A Thesis Submitted for the Degree of PhD at the University of Warwick

Frequency-Dependent Response of Neurons to Oscillating Electric Fields

by

Naveed Ahmed Malik

Thesis

Submitted to the University of Warwick

for the degree of

Doctor of Philosophy

MOAC Doctoral Training Centre and Warwick Systems Biology

August 2011

Acknowledgments

Writing this section seems almost as difficult as the thesis itself because the generosity of those who have contributed to this project far outweighs the quality of my writing. If I have forgotten someone, please accept my sincere apologies.

First and foremost, I thank God for giving me the faculties and the opportunity to embark on this project. Without His direct help I would for sure be lost at sea.

I am deeply and immeasurably indebted to my dearest "Huzur", Hadhrat Mirza Masroor Ahmad (atba). He is the reason I started my PhD and his wise guidance, kind encouragement, continued prayers and inspirational personality are what got me through this journey.

I cannot thank enough my primary supervisor, Magnus Richardson, the best supervisor a student can have. He has not only helped me greatly throughout this project, but has taught me the meaning of academic professionalism. I would also like to thank my co-supervisor Mark Wall, for supporting this project from start to finish.

I would like to thank Alison Rodger, who took me in to MOAC and has provided academic and moral support throughout. Also many thanks to the amazing MOAC staff: Dorothea Mangels, Philip Richardson and Sarah Shute for all the help. I am forever grateful to Monica Lucena who provided me with crucial first aid after I managed to cut my hand in the lab and nearly fainted due to loss of blood (we were measuring water of all things). Many thanks also to my advisors Matthew Turner, Sacha Ott and Bruno Frenguelli, for their excellent guidance throughout these years.

I am grateful to the EPSRC for the financial support.

My friends at Warwick were a blessing. I am especially grateful to Jon, Elina and Alistair, whose friendship I treasure (I can't help but smile when I think of our ill-advised road trip to the coast). A big thank you to my wonderful friends, "the room 330 gang": Sapna, Boris, Chengjin, Mudassar and Daniela, who brought the office to life with their laughter and kindness (I wish we had more time for our badminton matches and Frisbee playoffs). I would also like to thank Azadeh and Stephen, my "theoretical neuroscience buddies" for their company and support.

I am greatly indebted to my friends whose moral support and prayers kept me going. A special thank you to Fahim Anwer for his kindness and help all the way through. I am grateful to my dear friend Asim Mumtaz. From Cambridge to Warwick, he has guided and helped me in every way he could. I thank my dear friend Zia Rehman for all the support (I still have fond and "interesting" memories of our trip to China). And what can I say about the MKA Research Association crew: Muddassar, Anas, Azhaar, Adeel, Qasid, Rizwan, Usama, Taha N, Tahir, Umar, Taha M, Foaad, Shahzaib, Talha and Arslan? There is no other bunch of "gupshupping", ready for anything, stargazing and brilliant gentlemen on the planet. I thank you all from the bottom of my heart because your company inspired me to keep going. I am especially grateful to Tauseef Khan, who has been a true friend and a mentor to me all the way through. I am especially thankful to Jahangeer Khan Sahib, whose genuine kindness and unwavering brilliance never fail to inspire me.

I am eternally grateful to my friends in Coventry who were a family away from home. How can I forget Badr Aunty, Mumtaz Uncle and their family who took me in during the first days of my course (I still remember Aunty's delicious cooking fondly). A special thanks to Abdul Aziz Dogar Sahib, his inimitable spirit, kindness and prayers were my fuel.

I am fortunate beyond measure to have a loving, supporting and understanding family. I am grateful to my dear brothers Kashif and Atif, who have always looked after me in every way and never let me feel the loss of our father. They are an inspiration to me and the pillars of my life. I am forever grateful to my dearest mother whose prayers through the nights have carried me through this long journey. There is no other person who has suffered more during this project and yet has unconditionally supported me in every way. She is the truest person I know, and I can never thank her enough for it. I would also like to thank Nadeem Bhai, Lubna Baji and their family for their unwavering support and guidance. I cannot forget my dear Zia Khalo Jaan and Anjum Khala Jaan. I am grateful to them for always remembering me despite the long distances.

Lastly I would like to thank the most special person in my life, my wife and friend, Fiza. She has brought joy in to my life and taught me how to live. She brings out the best in me. Her laughter is the light of my life and she herself is my raison d'être. Du bist mein Wunder der Natur.

I dedicate this thesis to my father, Zarif Ahmed Malik, the most humble and gentle person I knew. I miss you Abbu.

Abstract

Neuronal interactions with electric fields depend on the biophysical properties of the neuronal membrane as well as the geometry of the cell relative to the field vector. Biophysically detailed modeling of these spatial effects is central to understanding neuron-to-neuron electrical (ephaptic) interactions as well as how externally applied electrical fields, such as radio-frequency radiation from wireless devices or therapeutic Deep Brain Stimulation (DBS), interact with neurons. Here we examine in detail the shape-dependent response properties of cells in oscillating electrical fields by solving Maxwell's equations for geometrically extended neurons.

Early modeling for compact (spherical) cells in alternating fields predicts a smaller effective membrane time constant for the field-cell system compared to direct current injection via whole-cell patch clamp. This result, predicting that cells should respond strongly to field oscillations in the kHz range, was verified later in vitro for murine myeloma cells. However, recent experiments on CA3 pyramidal cells (highly elongated neurons) in the hippocampus do not exhibit this high frequency response. In this thesis we examine the implications of modeling full two-way coupling between three-dimensional cylindrical neurons and the extracellular field utilizing three different methodologies, namely: cable equation, finite-difference and finite-element. Our modeling demonstrates that the electrotonic length and orientation of the cell to the field are key determinants of the neuronal response to oscillating fields. This explains the experimentally observed absence of the high frequency response for pyramidal neurons when the applied field direction is oriented along their dendritic axis. Additionally, we developed biophysically detailed models of neuronal membranes with quasi-active electrical properties stemming from voltage-gated currents. These are known to lead to resonances at characteristic frequencies in the case of current injection via whole-cell patch clamp. Interestingly, in the field-cell system, the resonance was masked in compact, spherical neurons but recovered in elongated neurons.

Utilizing our cable and finite-element models, we investigate the effect of point-source stimulation on cylindrical neurons and find a novel type of "passive resonance" not reported before in the literature. We further extend our modeling by incorporating Hodgkin Huxley channels in to the membrane and construct a fully active, spiking model of a neuron, fully coupled to the applied electric fields. We then go on to embed the neuron in to an array of cells to validate our results at the tissue-level.

These findings delineate the relationship between neuron shape, orientation and susceptibility to high frequency electric fields, with implications for DBS efficacy, ephaptic coupling in networks and the filtering properties of cortical tissue.

Contents

Acknowledgments **i**

Abstract **iv**

List of Tables **ix**

List of Figures **x**

Declarations **xxxiii**

Chapter 1 Introduction **1**

1.1 The neuron as a computational engine 1

1.2 The membrane and the membrane potential 5

1.3 Synapses: How neurons communicate 12

1.4 General equations - coupling the membrane to electric fields 13

1.5 Deriving the time-dependent solution from the steady-state solution 17

1.6 Analytical modeling of field effects on single neurons - a discrepancy between theory and experiment 20

1.7 The need for modeling electric field effects 23

Chapter 2 Modeling passive cylindrical neurons in uniform electric fields **28**

2.1 Introduction 28

2.2 Modeling finite cylindrical neurons in an extracellular field using the cable equation . . . 30

2.3 Finite cable with sealed ends in a uniform field . . . 34

  2.3.1 Example calculation with a non-oscillating field . . . 34

  2.3.2 Example calculation with an oscillating field . . . 37

2.4 Finite cable with conducting ends in a uniform field . . . 44

2.5 Modeling cylindrical neurons with finite radii in uniform electric fields - beyond the cable equation . . . 48

  2.5.1 Finite-difference method for a finite cylindrical neuron in a uniform electric field . . . 51

  2.5.2 Finite-element method for a finite cylindrical neuron in a uniform electric field . . . 55

  2.5.3 Results and comparisons . . . 58

2.6 Physical reasoning behind the shape-dependent frequency response . 67

Chapter 3 Extracellular point-source stimulation of neurons 69

3.1 Point-source stimulation of a sealed cable . . . 70

  3.1.1 Steady-state point-source stimulation of finite cylinders . . . 75

  3.1.2 Sinusoidally oscillating point-source stimulation of finite cylinders - membrane potential response at the stimulation end . . 78

  3.1.3 Sinusoidally oscillating point-source stimulation of finite cylinders - membrane potential response away from the stimulation end . . . 86

  3.1.4 Conducting-end cables . . . 92

3.2 Summary of results . . . 95

Chapter 4 Quasi-active and fully active membranes 99

4.1 Quasi-active membrane . . . 100

4.1.1 The time-dependent spherical and cylindrical neurons with quasi-active membranes 103
4.2 Fully active Hodgkin Huxley neurons 106
4.3 Field interactions with neurons embedded in tissue 110
4.3.1 The array-embedded neuron with a passive membrane 113
4.3.2 The array-embedded neuron with a quasi-active membrane . 114
4.3.3 Explanation for the array results 114

Chapter 5 Conclusions **119**

5.1 A methodology for modeling two-way feedback coupling between the neuron and the field 120
5.2 Relationship between high-frequency response and electrotonic length 121
5.3 Point stimulation of cylindrical neurons 123
5.4 Interaction between the subthreshold voltage-gated resonance and field 125
5.5 Constructing equivalent cylinders from real neuron geometries 126
5.6 Array-embedded neurons and frequency filtering in cortical tissue . . 127
5.7 Future work 129
5.8 Summary 131

List of Tables

1.1 Parameters for the passive membrane. We have artificially set the resting membrane potential E_L to be zero for ease of notation. We note that for passive models, setting the resting potential to zero only offsets the resulting membrane potential by E_L and does not influence the membrane dynamics. 23

3.1 Comparison between the cable and FEM models for point source stimulation of cylindrical neuron at one end ($x = 0$) 97

4.1 Parameters for the quasi-active membrane model 103

4.2 Parameters for the Hodgkin Huxley membrane model 109

5.1 Table of consistent units 132

5.2 Algebraic expressions and numerical values of the effective membrane time constants for field-cell systems with different neuronal geometries. The biophysical parameters are those given in table 1.1. 133

List of Figures

1.1 Neurons come in various shapes and sizes. a) A Golgi stained, human neocortical Pyramidal neuron. The apical dendrite extends vertically from the top of the soma with secondary dendritic branches. The basal dendrites emerge laterally from the base of the soma with respective secondary branching. The most numerous type of excitatory neuron in the mammalian cortex, the Pyramidal neuron is found in the cerebral cortex, hippocampus and amygdala, and is thought to play important roles in cognitive processes. (Image by Bob Jacobs, Laboratory of Quantitative Neuromorphology Department of Psychology, Colorado College). b) Drawing of two pigeon Purkinje neurons by Santiago Ramon y Cajal, 1899. Some of the largest neurons in the human brain, Purkinje Neurons are anatomically characterized by an exceptionally elaborate and almost two-dimensional dendritic arbor, and a large number of dendritic spines. Found in the cerebellar cortex, these cells are a class of inhibitory GABAergic neurons. c) A Golgi stained cortical layer IV spiny stellate neuron. Several dendrites radiate away from the cell body, giving the neuron a star-like shape and hence their name. Stellate neurons are found in the molecular layer of the cerebellum as well as in the cortical layer IV. (Image from Churchill et al. BMC Neuroscience 2004 5:43 doi:10.1186/1471-2202-5-43). . . 2

1.2 A stereotypical illustration of a neuron. The dendrites are cellular extensions, which receive the majority of the input in to the neuron through synaptic contacts. Although dendritres are typically considered as passive elements, they have recently been found to harbour active channels, which mediate nonlinear phenomena such as dendritic spikes. The cell body or soma contains the nucleus and the protein synthesis machinery. The input in to the cell is passively integrated through spatiotemporal summation over the soma and the resultant membrane potential at the axonal hillock dictates the occurrence of an action potential. The action potential or spike is a nonlinear "all or none" wave, which constitues the output of the cell and travels down the axon and on to axon collaterals, which synapse on to further neurons. The axon can be myelinated by glial cells (Schwann cells), which insulate it at regular intervals and prevent the active propagation of the action potential through the membrane. The axonal spike propagation in the myelinated parts of the axons thus takes place electrotonically through the intracellular medium, with the action potential effectively "jumping" between the uninsulated Nodes of Ranvier, ensuring a high conduction velocity. (Image from Quasar Jarosz at en.wikipedia, URL: http://en.wikipedia.org/wiki/File:Neuron_Hand-tuned.svg). 4

1.3 A schematic of the biological membrane. The membrane consists of a lipid bilayer with embedded proteins. Acting as a selective barrier, separating the intracellular cytoplasm from the extracellular space, the membrane is impermeable to most charged molecules. The protein ion channels are selectively permeable across the membrane and can be leak, voltage-gated or ligand-gated (Image from Mariana Ruiz Villarreal at en.wikipedia, URL: http://en.wikipedia.org/wiki/File:Scheme_facilitated_diffusion_in_cell_membrane-en.svg). 6

1.4 The electric circuit model of the neuronal membrane. The membrane can be modeled as an electric circuit, with a capacitor in parallel to a resistor. The particular form of the ionic current is dictated by the particular model of the membrane under consideration and could be linear or nonlinear in the membrane potential, depending on the absence or presence respectively, of voltage-gated active channels (see Eqs. 1.2 and 1.3). 7

1.5 A schematic of the neuronal action potential showing the different phases. Upon the membrane potential reaching threshold (marked with blue), the rising phase of the action potential is brought about by the active sodium channels while the active potassium channels are responsible for the downward stroke. The undershoot phase sees the membrane potential become more negative than the resting potential (after hyperpolarization) and is caused by the high potassium permeability and slowly closing potassium channels. (Image from Synaptitude at en.wikipedia, URL: http://en.wikipedia.org/wiki/File:Action_potential_vert.png). 10

1.6 A schematic of a chemical synapse. An action potential in the presynaptic axon terminal triggers the entry of calcium ions into the terminal, which in turn causes the exocytosis of the neurotransmitter in to the synaptic cleft. The neurotransmitter then triggers excitatory or inhibitory postsynaptic potentials. (Image from Nrets at en.wikipedia, URL: http://en.wikipedia.org/wiki/File:SynapseIllustration2.svg). . 13

1.7 A schematic of a gap junction. Allowing for direct passage of ions in between cells, gap junctions or electrical synapses are a faster mode of intercellular communication then the chemical synapse. Composed of two hemichannels (connexons), gap junctions are formed between cells, which are 2-4 nm apart. Unlike the chemical synapses, gap junctions do not facilitate signal gain between cells. (Image from Mariana Ruiz Villarreal at en.wikipedia, URL: http://commons.wikimedia.org/wiki/File:Gap_cell_junction_en.svg) 14

1.8 Polarization (induced membrane potential) of a passive cylindrical neuron (radius 2 μm and length 8 μm) in the presence of a uniform electric field of strength 1 V/m (steady-state field is in the positive z-axis direction i.e. bottom to top in the orientation of the above figures). The color scheme represents the membrane potential, $V_m = V_i - V_e$ (in mVs) which is a measure of the charge accumulation on the capacitive membrane (with c_m as the per unit area capacitance). The charge density in the bulk regions is zero (see above section 1.4). The results are derived using the finite-element scheme (section 2.5.2) a) Polarization due to the steady-state field. The neuron end proximate to the positive terminal is hyperpolarised (positive charge outside and negative inside) whereas the neuron end proximate to the negative terminal is depolarised (negative charge outside and positive inside), as expected. b) Polarization due to oscillating field (100 Hz) with oscillation phase of π. The field polarity is reversed with respect to a) and so is the polarization of the neuron. c) Polarization due to oscillating field (100 Hz) with oscillation phase of $\frac{\pi}{4}$. d) Polarization due to oscillating field (100 Hz) with oscillation phase of $\frac{3}{4}\pi$. 18

1.9 Current flow in a field-neuron system with a passive cylindrical neuron (radius 2 μm and length 8 μm) in the presence of a uniform electric field of strength 1 V/m (steady-state field is in the positive z-axis direction i.e. bottom to top in the orientation of the above figures). The arrows represent the direction and strength of the current density J in the bulk regions (in A/m^2). The contours are lines of constant potential with the color scheme representing the intracellular (left colourbar) and the extracellular (right colourbar) potential (in mVs). The results are derived using the finite-element scheme (section 2.5.2) a) Current flow due to the steady-state field. The current flows from the positive terminal to the negative one while diverting away from the high resistance membrane. b) Polarization due to oscillating field (100 Hz) with oscillation phase of π. The current direction is reversed with respect to a). c) Current flow due to oscillating field (100 Hz) with oscillation phase of $\frac{\pi}{4}$. d) Current flow due to oscillating field (100 Hz) with oscillation phase of $\frac{3}{4}\pi$. 19

1.10 Two alternative ways of cell stimulation. (a) (Left) Current injection via whole cell patch-clamp: The membrane behaves isopotentially and the cell response is dependent on the membrane conductance and capacitance, not on the extra and intracellular conductivities (Eq. 1.24). (Right) Membrane potential distribution on a spherical neuron of radius 10 μm in the presence of an electric field oriented along the x-axis. The membrane potential is dependent on the position on the cell as well as the extra and intracellular conductivities (Eq. 1.21). (b) Normalized membrane potential responses of a passive current-injected and a passive field-stimulated spherical neuron (of radius 10 μm) to sinusoidal stimulation at varying frequencies. The current-injected point-neuron response (Eq. 1.24) falls off at around 10 Hz stimulation frequency, whereas the field-stimulated response (Eq. 1.21) is sustained up to kHz frequencies. Parameter values are as in table 1.1. 24

2.1 Schematic of a pyramidal neuron in an electric field. In a typical experimental setup, an in vitro neuronal slice is placed between parallel field electrodes, which are used to apply an electric field. The applied field is uniform far away from the cell and is in general aligned with the axo-dendritic axis of the neuron. 29

2.2 The core conductor model for a dendrite. a) A small section of a neuronal dendrite is modeled as a cylindrical cable with a thin membrane separating the intra and extracellular media. The extracellular potential is typically assumed to be constant and grounded. b) The dendritic cable is modeled as segments of parallel resistor-capacitor circuits joined in series by resistances r_L along the fiber. The capacitance c_m arises from the electrostatic forces acting through the lipid bilayer, the membrane resistance $1/g_L$ from the leak channels and the longitudinal resistances along the fiber r_L from the cytosol. 31

2.3 Steady-state membrane potential profiles for sealed-end cable neurons of various electrotonic lengths (L_e =0.5, 1, 2 and 4), in a uniform electric field oriented along the cable length. V_m is plotted against the distance along the cable x (measured in units of λ), with x only ranging from 0 to the cable half-length l, due to symmetry. Electrotonically longer cables are more eccentrically polarized than the shorter ones and V_m takes on a linear profile near the center of the cable ($x = 0$) for all electrotonic lengths. The parameters used to produce this figure are as given in table 1.1, with the cable radius $a = 2$ μm and $\lambda = 447.2$ μm. 36

2.4 Electrotonically compact neurons remain responsive to high-frequency electric field stimulation. a) Frequency response of cable neurons of various electrotonic lengths (box top right) to electric field stimulation, with V_m measured at cable end ($x = l$). More compact neurons (L_e = 0.5, 1) exhibit a higher drop-off frequency indicating a shorter effective time constant (τ_{cab}) for membrane polarization. The frequency response of all the neurons converges at high frequencies, with the response of the shorter neurons never significantly exceeding that of the longer ones. b) Frequency response of cable neurons with V_m measured at $x = \frac{l}{2}$. Frequency selectivity is observed with differing high-frequency asymptotes and the high-frequency response of the compact neurons (L_e = 0.5, 1) exceeds that of the elongated ones (L_e = 4, 8). The parameters used to produce these figures are as given in table 1.1, with the cable radius $a = 2$ μm and $\lambda = 447.2$ μm. The neurons considered have sealed ends. 40

2.5 Steady-state V_m plotted against electrotonic length for various fractional positions (box top right) along the cable neuron exposed to a uniform field. The non-monotonic profiles indicate that due to the increasingly eccentric polarization profiles of the longer cable neurons, a shorter neuron will give a larger response for the same off-end fractional position, which in turn leads to the high-frequency selectivity for the shorter cable neurons (fig. 2.4). The parameters used to produce this figure are as given in table 1.1, with the cable radius $a = 2$ μm and $\lambda = 447.2$ μm. The neurons considered have sealed ends. . . 44

2.6 A difference in cable-end boundary conditions do not have a significant impact on the frequency response of the cable neurons. Frequency response for cable neurons of electrotonic lengths $L_e = 0.5$ and 2 for both sealed-end and conducting-end boundary conditions. The responses for the two boundary conditions are virtually superimposed at this resolution. The measurements are performed at $x = l$. The parameters used to produce this figure are as given in table 1.1, with the cable radius $a = 2$ μm and $\lambda = 447.2$ μm. 48

2.7 The high-frequency asymptotes differ for the sealed-end and the conducting-end cable neurons in uniform electric fields. a) Loglog plot for the frequency repose of the cable neuron of electrotonic length $L_e = 0.5$. b) Loglog plot for the frequency response of the cable neuron of electrotonic length $L_e = 2$. The difference between the boundary conditions occurs due to the neurons being effectively electrotonically long at higher field frequencies, causing a lack of global charge distribution during dynamic polarization. V_m is measured at the cable end ($x = l$) and the parameters used to produce these figures are as given in table 1.1, with the cable radius $a = 2$ μm and $\lambda = 447.2$ μm. 49

2.8 The finite-difference grid for a cylindrical neuron exposed to a uniform electric field, where a is the neuron radius, l is the neuron half-length, ρ is the radial coordinate, z is the axial coordinate, and V_i and V_e are the intra and extracellular potentials respectively. Due to the axial symmetry of the cylindrical system only a two-dimensional grid is required. Further symmetry conditions due to the uniform field require only a quadrant of the field-cell system to be simulated. Each point on the membrane boundary corresponds to two overlayed points, one intracellular and one extracellular, both coupled through the membrane conductance, g_L. 54

2.9 Steady-state membrane potential distribution on a field-stimulated cylindrical neuron with a non-conductive membrane (finite-difference results). The applied field orientation is along the cylinder axis (x-axis) a) Membrane potential distribution on the side of the cylinder, V_x, plotted according to the linear fit (Eq. 2.59). As expected, the neuron is hyperpolarized at the positive field end, while being depolarized at the negative end. The cylinder is of size 2×16 μm (b) Variation of V_x along the axial direction for different cell shapes and sizes (finite-difference). (c) Normalized variation in the axial direction: V_x/l versus x/l. The plots for the different shapes and sizes converge for longer cylinders on to the function $V_x = Ex$. (d) Membrane potential distribution, V_ρ on the top of the cylinder ($x = l = 16$ μm), plotted according to the semi-analytical fit (Eqs. 2.60 and 2.61). V_ρ is axis-symmetric and highest at the center of the cylinder base. (e) Radial distribution of V_ρ at $x = l$, plotted for cylinders of various shapes (numerical simulations). (f) Plots of $(V_\rho - El)/a$ Vs ρ/a elucidating the function $f\left(\frac{\rho}{a}\right)$. An $a \times l$ neuron corresponds to a cell with radius a and half-length l. 56

2.10 Results from the finite-element solution method (COMSOL Multiphysics). a) An example mesh for the two-dimensional axial symmetric problem. The elements are triangular and the mesh resolution increases inside the neuron and around the membrane to take account of the higher field strengths in those regions, in a computationally efficient manner. b) A two-dimensional potential plot for the cylindrical neuron in a uniform field. 59

2.11 Membrane potential versus g_L comparison between finite-difference, finite-element and cable methods for a) 2×4 μm and b) 2×16 μm (compact) cylindrical neurons. The finite-element and finite-difference results agree very closely but both differ significantly from the cable results with the difference greater for the more compact 2×4 μm neuron. The neurons considered have conducting ends. V_m is measured at the cable end ($x = l$) and the parameters used to produce these figures are as given in table 1.1, with the cable radius $a = 2$ μm and $\lambda = 447.2$ μm. 61

2.12 Frequency response comparison between finite-difference, finite-element and cable methods for a) 2×4 μm and b) 2×16 μm (compact) cylindrical neurons. As in the steady-state case with g_L-variation (fig. 2.11) the finite-difference and finite-element methods agree closely but differ from the cable results, with an increasing error for more compact neurons due to cell-to-field feedback. The neurons considered have conducting ends. V_m is measured at the cable end ($x = l$) and the parameters used to produce these figures are as given in table 1.1, with the cable radius $a = 2$ μm and $\lambda = 447.2$ μm. An $a \times l$ neuron corresponds to a cell with radius a and half-length l. 62

2.13 Comparison between finite-element and and cable methods in ascertaining the frequency response for cylindrical neurons of electrotonic lengths comparable to λ, in an oscillating electric field. a) The frequency responses of the $L_e = 0.5$ and 2 neurons show close agreement between the finite-element and the cable methods. The finite-element response slightly overtakes that of the cable method for both b) $L_e = 0.5$ and c) $L_e = 2$ neurons at high frequencies. The neurons considered have conducting ends. V_m is measured at the cable end $(x = l)$ and the parameters used to produce these figures are as given in table 1.1, with the cable radius $a = 2$ μm and $\lambda = 447.2$ μm. . . 63

2.14 Comparison between the finite-element and cable methods in ascertaining the frequency response for compact cylindrical neurons, in an oscillating electric field. a) The frequency of responses for the $l = 10$ and 20 μm neurons differ significantly between the finite-element and the cable methods in the low-frequency limit. The log-log plots also reveal that the finite-element response falls slightly below that of the cable method for both b) $10 \times 10\mu$m and c) $10 \times 20\mu$m neurons at high frequencies. The drop-off frequencies are identical for both models. The neurons considered have conducting ends. V_m is measured at the cable end $(x = l)$ and the parameters used to produce these figures are as given in table 1.1, with the cable radius $a = 10$ μm and $\lambda = 1000$ μm. An $a \times l$ neuron corresponds to a cell with radius a and half-length l. 64

2.15 A potential contour plot from the finite-element solution for a compact cylindrical neuron in a uniform electric field. The compact cell distorts the applied uniform electric field causing radial currents to flow. This is an example of the neuron feeding-back to the extracellular electric field. 66

3.1 Point-source stimulation of cylindrical neurons (cable neuron (right), and three-dimensional finite-element neuron (left)). Due to the asymmetry imposed by the point-source current, a full three-dimensional model of the neuron has to be considered for the finite-element method. We consider three measurement points on the three-dimensional cylinder, “proximate”, “middle” and “far”. 71

3.2 Steady-state membrane potential profiles of cable neurons of various electrotonic lengths, under point-source stimulation, with the source aligned horizontally with one of the cable-ends (fig. 3.1). V_m is plotted against x normalized to the cable length L. Two different values of the source-to-neuron distance are considered, with $I = 100$ nA. a) Illustration showing the positioning of the cable neuron with respect to the point source and the point of measurement. b) Plots for $d = 0.1\lambda$ and c) $d = \lambda$. A biphasic and asymmetric polarization is observed, with the neutral point located nearer to the stimulation end of the cable. The membrane potential profile becomes more symmetric with smaller $\frac{L}{d}$ ratios. The neurons considered have sealed ends. The parameters used to produce these figures are as given in table 1.1, with the cable radius $a = 2$ μm and $\lambda = 447.2$ μm. 77

3.3 Comparison between the FEM and cable methods for the steady-state membrane potential profiles of neurons under point-source stimulation ($I = 100$ nA) with a) $L_e = 0.5$ and $d = 0.1\lambda$ b) $L_e = 2$ and $d = 0.1\lambda$ c) $L_e = 0.5$ and $d = \lambda$ and $L_e = 2$ and $d = \lambda$. The source is aligned horizontally with one of the cable-ends (fig. 3.1). V_m is plotted against x normalized to the cable length L. The cable profiles match well with the "middle" FEM profiles. The difference between the cable and the "proximate" / "far" profiles arises due to the radial orientation of the field at and near $x = 0$. The neurons considered have sealed ends. The parameters used to produce these figures are as given in table 1.1, with the cable radius $a = 2$ μm and $\lambda = 447.2$ μm. 79

3.4 Comparison between the FEM and cable methods for the steady-state membrane potential profiles of a compact 10×10 μm neuron under point-source stimulation ($I = 100$ nA). The source is aligned horizontally with one of the cable-ends (fig. 3.1). a) The axial profile of V_m differs greatly between the "proximate" and "far" FEM results, and the cable results ($\sim$95% increase in V_m for the FEM model). V_m is plotted against x normalized to the cable length L. The neuron considered has sealed ends. b) Radial variation of V_m across the top of the FEM three-dimensional cylindrical neuron (taking a line from the "proximate" to the "far" point), with conducting and sealed ends. The radial field due to the point-source induces a radially varying membrane potential across the top of the cylinder. The parameters used to produce these figures are as given in table 1.1, with the cable radius $a = 10$ μm and $\lambda = 1000$ μm. An $a \times l$ neuron corresponds to a cell with radius a and half-length l. 80

3.5 Electrotonically compact cable neurons remain responsive to high-frequency electric field stimulation from a point-source ($I = 100$ nA and V_m is measured at the cable end proximate to the point-source $x = 0$). Frequency response of neurons of various electrotonic lengths (box top right) to point-source electric field stimulation, with V_m measured at the cable end closest to the source. Like in the uniform field case (fig. 2.4), more compact neurons exhibit a higher drop-off frequency indicating a shorter time constant for membrane polarization. The frequency response of all the neurons converge at high frequencies, with the response of the shorter neurons never significantly exceeding that of the longer ones. Two different values of d: a) 0.1λ and b) λ are used. The neurons considered have sealed ends. The parameters used to produce these figures are as given in table 1.1, with the cable radius $a = 2$ μm and $\lambda = 447.2$ μm. 82

3.6 Comparison between cable neurons under uniform and point-source field stimulation with $d = 0.1\lambda$ ($I = 100$ nA and V_m is measured at the cable end, $x = 0$). Neurons with two differing sizes: a) $L_e = 1$ (with $a = 2$ μm and $\lambda = 447.2$ μm) and b) 10×10 μm (with $a = 10$ μm and $\lambda = 1000$ μm) are considered. Both point and uniform stimulation produce the same frequency drop-offs. The neurons considered have sealed ends. The parameters used to produce these figures are as given in table 1.1. An $a \times l$ neuron corresponds to a cell with radius a and half-length l. 83

3.7 Comparison between finite-element and cable methods in ascertaining the frequency response for cylindrical neurons of electrotonic length $L_e = 1$, in an oscillating point-source electric field ($I = 100$ nA and V_m is measured at the cable end $x = 0$). The "middle" point for the FEM model matches well with the cable model for both a) $d = 0.1\lambda$ and b) $d = \lambda$. An additional high-frequency plateau is observed for the FEM models. The measurement is performed at the cable end proximate to the source. The neurons considered have sealed ends. The parameters used to produce these figures are as given in table 1.1, with the cable radius $a = 2$ μm and $\lambda = 447.2$ μm. 84

3.8 Comparison between finite-element and and cable methods in ascertaining the frequency response for a compact cylindrical neuron of size 10×10 μm , in an oscillating point-source electric field ($I = 100$ nA and the measurement is performed at the cable end proximate to the source $x = 0$). The FEM results for the "proximate" and "far" points differ greatly from the cable model for both a) $d = 0.1\lambda$ and b) $d = \lambda$. The difference is caused by the radial profile of the extracellular field for small $\frac{L}{d}$ ratios. The neurons considered have sealed ends. The parameters used to produce these figures are as given in table 1.1, with the cable radius $a = 10$ μm and $\lambda = 1000$ μm. An $a \times l$ neuron corresponds to a cell with radius a and half-length l. 85

3.9 The "passive resonance" is observed for off-end measurement of cable neurons under point stimulation (with V_m measured at $x = \frac{L}{4}$). Frequency response of cable neurons of various electrotonic lengths (box top right) with a) $d = 0.1\lambda$ and b) $d = \lambda$. Frequency selectivity is observed with differing high-frequency asymptotes and the high-frequency response of the compact neurons exceeds that of the elongated ones. Additionally strong and broad resonances are observed for L_e =1, 2 and 4 in the $d = 0.1\lambda$ case. The neurons considered have sealed ends and the parameters used to produce these figures are as given in table 1.1, with the cable radius $a = 2$ μm and $\lambda = 447.2$ μm. 87

3.10 Frequency response of cable neurons (of various electrotonic lengths (box top right)) under point stimulation, with V_m measured at the center $x = \frac{L}{2}$, with a) $d = 0.1\lambda$ and b) $d = \lambda$. Frequency selectivity is observed with differing high-frequency asymptotes and the high-frequency response of the compact neurons exceeds that of the elongated ones. No resonance is observed. The neurons considered have sealed ends and the parameters used to produce these figures are as given in table 1.1, with the cable radius $a = 2$ μm and $\lambda = 447.2$ μm. 88

3.11 Frequency response of cable neurons of various electrotonic lengths (box top right) under point stimulation, with V_m measured at $x = \frac{3L}{4}$, with a) $d = 0.1\lambda$ and b) $d = \lambda$. Frequency selectivity is observed with differing high-frequency asymptotes and the high-frequency response of the compact neurons exceeds that of the elongated ones. No resonance is observed. The neurons considered have sealed ends and the parameters used to produce these figures are as given in table 1.1, with the cable radius $a = 2$ μm and $\lambda = 447.2$ μm. 89

3.12 Frequency response of cable neurons of various electrotonic lengths (box top right) under point stimulation, with V_m measured at $x = L$, with a) $d = 0.1\lambda$ and b) $d = \lambda$. Frequency selectivity is observed with differing high-frequency asymptotes and the high-frequency response of the compact neurons exceeds that of the elongated ones. No resonance is observed. The neurons considered have sealed ends and the parameters used to produce these figures are as given in table 1.1, with the cable radius $a = 2$ μm and $\lambda = 447.2$ μm. 90

3.13 Development of the localized resonance through the length of the cable neuron from $x = 0.1L$ to $x = 0.5L$. The neuron under consideration is of size $L_e = 1$ and has sealed ends. The parameters used to produce these figures are as given in table 1.1, with the cable radius $a = 2$ μm and $\lambda = 447.2$ μm. 92

3.14 "Passive resonance" is observed for the three-dimensional FEM models as well as for the cable models (measurement performed at $x = 0.25L$ with horizontal electrode-neuron distance $d = 0.1\lambda$). The neuron under consideration is of size $L_e = 1$. The high-frequency plateau for the FEM case is observed as in the cases where the measurements are performed at $x = l$ above (fig. 3.7). The neuron has sealed ends and the parameters used to produce these figures are as given in table 1.1, with the cable radius $a = 2$ μm and $\lambda = 447.2$ μm. 93

3.15 The “passive resonance” is observed for off-end point stimulation of cable neurons. Frequency response of cable neurons of various electrotonic lengths (box top right). The horizontal electrode-cell distance is $d = 0.1\lambda$ a) Point-source is placed next to the vertical center of the neuron and the measurement is performed at $x = 0$. No resonance is observed. b) Point-source is placed next to the vertical center of the neuron and the measurement is performed at $x = 0.25L$. No resonance is observed. c) Point-source is placed a quarter of the way up the length of the neuron ($x = \frac{L}{4}$) and the measurement is performed at $x = 0$. Strong and broad resonances are observed. The neurons considered have sealed ends and the parameters used to produce these figures are as given in table 1.1, with the cable radius $a = 2$ μm and $\lambda = 447.2$ μm. 94

3.16 The “passive resonance” is observed for point stimulation of cable neurons with conductive ends (horizontal electrode-cell distance is $d = 0.1\lambda$). Frequency response of cable neurons of various electrotonic lengths (box top right). a) Point-source is placed at $x = 0$ and the measurement is performed at $x = \frac{L}{4}$. b) Point-source is placed at $x = \frac{L}{4}$ and the measurement is performed at $x = 0$. The “passive resonances” are apparent as in the sealed-end cases above. The parameters used to produce these figures are as given in table 1.1, with the cable radius $a = 2$ μm and $\lambda = 447.2$ μm. 96

3.17 The different features of the frequency profile for the point-stimulated FEM cylindrical neuron. The FEM and cable plots are as in fig. 3.7a for cylindrical neurons of electrotonic length $L_e = 1$, in an oscillating point-source electric field ($I = 100$ nA, $d = 0.1\lambda$ and V_m is measured at the cable end, $x = l$). In agreement with the cable plot, all three FEM profiles exhibit the low frequency plateau and the same frequency drop-off. In contrast with the cable plot, the "proximate" and "far" point profiles also exhibit a high frequency plateau. This high frequency plateau is also seen in measurements with the "passive resonance" (fig. 3.14). 98

4.1 Electric circuit models of active membranes. a) Representation of non-linearized two-component system with one type of voltage-gated channel. b) The LRC Circuit representing the the linearised form of the two-component system in a). The inductance, $L = \frac{\tau_n}{\kappa}$ and the conductances are given by $\kappa = g_n(V_m^* - E_n)\frac{dn_\infty}{dV_m}|_{V_m^*}$ and $g_T = g_L + g_n n^*$. c) Circuit representing the fully active Hodgkin Huxley membrane, with the respective sodium, potassium and leak conductances. . . . 101

4.2 Frequency response for field-stimulated neurons of various shapes (Spherical, finite-element and cable results) with quasi-active membranes in a uniform oscillating field. a) Comparison between the current-injected neuron and the field-stimulated spherical neuron of radius 10 μm (analytical solutions in Eqs. 4.11 and 4.12 respectively). The subthreshold resonance is clearly evident in the current-injected case whereas it is eliminated in the field-stimulated spherical neuron case. b-d) Comparison between field-stimulated cylindrical neurons of electrotonic lengths $L_e = 0.5$, 1 and 2, respectively, with the measurement performed at the cable end ($x = l$). The resonance disappears for neurons with low electrotonic lengths but is recovered for elongated neurons. Both the FEM and cable results agree well for the given neuron sizes. The cable neurons under consideration have sealed ends. The parameters used to produce these figures are as given in table 4.1, with the cable radius $a = 2$ μm and $\lambda = 447.2$ μm. 105

4.3 The "passive resonance" in the Hodgkin Huxley Neuron. a) The resonance profile for a passive cable neuron of size $L_e = 1$, under point stimulation ($I = 100$ nA) at $x = 0$ and measured at $x = 0.25L$. The horizontal electrode-cell distance is $d = 0.1\lambda$. The parameters are as given in table 1.1b) The dynamic subthreshold oscillations in a finite-element Hodgkin Huxley neuron of size $L_e = 1$ and $I = 100$ nA. The parameters are as given in table 4.2. The stimulation and measurement points are as in a). The resonance can be seen in the amplitudes, going from 100-5000 Hz. The neurons considered have sealed ends with the cable radius $a = 2$ μm and $\lambda = 447.2$ μm. . . . 111

4.4 A point-stimulated, finite-element spiking neuron of size $L_e = 1$ and $I = 100$ nA (the stimulation and measurement points are as in fig. 4.3). The rising amplitude due to the resonance can be seen going from a) 5 Hz to b) 10 Hz to c) 100 Hz with the 100 Hz neuron firing. $I = 2000$ nA for all the models. The parameters are as given in table 4.2. The neurons considered have sealed ends with the cable radius $a = 2$ μm and $\lambda = 447.2$ μm. 112

4.5 The semi-infinite neuronal array a) A schematic of the 3-dimensional field-stimulated neuronal array, simulated using the finite-element method. The periodic boundary conditions along the field-perpendicular axes simulate an effectively infinite number of neurons along these directions. The cumulative height of cells is maintained at approximately 100 μm above and below the central observed cell. b) Normalized steady-state membrane potential distribution, V_x/x for a $4 \times 4 \times 4$ and $4 \times 4 \times 32$ μm passive array-embedded neuron exposed to a non-oscillating electric field oriented along the x-axis. The field-coupling for the array-embedded neuron is much greater than for the isolated case, with the magnitude of the induced membrane potential approximately twice that for an isolated neuron. The parameters used to produce b) are as given in table 1.1. An $w \times d \times l$ neuron corresponds to a cell with width w, depth d and half-length l. 115

4.6 Frequency response for a passive array-embedded neuron exposed to an oscillating electric field (the measurement is performed at the "top-right" corner of the central neuron). The array-embedded cell is compared with the monolayer-embedded and the isolated cases for cell sizes of a) $4 \times 4 \times 4$ μm and b) $4 \times 4 \times 32$ μm. The drop-off frequency decreases going from the isolated to the full array-embedded neuron, with the cells in the field-perpendicular plane primarily contributing to the change as demonstrated by the monolayer case. The effect of cell elongation on the drop-off frequency is still apparent with the array-embedded neuron. The parameters used to produce these figures are as given in table 1.1. An $w \times d \times l$ neuron corresponds to a cell with width w, depth d and half-length l. 116

4.7 Frequency response for a quasi-active field-stimulated neuron embedded in array and exposed to an oscillating electric field (the measurement is performed at the "top-right" corner of the central neuron). The array-embedded cell is compared with the monolayer-embedded and the isolated cases for cell sizes of a) $4{\times}4{\times}256$ μm and b) $4{\times}4{\times}512$ μm. Analogous to the isolated neuron case, the resonance reappears for the longer neuron. Additionally the resonance amplitude increases going from the isolated case to the monolayer-embedded or the field-embedded cases. The parameters used to produce these figures are as given in table 4.1. An $w \times d \times l$ neuron corresponds to a cell with width w, depth d and half-length l. 117

Declarations

I declare that, to the best of my knowledge, the material contained in this thesis is original and my own work except otherwise indicated, cited, or commonly known.

Chapter 1

Introduction

1.1 The neuron as a computational engine

The neuron is the fundamental biological component of the nervous system, the functionality of which provides for the information processing capability of the complex neuronal networks in the brain. Thus understanding the full functional capabilities of the single neuron is crucial towards gaining insight in to the long sought after questions about how cognition and sentience are mediated by the interconnected networks of some 86 billion neurons in the human brain.

Neurons are widely differentiated in terms of their size and shape, with cell bodies ranging from 5-120 μm and shapes ranging from the pyramidal to the stellate (fig. 1.1). The general structure and functionality of the neuron however can be schematized as in (fig. 1.2). The input signals from the presynaptic neurons are received through the synaptic contacts on the dendrites and the cell body. These graded signals are then processed by the soma through threshold computation, resulting in an all or none action potential output at the axonal initial segment which travels down the length of the axon. The axon itself then branches off in to collaterals ending in synaptic terminals which generate chemically mediated output to other neurons through the synaptic cleft.

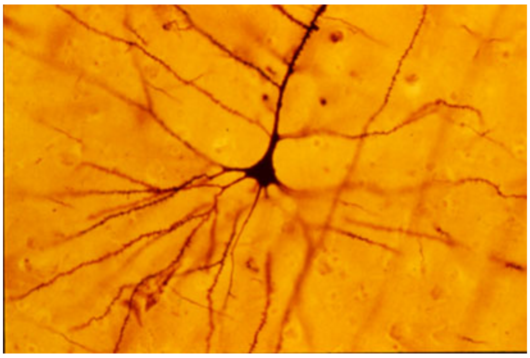

(a) Pyramidal neuron

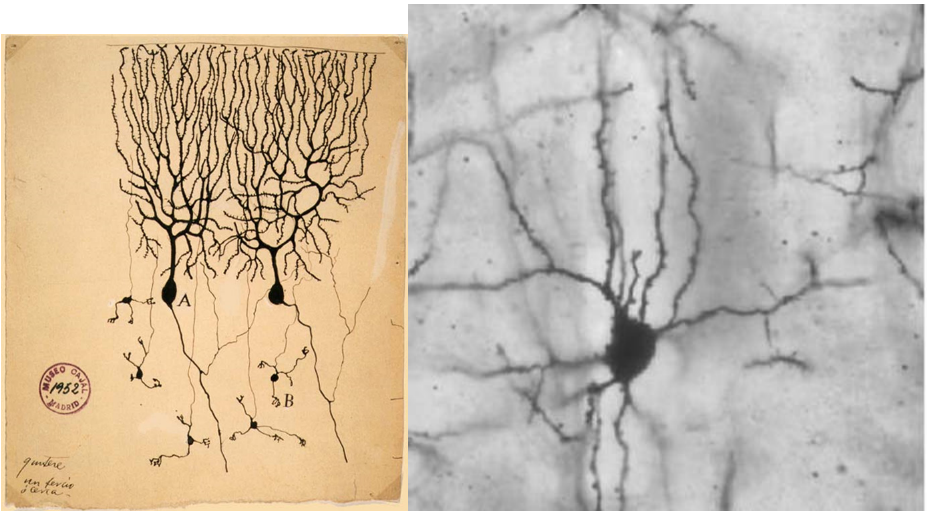

(b) Purkinje neuron

(c) Stellate neuron

Figure 1.1: Neurons come in various shapes and sizes. a) A Golgi stained, human neocortical Pyramidal neuron. The apical dendrite extends vertically from the top of the soma with secondary dendritic branches. The basal dendrites emerge laterally from the base of the soma with respective secondary branching. The most numerous type of excitatory neuron in the mammalian cortex, the Pyramidal neuron is found in the cerebral cortex, hippocampus and amygdala, and is thought to play important roles in cognitive processes. (Image by Bob Jacobs, Laboratory of Quantitative Neuromorphology Department of Psychology, Colorado College). b) Drawing of two pigeon Purkinje neurons by Santiago Ramon y Cajal, 1899. Some of the largest neurons in the human brain, Purkinje Neurons are anatomically characterized by an exceptionally elaborate and almost two-dimensional dendritic arbor, and a large number of dendritic spines. Found in the cerebellar cortex, these cells are a class of inhibitory GABAergic neurons. c) A Golgi stained cortical layer IV spiny stellate neuron. Several dendrites radiate away from the cell body, giving the neuron a star-like shape and hence their name. Stellate neurons are found in the molecular layer of the cerebellum as well as in the cortical layer IV. (Image from Churchill et al. BMC Neuroscience 2004 5:43 doi:10.1186/1471-2202-5-43).

The nerve cell can thus be thought of as the “multiplex neuron” as proposed by Waxman [1], where information processing occurs at distinct hierarchical levels of the cell; firstly in the dendrites through the spatiotemporal summation of excitatory and inhibitory synaptic inputs, secondly at the soma and the axon initial segment which can receive further synaptic inputs [2–5] and thirdly in the axonal tree and the end terminals with further synaptic inputs [6]. Thus the neuron is envisaged as analogous to a microelectronic “chip” rather than a “gate” [1, 7], a description far removed from the “point-neuron” view of the nerve cell as employed by McCulloch and Pitts in their 1943 paper on neural computation [8], consisting of a threshold computing soma receiving linear preprocessed synaptic inputs. This description highlights the substantial information processing power available to the nervous system even at a single cell level. With the discovery of active channels in the dendrites, facilitating forward and back propagating action potentials [9–12], and axon transmission delays and branch point failures facilitated by axonal morphology and channel biophysics [13], the role of the dendrites and axons has been extended beyond the simple transmission of input and output signals. In short, investigators are finding the “neural chip” to be more and more complex [13–16].

This thesis explores another source of computation available to the neuron, namely ephaptic coupling. Lesser known than its chemical and electrical synaptic counterparts, ephaptic coupling (from the Greek ephapse, meaning “to touch”) refers to influence through the extracellular medium, which can occur when proximate neurons alter their neighbours’ excitability through extracellular field generation. Until recently, ephaptic effects have been thought of as epiphenomena with a functional relevance restricted to pathological or artificial stimulation. But as we highlight below, new studies are demonstrating ephaptic field effects to have functional significance in normal nervous system operation. Firstly, in this chapter we introduce the key aspects of neuronal anatomy and describe the basic functionality of the neuron. We then go on to setup the mathematical framework for modeling neuronal function

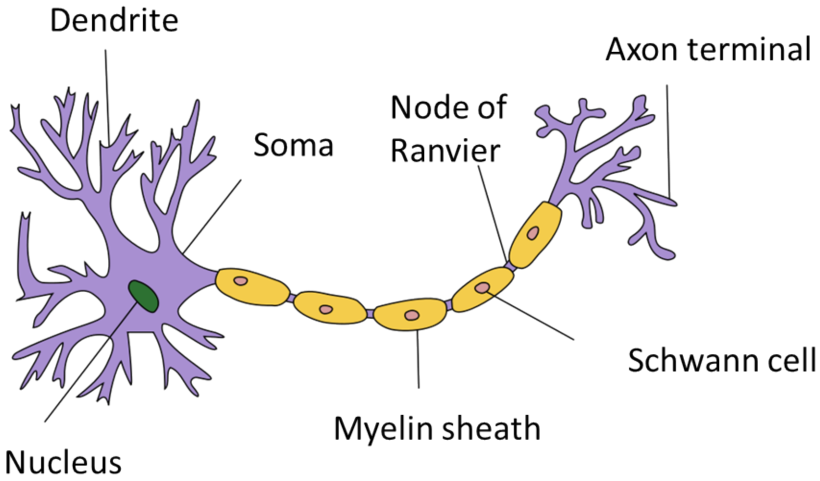

Figure 1.2: A stereotypical illustration of a neuron. The dendrites are cellular extensions, which receive the majority of the input in to the neuron through synaptic contacts. Although dendritres are typically considered as passive elements, they have recently been found to harbour active channels, which mediate nonlinear phenomena such as dendritic spikes. The cell body or soma contains the nucleus and the protein synthesis machinery. The input in to the cell is passively integrated through spatiotemporal summation over the soma and the resultant membrane potential at the axonal hillock dictates the occurrence of an action potential. The action potential or spike is a nonlinear "all or none" wave, which constitues the output of the cell and travels down the axon and on to axon collaterals, which synapse on to further neurons. The axon can be myelinated by glial cells (Schwann cells), which insulate it at regular intervals and prevent the active propagation of the action potential through the membrane. The axonal spike propagation in the myelinated parts of the axons thus takes place electrotonically through the intracellular medium, with the action potential effectively "jumping" between the uninsulated Nodes of Ranvier, ensuring a high conduction velocity. (Image from Quasar Jarosz at en.wikipedia, URL: http://en.wikipedia.org/wiki/File:Neuron_Hand-tuned.svg).

in the presence of extracellular electric fields. Finally, we highlight a discrepancy in the experimental literature considering field-cell interactions, before going on to justify the need for modeling extracellular electric field interactions within the nervous system.

1.2 The membrane and the membrane potential

The biological membrane is a lipid bilayer embedded with functional protein complexes (fig. 1.3), in general impermeable to most charged molecules and thus acts like a capacitor in separating charge on either side. The membrane allows current flow through embedded ion channels which provide for selective ion permeabilities. The essential variable which defines single neuron function is the membrane potential, a difference in potential which exists across the plasma membrane of all cells. For neurons at rest, this potential difference arises because of the difference in ionic concentrations (maintained by active ionic pumps) between the inside and outside of the cells with the membrane having different permeabilities for different ions. The membrane thus can be modeled by a simple electric circuit with a capacitor acting in parallel to a resistor (fig. 1.4). This model implies a transmembrane current density

$$J = c_m \frac{\partial}{\partial t} V_m + I_{ion}(V_m) \tag{1.1}$$

where c_m is the membrane capacitance per unit area, V_m is the membrane potential (inside minus outside) and t is the time. The first term on the right hand side of Eq. 1.1 is the capacitive current density while I_{ion} is the ionic current density through the channels. For subthreshold conditions when only the passive leak channels are open, I_{ion} is commonly modeled as a linear function of the membrane potential [17]

$$I_{ion} = g_L(V_m - E_L) \tag{1.2}$$

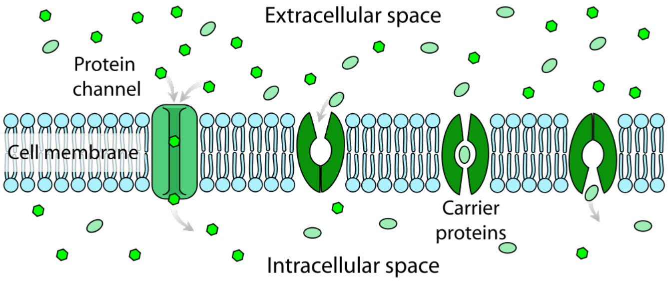

Figure 1.3: A schematic of the biological membrane. The membrane consists of a lipid bilayer with embedded proteins. Acting as a selective barrier, separating the intracellular cytoplasm from the extracellular space, the membrane is impermeable to most charged molecules. The protein ion channels are selectively permeable across the membrane and can be leak, voltage-gated or ligand-gated (Image from Mariana Ruiz Villarreal at en.wikipedia, URL: http://en.wikipedia.org/wiki/File:Scheme_facilitated_diffusion_in_cell_membrane-en.svg).

where $g_L = \sum g_i$ is the leak conductance per unit area and $E_L = \frac{\sum g_i E_i}{g_L}$ is the resting membrane potential, with g_i and E_i as the membrane conductance per unit area and the Nernst potential for the i_{th} ion, respectively.

Until now the description given for the transmembrane currents has been strictly passive, we know that when the membrane potential is sufficiently depolarized so that it reaches a threshold potential at the axon initial segment, the highly nonlinear process of the action potential occurs (fig. 1.5). The neuron is naturally excited to this state through the cumulative effect of synaptic or receptor inputs to its dendrites or the soma. The action potential or neuronal "spike" is a highly stereotyped nonlinear wave in the membrane potential which constitutes the output of the nerve cell. This rapid depolarization of the membrane, lasting for about a millisecond, is brought about through the action of voltage-gated ion channels, which are activated as the neuron reaches threshold. Sensing the initial depolarization, the fast acting sodium channels cause the rising phase in the action potential through a positive feedback mechanism, while the delayed outward rectifier potassium channels bring about the downward stroke. Including the transmembrane currents through

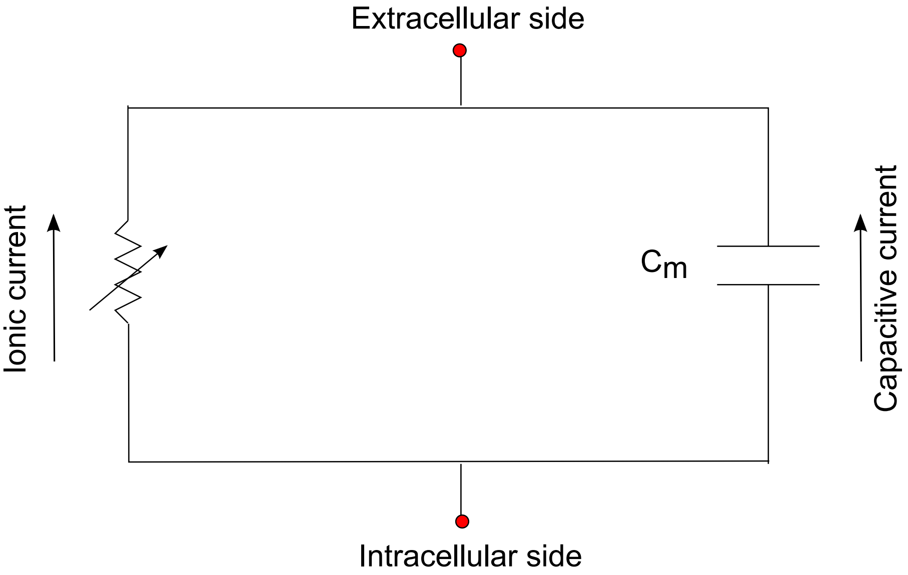

Figure 1.4: The electric circuit model of the neuronal membrane. The membrane can be modeled as an electric circuit, with a capacitor in parallel to a resistor. The particular form of the ionic current is dictated by the particular model of the membrane under consideration and could be linear or nonlinear in the membrane potential, depending on the absence or presence respectively, of voltage-gated active channels (see Eqs. 1.2 and 1.3).

these channels into the transmembrane current density J, we obtain

$$J = c_m \frac{\partial}{\partial t} V_m + g_L(V_m - E_L) + g_K n^4 (V_m - E_K) + g_{Na} m^3 h (V_m - E_{Na}) \quad (1.3)$$

where g_K and g_{Na} are the maximal conductances per unit area for the potassium and sodium ions respectively (they are the conductances per unit area if all the channels of the respective type are open), E_K and E_{Na} are the potassium and sodium reversal potentials respectively, and n, m and h are the gating variables described by their respective rate equations.

Equation 1.3 represents the membrane currents as described by the Hodgkin Huxley model [18] and is an example of a conductance-based description of the membrane potential dynamics, where the current density through a particular ion channel is given by the product of the conductance per unit area and the driving force $V_m - E_i$ at the ion channel, where $i \epsilon \{L, K, Na\}$. The first two terms on the right hand side of equation 1.3 represent the capacitive and the leak currents, respectively as stated earlier. The last two terms in equation 1.3 describe the currents through the potassium and the sodium channels respectively, with voltage-gated conductances which are given by the product of the maximal conductances and the probabilities that the respective channel is open (given by the products of the gating variables). The voltage dependence arises because n, m and h are dependent on V_m and hence t. For the persistent (noninactivating) potassium current density, the conductance is given by $g_K n^4$, where n^4 is the probability that the channel will be in an open state. The exponent of four for the gating variable n is essentially a functional value, being also consistent with the four subunits comprising the potassium channel, acting independently (with the probability of a single subunit opening to be n). The potassium conductance being noninactivating, only requires an activation gating variable (n), which increases with increasing depolarization.

For the transient sodium current density, the conductance is given by $g_{Na} m^3 h$, where now the probability of channel opening is given by the product of two gating variables $m^3 h$, to account for the transient nature of the conductance. Here m and h represent the activation and the inactivation gates of the sodium channel respectively. With increasing depolarization, m increases and activates the channel whereas h decreases and eventually inactivates the channel. It should be noted that the channel opening probabilities (n^4 and $m^3 h$) represent the fractions of channels (for potassium and sodium ions respectively) which are open at a particular time and arise from a deterministic description of the channel dynamics (justified by the large numbers of stochastically fluctuating individual channels). The dynamics of the gating variables are described by equations of the form

$$\frac{dj}{dt} = \alpha_j(V_m)(1-j) - \beta_j(V_m)j \tag{1.4}$$

where $j \epsilon \{n,\ m,\ h\}$, and α_j and β_j are the gate opening and closing rates, respectively. For the particular channel subunit, the first term on the right hand side of Eq. 1.4

is the product of the closed probability and the opening rate and thus represents the probability that the subunit opens in a short time interval. Similarly, the first term on the right hand side of Eq. 1.4 is the product of the open probability and the closing rate and thus represents the probability that the subunit closes in a short time interval. Thus the difference of the two terms gives the rate of change of the open probability j. The rate functions are obtained by fitting experimental data, but the general form can be derived using thermodynamic arguments (see chapter 5 of [84]). The particular expressions for the rate functions used in this thesis, are given in section 4.2, where we model active neurons in the presence of extracellular electric fields.

The action potential is propagated along the axonal fiber due to the excitation of downstream sodium channels through extracellular and intracellular local circuit currents which flow passively between the active zone and the oncoming dormant part of the axonal fiber.

Traditional point-neuron models assume the transmembrane current and hence V_m to be spatially independent, leaving a one-dimensional system of differential equations to be solved. The development of linear cable theory in the late 1950s by Rall [19] allowed modelers to treat dendrites as one-dimensional core conductor cables surrounded by a passive membrane. In the majority of these modeling approaches, assumptions are made which a priori exclude the possibility of realistic extracellular interaction. In the first instance, the extracellular potential is assumed to be grounded at zero, implying that no injection of current occurs in the extracellular space, either from other neurons or an artificial source. Secondly, when an extracellular potential is imposed, it is decoupled from the activity of the neuron itself.

In reality the neuronal membranes are not isolated from influence of extracellular fields and neither is the extracellular environment isolated from the influence of the neuron. Local excitability changes and impulse synchronization in isolated par-

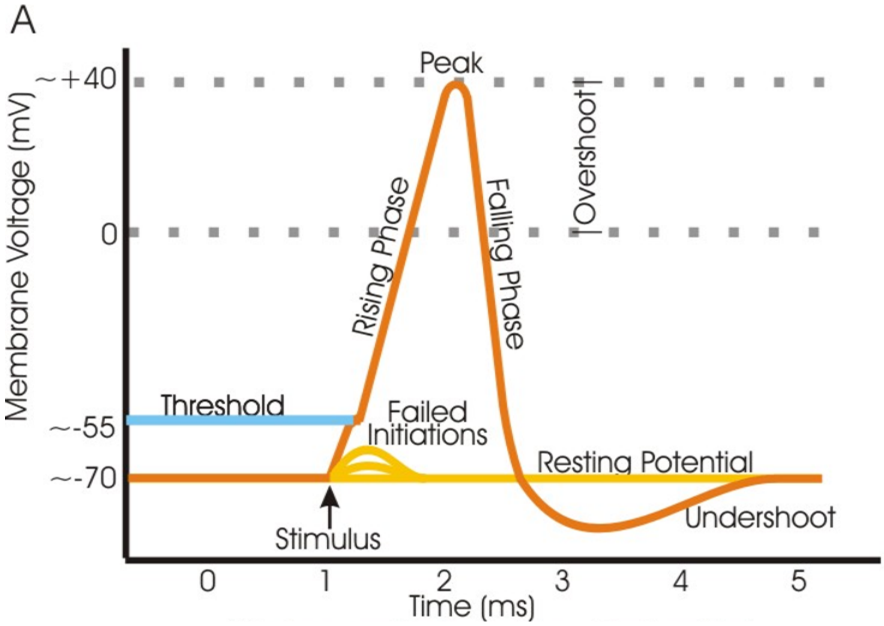

Figure 1.5: A schematic of the neuronal action potential showing the different phases. Upon the membrane potential reaching threshold (marked with blue), the rising phase of the action potential is brought about by the active sodium channels while the active potassium channels are responsible for the downward stroke. The undershoot phase sees the membrane potential become more negative than the resting potential (after hyperpolarization) and is caused by the high potassium permeability and slowly closing potassium channels. (Image from Synaptitude at en.wikipedia, URL: http://en.wikipedia.org/wiki/File:Action_ potential_vert.png).

allel nerve fibers via extracellular ephaptic coupling were demonstrated as far back as 1940 [20, 21]; Katz and Schmitt being the first to do so using the crab limb nerve model [20]. Axo-axonal interactions have been proposed to occur in situations where the myelin sheath is compromised or the nerves are brought into unphysiological proximity, such as in multiple sclerosis or in crushed nerves [22]. In such a situation an action potential in one axon can change the excitability of or even cause an action potential in the neighboring axons through local extracellular currents. This type of ephaptic interaction is also hypothesized to occur in physiological conditions where the axons are tightly packed, increasing the extracellular resistance, such as in the mammalian olfactory nerve fascicles containing unmyelinated axons [23,24]. Another type of ephaptic communication is via the modulation of the spike threshold, where the extracellular potential around an axon hillock is modified through the action of other neurons. This type of communication, providing for fast local inhibition of the spike initiation zone has been shown to occur within specialized structures around the teleost Mauthner and the mammalian cerebellar Purkinje cells [25,26]; to date the only known cases of ephaptic coupling in non-pathological systems without artificial electrical stimulation.

Furthermore, the existence of synchronous oscillations within hippocampal slices, in the absence of synaptic function between pyramidal cells [27–31], has demonstrated the significant contribution of the extracellular field towards neuronal synchronization, in vitro. These as well as other endogenous effects constitute potentially significant roles for extracellular field coupling, in neuronal synchrony and computation, during both pathological and non-pathological nervous function [13, 32]. The evidence for field interactions within neuronal systems is also demonstrated by studies looking at the effects of artificially applied electric fields on the mammalian brain in vitro [33–36] as well as the human brain in vivo in therapies such as deep brain stimulation (DBS) for movement [37–39] and affective disorders [40, 41].

1.3 Synapses: How neurons communicate

For a neuron the input for the neuronal computations typically comes through the chemical synapses; highly specialized structures which provide for the main lines of communication between neurons within the nervous system (fig. 1.6). Forming between the presynaptic axon terminal and a part of the postsynaptic neuron, chemical synapses can be axodendritic, axosomatic or axoaxonal and number around 240 trillion in the cerebral cortex [83]. Communication through the synapse occurs when an action potential arrives at a presynaptic terminal causing the activation of voltage-gated calcium channels leading to a rise in the intracellular calcium concentration within the terminal. This triggers the probabilistic release and diffusion of neurotransmitters (packaged in synaptic vesicles within the terminal) into the synaptic cleft due to calcium-dependent exocytosis. The neurotransmitter then binds to specific receptors on the postsynaptic membrane causing specific changes in ionic permeabilities leading to depolarization and excitation or hyperpolarization and inhibition of the postsynaptic cell through postsynaptic potentials.

The chemical synaptic mechanism described above leads to an intriguing possibility of another kind of ephaptic communication, that within the synaptic cleft. In an excitatory synapse, activation will lead to the influx of positive current from the extracellular space through the synaptic cleft and into the postsynaptic neuron. This current will cause a slight depolarization within the intersynaptic space which would be sensed by the presynaptic voltage-gated calcium channels leading to an increase in the calcium influx and hence of neurotransmitter release in a positive feedback loop. The magnitude of the effect will depend on the amount of current flow and the intersynaptic resistance, being maximized for large invaginated synapses. This kind of ephaptic feedback has been postulated to occur in the CA3 area of the hippocampus, in the visual cortex [42–44] and within the retinal synapse, with some indirect experimental evidence [32].

Chemical synapses are not the only kind of structure specialized for neuronal

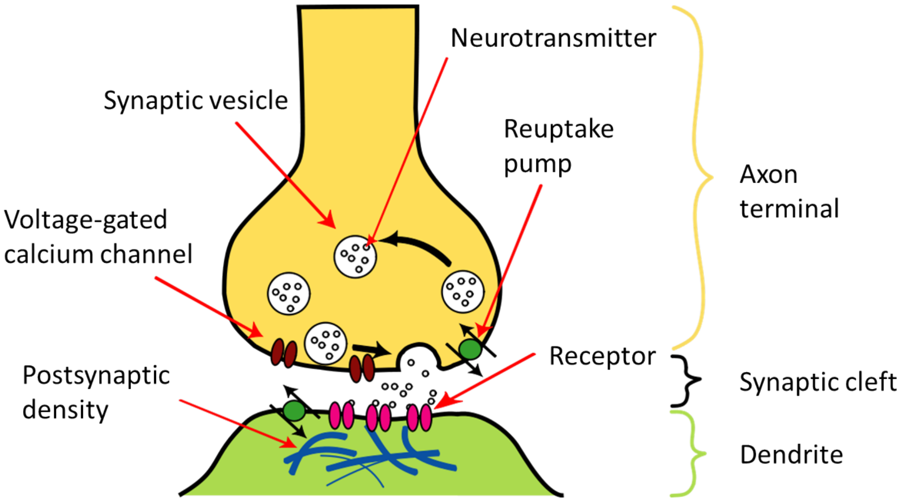

Figure 1.6: A schematic of a chemical synapse. An action potential in the presynaptic axon terminal triggers the entry of calcium ions into the terminal, which in turn causes the exocytosis of the neurotransmitter in to the synaptic cleft. The neurotransmitter then triggers excitatory or inhibitory postsynaptic potentials. (Image from Nrets at en.wikipedia, URL: http://en.wikipedia.org/wiki/File:SynapseIllustration2.svg).

communication within the nervous system. Electrical synapses or gap junctions mediate electrical transmission between adjacent neurons. Constructed from connexons, arrays of paired hexameric ion channels, gap junctions (fig. 1.7) allow small molecules to pass between the connected neurons, in turn allowing potentials (including action potentials) to spread between the cells at very short time scales. Gap junctions are known to play an important role in fast neuronal synchronization [45].

1.4 General equations - coupling the membrane to electric fields

A fully electric field-coupled model requires modeling of the extracellular (and intracellular) space. We consider an idealized single cell in an external electric field, where the domain is divided into purely conductive bulk intra and extracellular regions with constant conductivities, separated by an infinitely thin membrane. Assuming negligible magnetic effects and no diffusion currents, the current density in the bulk

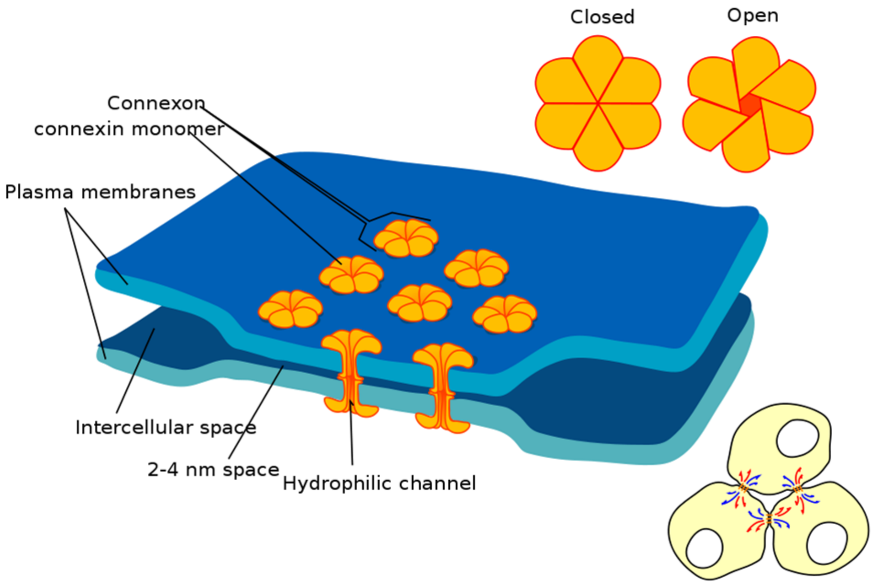

Figure 1.7: A schematic of a gap junction. Allowing for direct passage of ions in between cells, gap junctions or electrical synapses are a faster mode of intercellular communication then the chemical synapse. Composed of two hemichannels (connexons), gap junctions are formed between cells, which are 2-4 nm apart. Unlike the chemical synapses, gap junctions do not facilitate signal gain between cells. (Image from Mariana Ruiz Villarreal at en.wikipedia, URL: http://commons.wikimedia.org/wiki/File:Gap_cell_junction_en.svg)

domains is described by the simplified version of the Nernst-Planck equation

$$\mathbf{J} = -\sigma \nabla V \tag{1.5}$$

where σ is the conductivity and V is the potential. Application of charge conservation gives the continuity equation

$$\tfrac{\partial \rho}{\partial t} + \nabla \cdot \mathbf{J} = 0 \tag{1.6}$$

where ρ is the charge density. Combining Eqs. 1.5 and 1.6 above gives

$$\frac{\partial \rho}{\partial t} = \sigma \nabla^2 V \tag{1.7}$$

Now utilizing the differential form of Gauss' Law describing how the charge density influences the electric field

$$\nabla \cdot \mathbf{E} = \tfrac{\rho}{\epsilon} \tag{1.8}$$

$$\nabla^2 V = -\tfrac{\rho}{\epsilon} \tag{1.9}$$

where we have used the definition of the electric potential $E = -\nabla V$ to obtain Eq. 1.9, with E as the electric field and ϵ as the permittivity. Substituting from Eq. 1.9 in to Eq. 1.7 we get

$$\frac{\partial \rho}{\partial t} = -\frac{\sigma}{\epsilon}\rho \tag{1.10}$$

Thus we see that the charge density in the bulk domains goes to zero with a time constant $\frac{\epsilon}{\sigma}$. For our purely resistive model of the extracellular and intracellular domains we have $\frac{\epsilon}{\sigma} \rightarrow 0$, which implies that the charge density is always zero in the timescales of interest. This pure resistive model for the bulk domains implies that the capacitive effects of other (inactive) membranes in the bulk regions can be ignored as very little current passes through them. Thus all the time-dependence in the system comes from the oscillating electric field, and the membrane capacitance and voltage-gated conductances. This assumption is justified as the typical value of the time constant $\frac{\epsilon}{\sigma}$ is ~ 3 μs in tissue compared to the typical value of 10 ms for the membrane time constant. With $\rho = \frac{\partial \rho}{\partial t} = 0$ in the bulk domains, the intra and extracellular potentials V_i and V_e respectively, satisfy Laplace's equation [46, 47]

$$\nabla^2 V_i = \nabla^2 V_e = 0 \tag{1.11}$$

Thus in our theoretical framework we do not need to model the ionic charge distribution as is done in the Poisson-Boltzmann equation, and similarly considerations such as Debye screening can be ignored. To give the reader an intuitive picture of the charge distribution and current flow in a cell-field system, we have plotted the membrane potential V_m (fig. 1.8) and the current density (fig. 1.9) for a field-neuron system, with a steady-state and an oscillating field (at different phases). Note the reversal of the current flow and the neuron polarization which occurs when the field reverses orientation (at phases of π and $\frac{3}{4}\pi$ for a cosine oscillation).

The boundary conditions far away from the cell are determined by assuming that the cell is small compared to the extracellular region and is located away from the external boundaries, giving the extracellular potential

$$V_e(\mathbf{r}, t) = \mathbf{E} \cdot \mathbf{r} \qquad |\mathbf{r}| \to \infty \tag{1.12}$$

where $\mathbf{r}$ is the position where the potential is being calculated with respect to the origin and $\mathbf{E}$ is the uniform applied electric field. We assume that the potential across the membrane is discontinuous, with V_m as the difference between the intra and extracellular potentials. The transmembrane current density, J is given by

$$J = -\mathbf{n} \cdot (\sigma_i \nabla V_i) = c_m \frac{\partial}{\partial t} V_m + I_{ion}(V_m) = -\mathbf{n} \cdot (\sigma_e \nabla V_e) \tag{1.13}$$

where $\mathbf{n}$ is a unit normal pointing outward from the membrane and σ_i and σ_e are the intra and extracellular conductivities respectively. Eq. 1.13 ensures that J is continuous across the membrane and relates it to the membrane potential, resulting from the membrane and the bulk media properties.

1.5 Deriving the time-dependent solution from the steady-state solution

Using the general boundary-value problem above (Eqs. 1.11-1.13), we can derive a simple recipe for converting the steady-state solution to the oscillatory time-dependent one, where the stimulating uniform external field is given by $E_o + \hat{E}e^{i\omega t}$, where $i = \sqrt{-1}$ and ω is angular frequency of the sinusoidal field oscillations in time. If we assume the ansatz

$$V_e(\mathbf{r}, t) = V_e^o(\mathbf{r}) + \hat{A}_e(\mathbf{r})e^{i\omega t} \qquad r \geq a \tag{1.14}$$

$$V_i(\mathbf{r}, t) = V_i^o(\mathbf{r}) + \hat{A}_i(\mathbf{r})e^{i\omega t} \qquad r \leq a \tag{1.15}$$

for the time-dependent oscillatory solution, applying the bulk Laplace equation (Eq. 1.11) to the above solution form, results in the Laplacians of V_e^o, V_i^o, $\hat{A}_e$ and $\hat{A}_i$ equaling zero independently. So the initial general forms for V_e^o and $\hat{A}_e$ have to be identical to the initial general form of the steady-state solution $V_e(\mathbf{r})$, and the initial general form for V_i^o and $\hat{A}_i$ have to be identical to the initial general form of the steady-state solution $V_i(\mathbf{r})$.

A simple application of the far away boundary condition (Eq. 1.12) and the continuity boundary condition from Eq. 1.13 (i.e. $-\mathbf{n} \cdot (\sigma_i \nabla V_i) = -\mathbf{n} \cdot (\sigma_e \nabla V_e)$), and matching the oscillatory and non-oscillatory components across equations, shows that the constraints on V_e^o, V_i^o, $\hat{A}_e$ and $\hat{A}_i$ imposed by this boundary condition are exactly the same as those imposed on the steady-state solution. This implies that the solution form for these spatial variables is identical to the steady-state form.

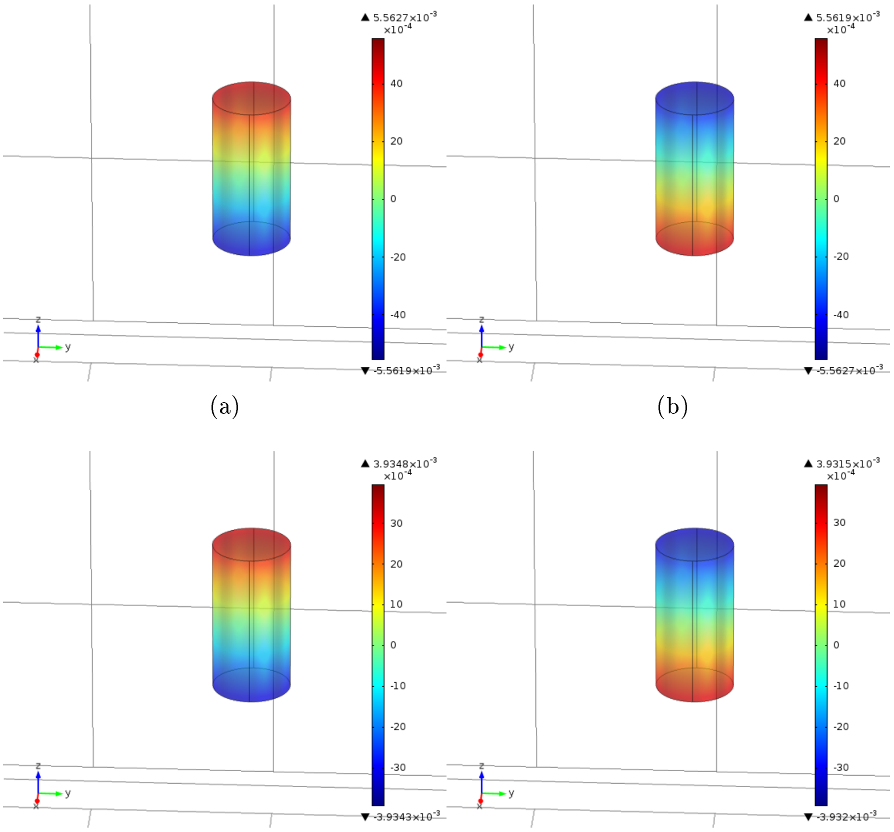

(a) (b)

(c) (d)

Figure 1.8: Polarization (induced membrane potential) of a passive cylindrical neuron (radius 2 μm and length 8 μm) in the presence of a uniform electric field of strength 1 V/m (steady-state field is in the positive z-axis direction i.e. bottom to top in the orientation of the above figures). The color scheme represents the membrane potential, $V_m = V_i - V_e$ (in mVs) which is a measure of the charge accumulation on the capacitive membrane (with c_m as the per unit area capacitance). The charge density in the bulk regions is zero (see above section 1.4). The results are derived using the finite-element scheme (section 2.5.2) a) Polarization due to the steady-state field. The neuron end proximate to the positive terminal is hyperpolarised (positive charge outside and negative inside) whereas the neuron end proximate to the negative terminal is depolarised (negative charge outside and positive inside), as expected. b) Polarization due to oscillating field (100 Hz) with oscillation phase of π. The field polarity is reversed with respect to a) and so is the polarization of the neuron. c) Polarization due to oscillating field (100 Hz) with oscillation phase of $\frac{\pi}{4}$. d) Polarization due to oscillating field (100 Hz) with oscillation phase of $\frac{3}{4}\pi$.

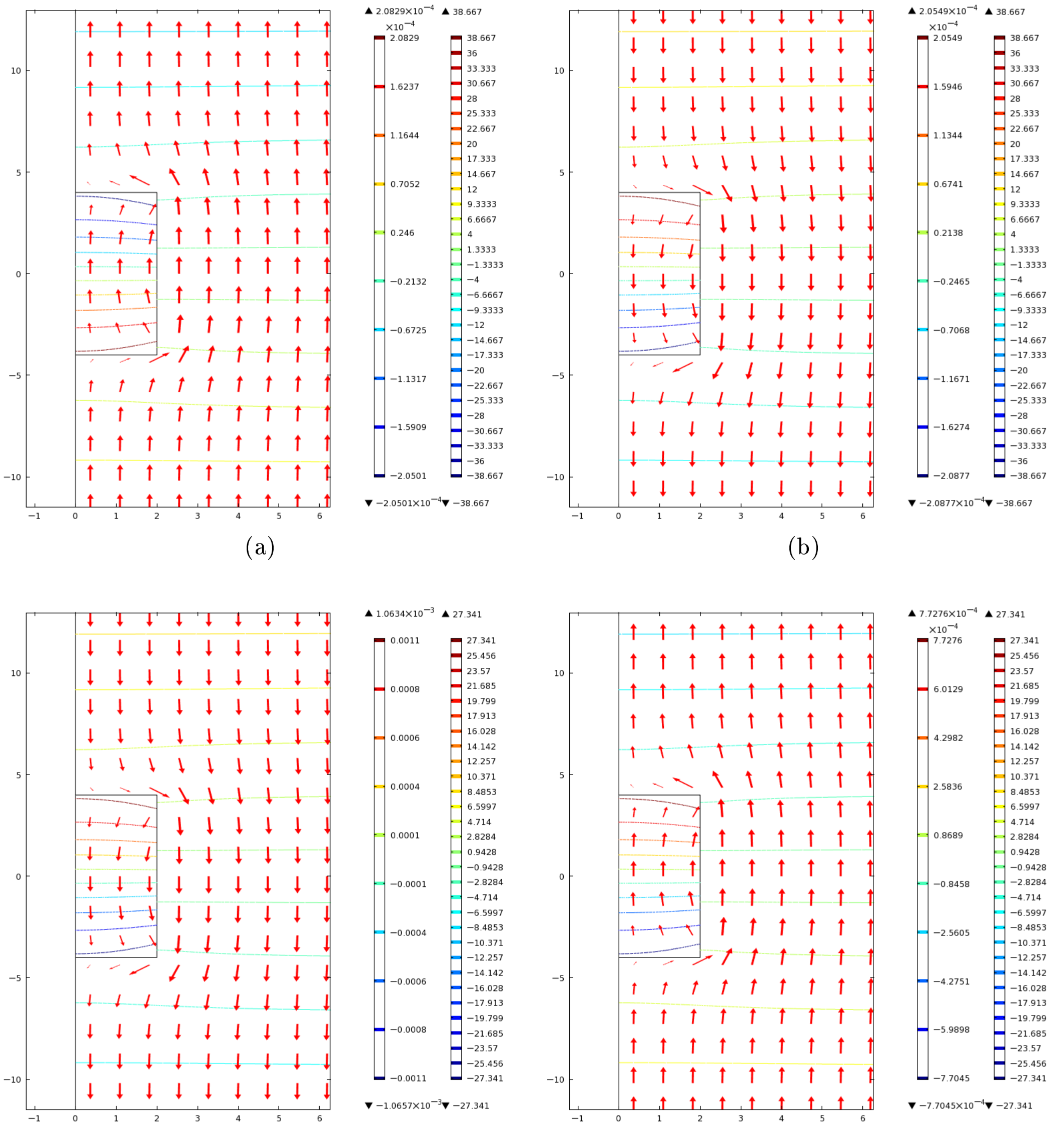

(a) (b)

(c) (d)

Figure 1.9: Current flow in a field-neuron system with a passive cylindrical neuron (radius 2 μm and length 8 μm) in the presence of a uniform electric field of strength 1 V/m (steady-state field is in the positive z-axis direction i.e. bottom to top in the orientation of the above figures). The arrows represent the direction and strength of the current density J in the bulk regions (in A/m^2). The contours are lines of constant potential with the color scheme representing the intracellular (left colourbar) and the extracellular (right colourbar) potential (in mVs). The results are derived using the finite-element scheme (section 2.5.2) a) Current flow due to the steady-state field. The current flows from the positive terminal to the negative one while diverting away from the high resistance membrane. b) Polarization due to oscillating field (100 Hz) with oscillation phase of π. The current direction is reversed with respect to a). c) Current flow due to oscillating field (100 Hz) with oscillation phase of $\frac{\pi}{4}$. d) Current flow due to oscillating field (100 Hz) with oscillation phase of $\frac{3}{4}\pi$.

Finally, applying the membrane boundary condition in Eq. 1.13, with $I_{ion} = g_L(V_i - V_e - E_L)$, we obtain

$$\begin{aligned} -\sigma_e \hat{\mathbf{n}} \cdot \nabla (V_e^o + \hat{A}_e e^{i\omega t}) = g_L \left(V_i^o - V_e^o + \left(\hat{A}_i - \hat{A}_e \right) e^{i\omega t} - E_L \right) \\ + i\omega c_m \left(\hat{A}_i - \hat{A}_e \right) e^{i\omega t} \qquad r = a \end{aligned} \tag{1.16}$$

Matching the non-oscillatory coefficients, we obtain

$$-\sigma_e \hat{\mathbf{n}} \cdot \nabla V_e^o = g_L \left(V_i^o - V_e^o - E_L \right) \qquad r = a \tag{1.17}$$

This again implies the identical constraint as that imposed on the steady-state solution by this boundary condition. So we can conclude that the solutions for V_e^o and V_i^o will be identical to the steady-state solutions with E replaced by E_o.

Matching the oscillatory components, we obtain

$$-\sigma_e \hat{\mathbf{n}} \cdot \nabla \hat{A}_e = (g_L + i\omega c_m) \left(\hat{A}_i - \hat{A}_e \right) \qquad r = a \tag{1.18}$$

$$-\sigma_e \hat{\mathbf{n}} \cdot \nabla A_e = \hat{g}_L \left(\hat{A}_i - \hat{A}_e \right) \qquad r = a \tag{1.19}$$

where $\hat{g}_L = g_L + i\omega c_m$. Here we see that the form of the constraint is exactly the same as that for the steady-state case, with the exception of $g_L \rightarrow \hat{g}_L$ as well as the absence of E_L. Therefore we conclude that the the solutions for $\hat{A}_e$ and $\hat{A}_i$ will be identical to the respective steady-state solutions, with E replaced by $\hat{E}$, with g_L replaced by $\hat{g}_L$ and $E_L = 0$.

1.6 Analytical modeling of field effects on single neurons - a discrepancy between theory and experiment

In order to develop a fully predictive theory for these biophysical effects, which occur at the single neuron and network levels, a microscopic understanding of the steady-state and dynamic field interactions with neuronal structures of varying geometries and biophysically detailed membrane properties is needed. Specifically, a knowledge of the induced membrane potential V_m, in response to a steady and oscillating electric field is a crucial first step for probing this interaction. The analytical approach to solving this problem for a passive spherical cell exposed to a uniform electric field was developed by Schwan [46, 47], which involves solving Laplace's potential equation over a domain consisting of highly polarizable intra and extracellular regions with conductivities σ_i and σ_e respectively, and a thin passive conductive membrane, yielding the expressions (as derived by Grosse and Schwan [47])

$$V_m = \frac{3/2 E a \cos\theta}{1 + a g_L \left(\frac{1}{\sigma_i} + \frac{1}{2\sigma_e}\right)} \qquad \text{static field} \tag{1.20}$$

$$\hat{V}_m = \frac{3/2 \hat{E} a \cos\theta}{1 + a(g_L + i\omega c_m) \left(\frac{1}{\sigma_i} + \frac{1}{2\sigma_e}\right)} \qquad \text{sinusoidally varying field} \tag{1.21}$$

where E and $\hat{E}$ are the magnitudes of the static and sinusoidally varying electric fields respectively, a is the cell radius, θ is the polar angle measured from the center of the cell with respect to the direction of the field and ω is angular frequency of the oscillating field (for a detailed derivation, see appendix D). In the physiological range (table 1.1), the expression $a g_L(\frac{1}{\sigma_i} + \frac{1}{2\sigma_e}) \ll 1$ and thus Eq. 1.20 can be approximated by the original version of the Schwan equation [48]

$$V_m = \frac{3}{2} E a \cos\theta \tag{1.22}$$

Eq. 1.22 reveals a linear relationship between V_m and the spherical radius a. Extending the solution method to non-spherical cells, Kotnik and Miklavcic [49] derived the analogous analytical expressions for prolate and oblate spheroidal cells with non-conductive membranes and with the applied field orientation parallel to the symmetry axis of the spheroids. Going further, Gimsa and Wachner [50–52] derived analytical expressions for V_m, for ellipsoids arbitrarily oriented with respect to a uniform and oscillating electric field. The resultant equations were simplified by Maswiwat [53, 54] avoiding complex expressions for the depolarizing factors used in the original derivation.

It is interesting to contrast Eq. 1.21 with the expression for V_m for a passive cell stimulated with direct current injection from an electrode, $I_{app} = \hat{I}_{app}e^{i\omega t}$ via whole-cell patch clamp (fig. 1.10a). The resulting differential equation is given by

$$c_m \frac{\partial}{\partial t} V_m = g_L(E_L - V_m) + I_{app} \tag{1.23}$$

The oscillatory solution to the above equation is given by

$$\hat{V}_m = \frac{\hat{I}_{app}}{g_L + i\omega c_m} \tag{1.24}$$

It is important to note that due to the large size of the electrode relative to the cell and the consequent uniform polarization, Eq. 1.24 is not spatially dependent. Both systems exhibit two regimes of behaviour. Firstly, the cell remains responsive up to the frequency given by the reciprocal of the respective time constant. Secondly, above this frequency the response starts to diminish with increasing frequency. The different time constants are characteristic of the time it takes for the cell to polarize in response to the stimulation. For the direct current injection case, the time constant is solely dependent on the membrane properties of the cell and is given by $\tau_m = c_m/g_L$, which for physiological parameter values (table 1.1) is around 10 ms. In the case of a field-stimulated spherical cell, the effective membrane time constant, now dependent on the cell radius and the intra and extracellular conductivities, is given by

$$\tau_{sph} = \frac{c_m}{\frac{2\sigma_e}{a\left(1+2\frac{\sigma_e}{\sigma_i}\right)} + g_L} = \frac{\tau_m}{1 + \frac{2\sigma_e}{g_L a\left(1+2\frac{\sigma_e}{\sigma_i}\right)}} \tag{1.25}$$

For a 10 μm cell and physiological values for the membrane and bulk media properties (table 1.1), $\tau_{sph} \approx 7 \times 10^{-4}$ ms. This reduction in the time constant means that the spherical cell remains responsive to field stimulation of $\sim$ 100 kHz frequency, whereas in the current injection case the response drops off after about 10 Hz (fig. 1.10b). This high-frequency response, predicted by the time-dependent version of the Schwan equation [46, 47] has been observed in vitro for field stimulated spherical Murine myeloma cells [55]. The same response however, had not been seen in experiments with pyramidal cells in rat hippocampal slices exposed to AC electric fields [36]. These cells are not compact but are highly elongated, suggesting that the shape of the cell may be important in determining its frequency response to an oscillating electric field.

Table 1.1: Parameters for the passive membrane. We have artificially set the resting membrane potential E_L to be zero for ease of notation. We note that for passive models, setting the resting potential to zero only offsets the resulting membrane potential by E_L and does not influence the membrane dynamics.

Parameter	Denotation	value
Extracellular medium conductivity	σ_e	0.2 μSμm^{-1}
Cytoplasmic conductivity	σ_i	0.2 μSμm^{-1}
Membrane leak conductance	g_L	1×10^{-6} μSμm^{-2}
Membrane capacitance	c_m	1×10^{-5} nFμm^{-2}
Assumed leak reversal potential	E_L	0 mV
Membrane time constant	τ_m	10 ms

1.7 The need for modeling electric field effects

The current level of understanding of how extracellular field interactions take place, endogenously between neurons and between artificially imposed fields and neuronal networks, is still being refined. In particular, there are two aspects which current modeling studies miss and which we want to address. Firstly, often a one-way field coupling is taken into account, where either the extracellular field influences the neuron but is not in turn influenced by the neuronal activity [56, 57] or the neuron influences the extracellular field but is not in turn influenced by the extracellular activity [58]. Secondly, the three-dimensional structure of the neuronal geometry is

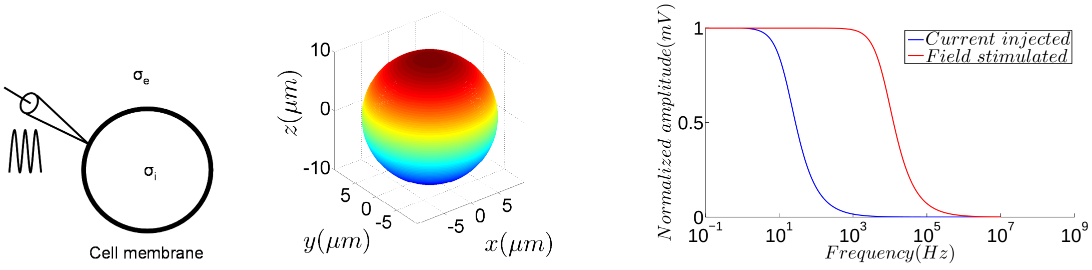

(a) (b)

Figure 1.10: Two alternative ways of cell stimulation. (a) (Left) Current injection via whole cell patch-clamp: The membrane behaves isopotentially and the cell response is dependent on the membrane conductance and capacitance, not on the extra and intracellular conductivities (Eq. 1.24). (Right) Membrane potential distribution on a spherical neuron of radius 10 μm in the presence of an electric field oriented along the x-axis. The membrane potential is dependent on the position on the cell as well as the extra and intracellular conductivities (Eq. 1.21). (b) Normalized membrane potential responses of a passive current-injected and a passive field-stimulated spherical neuron (of radius 10 μm) to sinusoidal stimulation at varying frequencies. The current-injected point-neuron response (Eq. 1.24) falls off at around 10 Hz stimulation frequency, whereas the field-stimulated response (Eq. 1.21) is sustained up to kHz frequencies. Parameter values are as in table 1.1.

not always fully taken into account as in the example of cable theory [19,56,57]. Our aim is to build three-dimensional, two-way coupled models which fully incorporate the feedback, which in reality exists between the neuron and the extracellular field as demonstrated recently by Frohlich and McCormick [59]. This will provide for realistic modeling of field effects on the nervous system in pathological, physiological and clinical contexts. The models will require a synthesis of two different modeling approaches used in two different fields; first the nonlinear time-varying behaviour of the membrane characterized by the Hodgkin Huxley equations [18] used extensively in theoretical and computational neuroscience, secondly the volume conductor behaviour in the bulk media found by the solution of Maxwell's equations.

In chapter 2 we explore the spatial dependence highlighted above (section 1.6), comparing the cable theory, finite-difference and finite-element methodologies. We expand the theoretical analysis above [46–54] to geometrically extended neurons modeled by finite cylinders of various radii-length ratios, focusing on the relationship between the neuron shape and its response at varying field frequencies. We use the finite-difference and finite-element methods for solving the analytically awkward problem of a finite cylinder in an oscillating electric field. We compare these results with those obtained through the extracellular cable equation and delineate the relationship between cellular shape, orientation and susceptibility to high-frequency electric fields. In particular we find that the neurons stimulated by extracellular fields exhibit an effective membrane time constant dependent on their electrotonic length and thus resolve the discrepancy in the literature, highlighted in section 1.6. In the context of cable theory (see section 2.2), the electrotonic length, L_e is the physical length of the neurite under consideration (L), measured in units of the electrotonic length constant

$$\lambda = \sqrt{\frac{a}{2r_L g_L}} \tag{1.26}$$

where a is the radius of the cable, r_L is the intracellular resistivity and g_L is the membrane leak conductance per unit area as before. λ represents the distance over which a current input in to the dendrite will spread and hence influence the membrane potential. Physically, a larger a and a smaller r_L would impose a smaller resistance to current spread (leading to a larger λ), whereas a larger g_L would lead to more current escaping in to the extracellular space (and hence a smaller λ).

In chapter 3 we investigate the behaviour of the passive cylindrical cell under point-source stimulation. Deriving the cable results using Green's functions, we compare them against the results obtained through our finite-element model. Due to the breaking of the axial symmetry by the non-uniform point-source field, a three-dimensional finite-element model is constructed. Both modeling methodologies reveal a novel form of localized frequency preference by the entirely passive neurons, the magnitude and frequency of which is dependent on the cell geometry and the distance between the neuron and the point-source. To our knowledge this "passive resonance" has not been reported in the literature before.

In chapter 4, we go on to incorporate a more biophysically detailed model of a quasi-active membrane into our field-neuron system known to lead to resonance at a characteristic stimulation frequency, manifesting itself as a peak in the induced voltage oscillations, when stimulated by current injection via whole-cell patch clamp [60, 61]. This phenomenon, found in many parts of the central nervous system, including in neocortical neurons [62–65] as well as hippocampal pyramidal cells [66, 67] and interneurons [67], arises from an interplay between the passive and active neuronal properties. In particular, resonance requires voltage-gated currents, which slowly oppose membrane potential changes [60]. Here we apply the linearized quasi-active membrane model to the spherical and the cylindrical field-neuron systems, elucidating the relationship between the neuronal shape and its subthreshold resonance in the presence of an oscillating electric field.

We then go on to construct a fully active field-neuron finite-element model incorporating Hodgkin Huxley type channels into the membrane. A significant and novel step towards modeling field-neuron systems with full two-way feedback between the neuron and the field, we use the spiking model to demonstrate that the "passive resonance" and high-frequency response of the passive neurons under point-source stimulation translates to the fully active neuron case.

Lastly, we go further and simulate the frequency response of passive neurons embedded in semi-infinite arrays and exposed to extracellular fields, validating the results obtained for the case of isolated neurons.

The work in this thesis can be categorized both as technique development and as finding novel aspects of field-neuron interaction. The findings below in relation to the frequency response of neurons to oscillating electric fields have important implications for understanding how endogenous and artificial electric fields may affect the behaviour of neuronal networks, a field which has been relatively understudied. Although the primary aim of the project was not technique development, the finite-element models developed for field-neuron interactions here, could have a greater impact on the field. Our FEM models have given us the capability to quickly and efficiently model neurons with realistic geometries and biophysics, and with full field coupling in a tissue environment. Given sufficient computational power, this advance could help answer the long standing questions about endogenous field-neuron interactions and also how artificial field intervention affects the nervous system.

Chapter 2

Modeling passive cylindrical neurons in uniform electric fields

2.1 Introduction

In section 1.6 we presented an apparent discrepancy in the literature with regards to the high-frequency response of cells exposed to oscillating electric fields. The analytical Schwan equation [46, 47] for spherical cells, predicts a membrane potential response to fields oscillating at frequencies even in the kHz range (fig. 1.10a). These results were experimentally verified by Marszalek et al [55] with experiments on murine myeloma cells exposed to electric fields generated with parallel plate platinum electrodes. Deans et al [36] conducted experiments on CA3 hippocampal slices exposed to oscillating fields generated through chlorided silver wire electrodes (fig. 2.1). The cells, positioned so that the CA3 axo-dendritic axis was parallel to the direction of the applied field, showed a point-neuron like behaviour with no high-frequency response (Eq. 1.24).

Furthermore, recent experiments performed by Anastassiou et al [57], using a 12 pipette setup for extracellular point stimulation with concurrent intra and extracellular recording from layer 5 neocortical pyramidal neurons in slices, demonstrate a

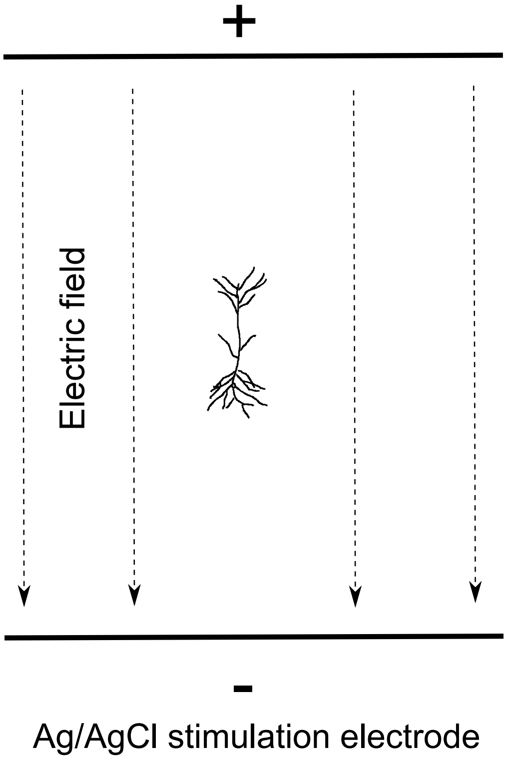

Figure 2.1: Schematic of a pyramidal neuron in an electric field. In a typical experimental setup, an in vitro neuronal slice is placed between parallel field electrodes, which are used to apply an electric field. The applied field is uniform far away from the cell and is in general aligned with the axo-dendritic axis of the neuron.

persistence of subthreshold oscillations in the membrane potential induced by the extracellular field oscillations of up to 100 Hz. These studies strongly suggest that the neuronal shape and orientation with respect to an applied extracellular field, shape the frequency response of the neuron. Thus one of the primary aims of this thesis is to examine in detail the relationship between neuronal shape and the membrane potential response, induced via electric field stimulation at varying frequencies.

2.2 Modeling finite cylindrical neurons in an extracellular field using the cable equation

The simplest method of modeling the neuronal membrane potential is to assume the neuron to be isopotential and hence point-like with only one voltage to solve for [68]. Neurons in reality have a spatial extent over which the membrane potential can vary considerably, with signal attenuation and delay occurring most severely through the long and narrow dendritic and axonal structures. Taking account of this spatial variation is vital in understanding how post synaptic potentials (PSPs) spread through the dendritic tree on to the soma and initial segment and also how the action potentials back-propagate from the soma on to the dendrites, processes important for understanding neuronal computation.

Neuronal processes are thus modeled using the "core conductor" approximation leading to the cable equation [69]. The key assumptions of the standard cable model are:

1. The neurite can be treated as a long and thin, purely conductive cylindrical core, with no radial extent. The intracellular space of the neurite is thus one-dimensional with all the current flow in the axial direction.
2. The extracellular space is isopotential and grounded, $V_e = 0$. This implies that most of the extracellular current flows in the radial direction and that no other neurons inject current in to the extracellular space.
3. The conducting core is surrounded by a passive membrane (fig. 2.2a), with the transmembrane current modeled by Eqs. 1.1 and 1.2.

For a more detailed review of the assumptions of standard cable theory, see chapter 2 of [83]. With the assumptions above, the membrane potential can be expressed as a function of the longitudinal spatial coordinate and time, $V_m = V_i(x, t)$. Taking a small cable section of length Δx and radius a (fig. 2.2a), its resistance to longitudinal

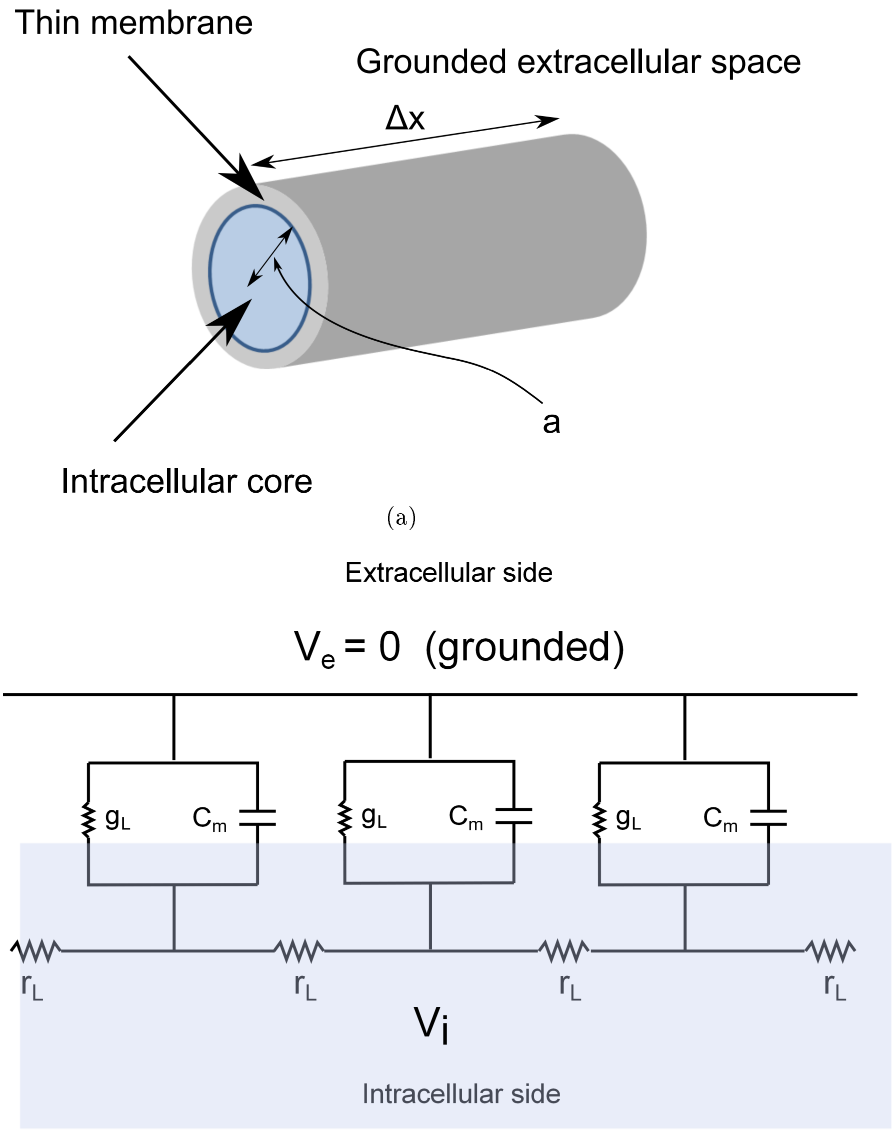

(a)

(b)

Figure 2.2: The core conductor model for a dendrite. a) A small section of a neuronal dendrite is modeled as a cylindrical cable with a thin membrane separating the intra and extracellular media. The extracellular potential is typically assumed to be constant and grounded. b) The dendritic cable is modeled as segments of parallel resistor-capacitor circuits joined in series by resistances r_L along the fiber. The capacitance c_m arises from the electrostatic forces acting through the lipid bilayer, the membrane resistance $1/g_L$ from the leak channels and the longitudinal resistances along the fiber r_L from the cytosol.

current is given by

$$R_L = \frac{r_L \Delta x}{\pi a^2} \tag{2.1}$$

where r_L is the longitudinal resistivity inside the cable. Using Ohm's Law, the longitudinal current in the increasing x direction is thus given by

$$I_L = \frac{\pi a^2 \left(V_i(x,t) - V_i(x+\Delta x, t)\right)}{r_L \Delta x} \tag{2.2}$$

which in the limit $\Delta x \to 0$ becomes

$$I_L(x) = -\frac{\pi a^2}{r_L} \frac{\partial V_i(x)}{\partial x} \tag{2.3}$$

where as before V_i is the intracellular potential (with $V_e = 0$). Applying conservation of current across the cable section, we see that

$$I_L(x) - I_L(x+\Delta x) = 2\pi a \Delta x \times c_m \frac{\partial}{\partial t} V_i + 2\pi a \Delta x \times g_L (V_i - E_L) \tag{2.4}$$

where the right hand side of the above equation represents the total transmembrane current for the cable section. Rearranging the above equation and taking the limit $\Delta x \to 0$, we obtain

$$-\frac{1}{2\pi a} \frac{\partial I_L(x)}{\partial x} = c_m \frac{\partial}{\partial t} V_i + g_L (V_i - E_L) \tag{2.5}$$

Substituting from Eq. 2.3 in to Eq. 2.5 and dividing through by g_L we arrive at the linear cable equation

$$\tau_m \frac{\partial V_i}{\partial t} + V_i = \lambda^2 \frac{\partial^2 V_i}{\partial x^2} \tag{2.6}$$

where $\tau_m = \frac{c_m}{g_L}$ is the membrane time constant and $\lambda = \sqrt{\frac{a}{2 r_L g_L}}$ is the electrotonic length constant (with a as the radius of the cable, r_L as the intracellular resistivity and g_L as the membrane leak conductance per unit area as before). The cable formulation of the one-dimensional neuronal cable can also be represented by an equivalent circuit diagram (fig. 2.2b). The passive dendritic cable thus acts as a low-pass filter selectively attenuating high-frequency voltage responses from synaptic inputs. The development and application of cable theory showed that passive dendrites, far from being isopotential, have a spatially varying membrane potential. Furthermore, the dendrites attenuate and delay the propagation of PSPs from the dendritic tree to the soma and the spike initiation zone.

It is important to note that the above cable equation and indeed most studies modeling neurons force the extracellular potential at the membrane to be grounded to zero (assumption 2 above), excluding the possibility of extracellular field interactions. In order to include the extracellular field coupling, the cable equation above (Eq. 2.6) has to be modified by including a non-zero extracellular potential V_e, leading to a membrane voltage $V_m = V_i - V_e$ driving the transmembrane currents on the left hand side of Eq. 2.6. The extracellular cable equation is thus given by

$$\tau_m \frac{\partial V_m}{\partial t} + V_m = \lambda^2 \frac{\partial^2 V_i}{\partial x^2} \tag{2.7}$$

Although the extracellular potential in the above cable model is now non-zero, it is still an imposed potential and does not receive any feedback from the neuron upon which it is imposed. Later on in this chapter we will investigate the validity of this assumption by constructing two-way coupled models of neurons interacting with applied electric fields.

The extracellular cable equation above has been applied in several studies to examine the effect of electric fields on neuronal behaviour. Tranchina and Nicholson [56] applied the above formalism for studying the behaviour of idealized neurons in electric fields. Assuming the soma to be an isopotential point, the axon to be myelinated, with evenly spaced nodes of Ranvier and using Rall's $\frac{3}{2}$-power rule to treat the dendritic tree as a cylinder, the authors derived analytical solutions for neurons in various orientations with respect to the field. Cartee and Plonsey [70] used the same formalism to study membrane potential rise times of finite cables in response to steps in extracellular electric field. Holt and Koch [71] used Eq. 2.7 to work out how the extracellular field generated by a spiking cell might effect a nearby passive cable. More recently, Anastassiou et al [72] used the same formalism to analyze the membrane potential response of one-dimensional cables and the reconstructed CA1 rat hippocampal pyramidal neuron, in the presence of inhomogeneous extracellular electric fields. According to our review, all these studies, while rigorously analyzing the steady-state response of the neurons to electric fields, neglect the frequency response of these cells to oscillating electric fields and the relationship between the neuron shape and its effective time constant. In the sections below, we demonstrate how the extracellular cable equation (Eq. 2.7) with appropriate boundary conditions can be used to relate the frequency response of the neuron to its shape and thus also to resolve the discrepancy in the literature highlighted in section 1.6.

2.3 Finite cable with sealed ends in a uniform field

2.3.1 Example calculation with a non-oscillating field

Most experimental studies involving extracellular electric field stimulation of cells or neuronal slices apply uniform fields using parallel plates [55] or wire electrodes [33, 35, 36], millimeters apart. The uniform field is said to simulate the effect of endogenous local field potentials (LFPs) [57, 59]. Using the cable formalism above, if we impose a linear non-oscillating extracellular potential, $V_e = -Ex$ along a finite cable, Eq. 2.7 at steady-state reduces to

$$\frac{d^2V_i}{dx^2} - \frac{V_i}{\lambda^2} = \frac{Ex}{\lambda^2} \tag{2.8}$$

Using standard techniques for solving second order linear differential equations, the general solution to Eq. 2.8 is given by

$$V_i = v_1 e^{x/\lambda} + v_2 e^{-x/\lambda} - Ex \tag{2.9}$$

where v_1 and v_2 are as yet undetermined constants. Taking the cable length to be L, spanning from $x = -\frac{L}{2} = -l$ to $x = \frac{L}{2} = l$, we apply the sealed-end boundary conditions $\frac{\partial V_i}{\partial x} = 0$ at $x = -l$ and $x = l$ to give

$$v_1 e^{-\frac{l}{\lambda}} - v_2 e^{\frac{l}{\lambda}} = \lambda E \qquad x = -l \tag{2.10}$$

$$v_1 e^{\frac{l}{\lambda}} - v_2 e^{-\frac{l}{\lambda}} = \lambda E \qquad x = l \tag{2.11}$$

Solving for v_1 and v_2 above and substituting into Eq. 2.9 gives

$$V_i = -\lambda E \left(\frac{e^{-\frac{l}{\lambda}} - e^{\frac{l}{\lambda}}}{e^{\frac{2l}{\lambda}} - e^{-\frac{2l}{\lambda}}} \right) \left(e^{x/\lambda} - e^{-x/\lambda} \right) + Ex \tag{2.12}$$

$$\Rightarrow \qquad V_m = V_i - V_e = \lambda E \frac{\sinh\left(\frac{x}{\lambda}\right)}{\cosh\left(\frac{l}{\lambda}\right)} \tag{2.13}$$

For electrotonically short neurons, i.e. in the limit $l \ll \lambda$, $V_m = Ex$, a simple linear potential profile representing a linear increase in membrane polarization from the center to the ends. For electrotonically long neurons, i.e in the limit $l \gg \lambda$,

$$V_m = \lambda E e^{\frac{x-l}{\lambda}} \qquad x \gg \lambda \tag{2.14}$$

$$V_m = 2Exe^{-\frac{l}{\lambda}} \qquad x \ll \lambda \tag{2.15}$$

Thus we see that electrotonically long cables become more eccentrically polarized in comparison with short ones (fig. 2.3), with the membrane potential near the center taking on a linear profile, much attenuated in magnitude by the $e^{-\frac{l}{\lambda}}$ factor in Eq. 2.15, and the membrane potential near the ends exponentially rising with x.

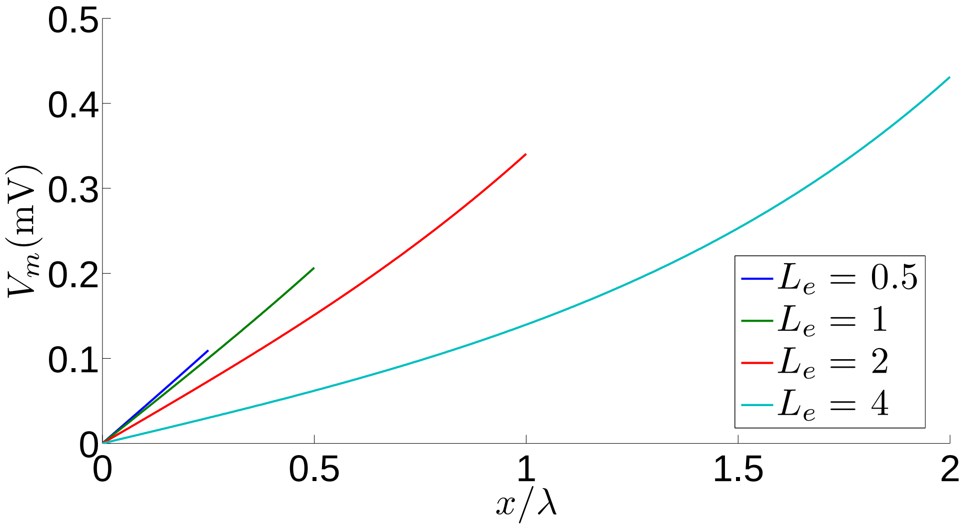

Figure 2.3: Steady-state membrane potential profiles for sealed-end cable neurons of various electrotonic lengths (L_e =0.5, 1, 2 and 4), in a uniform electric field oriented along the cable length. V_m is plotted against the distance along the cable x (measured in units of λ), with x only ranging from 0 to the cable half-length l, due to symmetry. Electrotonically longer cables are more eccentrically polarized than the shorter ones and V_m takes on a linear profile near the center of the cable ($x = 0$) for all electrotonic lengths. The parameters used to produce this figure are as given in table 1.1, with the cable radius $a = 2$ μm and $\lambda = 447.2$ μm.

2.3.2 Example calculation with an oscillating field

If we now impose a linear oscillating extracellular potential, $V_e = -Exe^{i\omega t}$, where ω is the angular frequency of the sinusoidal oscillations and $i = \sqrt{-1}$, Eq. 2.7 now becomes

$$\tau_m \frac{\partial V_i}{\partial t} + V_i + (1 + i\omega\tau_m)Exe^{i\omega t} = \lambda^2 \frac{\partial^2 V_i}{\partial x^2} \tag{2.16}$$

We apply the ansatz $V_i = A_i + B_i e^{i\omega t}$ to Eq. 2.16, giving

$$(1 + i\omega\tau_m)(B_i + Ex)e^{i\omega t} + A_i = \lambda^2 \frac{\partial^2 B_i}{\partial x^2} e^{i\omega t} + \lambda^2 \frac{\partial^2 A_i}{\partial x^2} \tag{2.17}$$

Matching the non-oscillatory components, we obtain the equation

$$\frac{\partial^2 A_i}{\partial x^2} - \frac{A_i}{\lambda^2} = 0 \tag{2.18}$$

With solution

$$A_i = a_1 e^{x/\lambda} + a_2 e^{-x/\lambda} \tag{2.19}$$

Matching the oscillatory components, we obtain the equation

$$\frac{\partial^2 B_i}{\partial x^2} - \frac{B_i}{\lambda_c^2} = \frac{Ex}{\lambda_c^2} \tag{2.20}$$

with the solution

$$B_i = b_1 e^{x/\lambda_c} + b_2 e^{-x/\lambda_c} - Ex \tag{2.21}$$

where λ_c is the complex length constant

$$\lambda_c = \frac{\lambda}{\sqrt{1 + i\omega\tau_m}} \tag{2.22}$$

Thus we have the complete solution for the intracellular potential

$$V_i = a_1 e^{x/\lambda} + a_2 e^{-x/\lambda} + \left(b_1 e^{x/\lambda_c} + b_2 e^{-x/\lambda_c} - Ex\right) e^{i\omega t} \tag{2.23}$$

Application of the sealed-end boundary conditions $\frac{\partial V_i}{\partial x} = 0$ at $x = -\frac{L}{2} = -l$ and $x = \frac{L}{2} = l$ to the above solution (Eq. 2.23) and matching the non-oscillatory and oscillatory components, we obtain

$$
\begin{aligned}
a_1 = a_2 &= 0 && \text{combining conditions at } x = -l \text{ and } x = l && (2.24)\\
b_1 e^{\frac{l}{\lambda_c}} - b_2 e^{-\frac{l}{\lambda_c}} &= \lambda_c E && x = -l && (2.25)\\
b_1 e^{-\frac{l}{\lambda_c}} - b_2 e^{\frac{l}{\lambda_c}} &= \lambda_c E && x = l && (2.26)
\end{aligned}
$$

Solving for b_1 and b_2 above and substituting into Eq. 2.23 gives the potential solution as

$$V_i = -\left(\lambda_c E \left(\frac{e^{-\frac{l}{\lambda_c}} - e^{\frac{l}{\lambda_c}}}{e^{\frac{2l}{\lambda_c}} - e^{-\frac{2l}{\lambda_c}}}\right)\left(e^{x/\lambda_c} - e^{-x/\lambda_c}\right) + Ex\right) e^{i\omega t} \tag{2.27}$$

$$\Rightarrow \qquad V_m = V_i - V_e = \lambda_c E \frac{\sinh\left(\frac{x}{\lambda_c}\right)}{\cosh\left(\frac{l}{\lambda_c}\right)} e^{i\omega t} \tag{2.28}$$

Thus we see that the amplitude of the oscillatory solution is obtained through the simple mapping

$$\lambda \to \lambda_c \tag{2.29}$$

applied to the steady-state solution (Eq. 2.13), where λ_c is as defined in Eq. 2.22. This mapping is also apparent through comparison of Eq. 2.20 with Eq. 2.8. It should be noted that the mapping in Eq. 2.29 is equivalent to the mapping $g_L \to g_L + i\omega c_m$ mentioned in section 1.5 above. At $x = l$, taking the complex amplitude of the expression in Eq. 2.28, we obtain

$$V_m = -\lambda_c E \tanh(l/\lambda_c) \tag{2.30}$$

It should also be noted that here and in later time-dependent expressions for V_m, the absolute value of the complex amplitude will be taken as the observable amplitude of the oscillations in the membrane potential. For electrotonically compact neurons

$(l \ll \lambda)$

$$V_m = El \qquad \omega\tau_m \ll \frac{\lambda^2}{l^2} \tag{2.31}$$

$$V_m = \frac{\lambda E}{\sqrt{i\omega\tau}} \qquad \omega\tau_m \gg \frac{\lambda^2}{l^2} \tag{2.32}$$

Thus for compact neurons, we see a cross-over of behaviour occurring at the field frequency $\omega_T = \frac{\lambda^2}{\tau_m l^2}$. The neuronal response, represented by the amplitude of the membrane potential oscillations induced by the external field, is sustained up to ω_T, after which the response attenuates with increasing field frequency. The reciprocal of the drop-off frequency gives the effective time constant

$$\tau_{cab} = \frac{1}{\omega_T} = \frac{l^2}{\lambda^2}\tau_m \tag{2.33}$$

which is characteristic of the time it takes for the finite cable to polarize in response to the dynamic field stimulation. Thus we see that for compact neurons the effective time constant for the frequency drop off is drastically shorter than that for the current-injected point-neuron case, where the time constant, $\tau_m = \frac{c_m}{g_m}$ is dependent only on the membrane properties of the neuron. For example for $l = 0.1\lambda$ and physiological values for the membrane, intracellular and extracellular parameters (table 1.1), $\tau_{cab} = 0.1$ ms.

In contrast, for electrotonically extended neurons $(l \gg \lambda)$

$$V_m = \frac{\lambda E}{\sqrt{1 + i\omega\tau_m}} \tag{2.34}$$

where the drop-off frequency is given by $\omega = \frac{1}{\tau_m}$, independent of the spatial dimensions of the neuron. Therefore we have the result that electrotonically compact "cable neurons", exposed to dynamic and uniform electric fields oriented along the cable axis, respond with a much faster time constant compared to the current-injected point-neuron (fig. 2.4). These compact neurons, much like the spherical cell case as

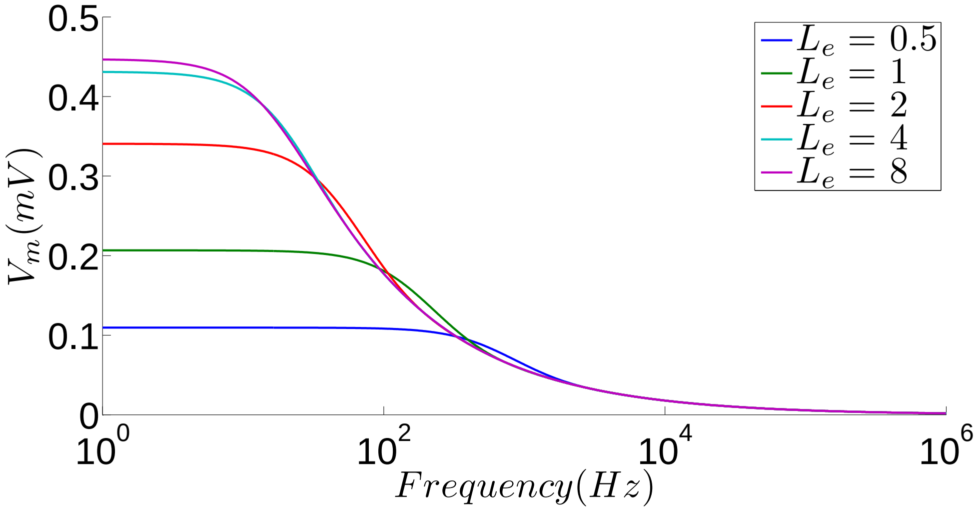

(a)

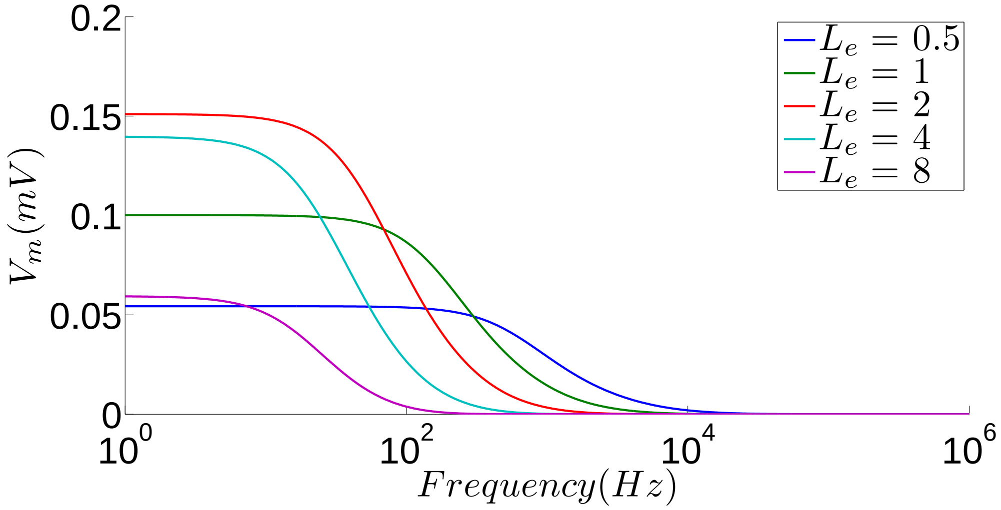

(b)

Figure 2.4: Electrotonically compact neurons remain responsive to high-frequency electric field stimulation. a) Frequency response of cable neurons of various electrotonic lengths (box top right) to electric field stimulation, with V_m measured at cable end ($x = l$). More compact neurons ($L_e = 0.5$, 1) exhibit a higher drop-off frequency indicating a shorter effective time constant (τ_{cab}) for membrane polarization. The frequency response of all the neurons converges at high frequencies, with the response of the shorter neurons never significantly exceeding that of the longer ones. b) Frequency response of cable neurons with V_m measured at $x = \frac{l}{2}$. Frequency selectivity is observed with differing high-frequency asymptotes and the high-frequency response of the compact neurons ($L_e = 0.5$, 1) exceeds that of the elongated ones ($L_e = 4$, 8). The parameters used to produce these figures are as given in table 1.1, with the cable radius $a = 2$ μm and $\lambda = 447.2$ μm. The neurons considered have sealed ends.

derived by Schwan [46, 47], are thus able to maintain their response to higher field frequencies (up to ∼250 Hz for electrotonic length $L_e = 0.5$ as opposed to ∼10 Hz for $L_e = 4$), in contrast with the drop-off frequency of about 10 Hz for the current-injected point-neuron case (fig. 1.10b). As the neuron becomes elongated, with its length becoming much larger than λ, it looses the high-frequency behaviour and behaves like the current-injected point-neuron.

The frequency behaviour of the end-point of the cable (fig. 2.4a) also shows that although the membrane potential response (V_m) for the more compact neuron is sustained up to higher frequencies, the actual magnitude only exceeds that of the more extended neuron by a very small amount before the responses reach the high-frequency asymptote (which is the same for both extended and compact neurons but different to the current-injected point-neuron case (Eq. 1.24)) of

$$V_m = \frac{\lambda E}{\sqrt{i\omega\tau_m}} \tag{2.35}$$

Thus for the cable end-point we see no selectivity at higher field frequencies; the response of the more compact neuron does not exceed that of the more extended. This however is not true for a different location on the cable. In the case when the measurement point is a quarter of the way up (or down) the cable ($x = \frac{l}{2}$) (fig. 2.4b), we see the compact neurons exceeding the extended ones in their membrane potential response, for example by 100 Hz the response of the $L_e = 8$ cable has nearly reached zero, whereas the response of the $L_e = 0.5$ cable is undiminished.

This high-frequency selectivity occurs because the longer cables are more eccentrically polarized along their length by the uniform field, in comparison to the compact cables, which follow a linear profile ($V_m = Ex$). As can be seen from Eq. 2.15, the V_m for longer neurons is much smaller than that for the shorter neurons for a given value of x close to the center of the cable (due to the $e^{-\frac{l}{\lambda}}$ factor with $l \gg \lambda$). Eq. 2.14 then shows us that for electrotonically long neurons, V_m takes on an exponentially growing profile near the ends (due to the $e^{\frac{x-l}{\lambda}}$ factor) which supersedes the V_m for the compact neurons. Therefore, as can be seen from fig. 2.3, for a given value of x close to the center, the electrotonically long neurons have a lower steady-state membrane potential than the compact ones. Thus the higher frequency drop-off points of the electrotonically compact cables ensure that their response supersedes that of the longer cables at high frequency, (for example when measuring at $x = \frac{l}{2}$, fig. 2.4b). This is also highlighted by the non-monotonic behaviour of V_m as measured at various fractional positions on the cable, plotted against increasing electrotonic length (fig. 2.5).

The above observations delineate the relationship between the neuron shape and its frequency response to oscillating electric fields; demonstrating that the more elongated the neuron is in the direction of the field, the larger its effective time constant (Eq. 2.33) and the lower the frequency up to which its V_m is entrained by the field (2.4). Previously, observed discrepancies (section 1.6) in the frequency response of neurons exposed to oscillating electric fields have been attributed to experimental limitations in accessing the extracellular space close to the neuron under observation (for calculating the membrane potential) [57]. The analysis above highlights the importance of cell shape and field orientation in determining the frequency response and offers a possible solution to these discrepancies. It should be noted that in this thesis the conclusions with regards to field orientation effects are qualitative, as we have not modeled field orientation explicitly. The relationship between cell elongation (in the field direction) and the reduction in the high frequency response, transfers logically to that between the field orientation for a given neuron and its frequency response.

In particular, it explains the differing frequency responses observed experimentally for the field stimulated, myeloma cells [55] and the hippocampal pyramidal neurons [36]. The compact spherical myeloma cells exhibit a high-frequency response in accordance with the time-dependent Schwan equation, while the lack of a high-frequency response in the hippocampal pyramidal neurons cannot be accounted for by the Schwan equation. Taking the geometrical elongation of the pyramidal neurons into account, the cable analysis above (2.30-2.35) explains this low-pass behaviour occurring due to the high l/λ ratios for the pyramidal neurons, while at the same time having the field orientation parallel to their dendritic-axonal axis. We note that the relationship between electrotonic compactness of a cell and its response time to an electric field has been elucidated upon previously using cable theory, but only in the context of membrane potential rise times in response to a sudden change in the applied field [70] and for ascertaining the electrotonic parameters of the cell [73]. The implications of the cable dimensions and field orientation for the drop-off frequency and the consequent high-frequency selectivity of more compact neurons have not been highlighted previously and these theoretical observations have not been linked to the discrepancy in frequency response between murine myeloma [55] and pyramidal cells [36]. The consequent prediction of this result is that cylindrical neurons with a compact orientation with respect to the field, will stay responsive even at higher frequencies. Thus it is hypothesized that in the case of pyramidal neurons, applying the field perpendicular to the axo-dendritic axis, will result in a neuronal response even at higher field frequencies. Indeed the limiting case for an infinitely long cylinder exposed to a field, oriented perpendicular to its axis can easily be derived by solving the full Maxwell's equations given in section 1.4 to give the membrane potential as

$$V_m = \frac{2E_o a \cos\theta}{1 + a(\frac{1}{\sigma_e} + \frac{1}{\sigma_i})(g_L + i\omega C_m)} \tag{2.36}$$

with the consequent effective membrane time constant

$$\tau_{cyl} = \frac{\tau_m}{1 + \frac{1}{g_L\left(\frac{1}{\sigma_e}+\frac{1}{\sigma_i}\right)a}} \tag{2.37}$$

which for physiological parameter values (table 1.1) is equal to 0.2 μs. For the derivation of Eq. 2.36, see appendix C.

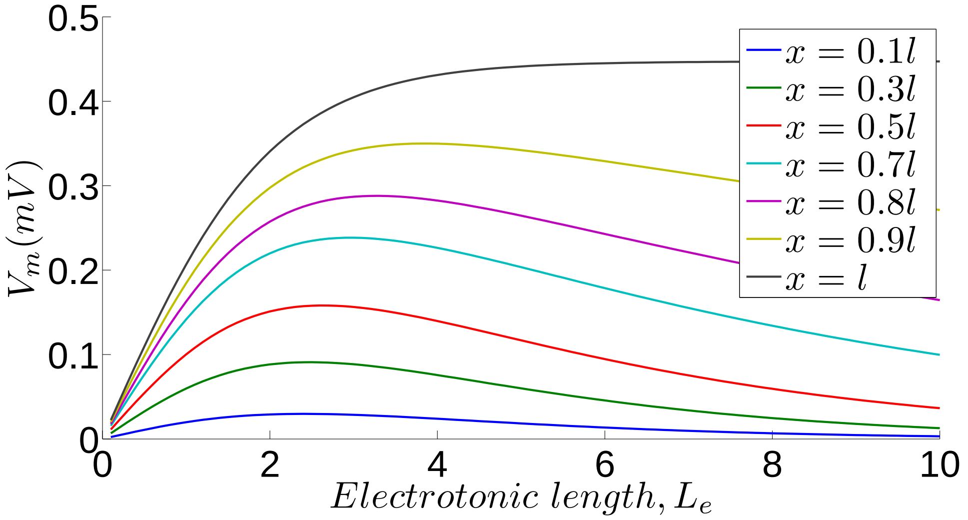

Figure 2.5: Steady-state V_m plotted against electrotonic length for various fractional positions (box top right) along the cable neuron exposed to a uniform field. The non-monotonic profiles indicate that due to the increasingly eccentric polarization profiles of the longer cable neurons, a shorter neuron will give a larger response for the same off-end fractional position, which in turn leads to the high-frequency selectivity for the shorter cable neurons (fig. 2.4). The parameters used to produce this figure are as given in table 1.1, with the cable radius $a = 2$ μm and $\lambda = 447.2$ μm. The neurons considered have sealed ends.

These findings could also help explain the high-frequency response (up to 100 Hz) observed for cortical neurons with unipolar field stimulation of the compact somata [57], in contrast with the current injection like response obtained with the parallel plate field stimulation of hippocampal neurons [36]. It is important to note however that for compact neurons the maximum DC value of the induced membrane potential would be lower due to the smaller cell size.

2.4 Finite cable with conducting ends in a uniform field

Dendrites and axons in reality are not sealed off at their ends and current flow occurs between the neurites and the soma as well as between the neurites and the extracellular space. Thus for comparison and completeness, we now derive the membrane potential response of a conducting-end cable exposed to a uniform electric field. We start with the general form of the steady-state solution in Eq. 2.9 obtained by solving Eq. 2.8

$$V_i = u_1 e^{x/\lambda} + u_2 e^{-x/\lambda} - Ex \tag{2.38}$$

where u_1 and u_2 are as yet undetermined constants. Exploiting the symmetry of the cable and the boundary conditions, we only model the cable spanning from $x = 0$ to $x = l = \frac{L}{2}$. By symmetry $V_i = 0$ at $x = 0$, thus

$$u_1 = -u_2 \tag{2.39}$$

$$V_i = u_1 \left(e^{x/\lambda} - e^{-x/\lambda}\right) - Ex \tag{2.40}$$

The conducting-end boundary condition at $x = l$, different from the electrically shorted condition ($V_i = 0$) commonly used, is given by the current density continuity equation, which matches the intracellular current density of the cable to the transmembrane current flowing out of the neuron

$$-\sigma_i \frac{\partial V_i}{\partial x} = g_L(V_i - V_e) \tag{2.41}$$

$$\frac{-\sigma_i u_1}{\lambda} \left(e^{l/\lambda} + e^{-l/\lambda}\right) + \sigma_i E = g_L u_1 \left(e^{l/\lambda} - e^{-l/\lambda}\right) \tag{2.42}$$

$$u_1 = \frac{\sigma_i E}{g_m\left(e^{l/\lambda} - e^{-l/\lambda}\right) + \frac{\sigma_i}{\lambda}\left(e^{l/\lambda} + e^{-l/\lambda}\right)} \tag{2.43}$$

Substituting into Eq. 2.40, we obtain

$$V_m = V_i - V_e = \frac{\lambda E \sinh\left(\frac{x}{\lambda}\right)}{\cosh\left(\frac{l}{\lambda}\right) + \frac{\lambda g_L}{\sigma_i} \sinh\left(\frac{l}{\lambda}\right)} \tag{2.44}$$

or

$$V_m = \frac{\lambda E \sinh\left(\frac{x}{\lambda}\right)}{\cosh\left(\frac{l}{\lambda}\right) + \frac{a}{2\lambda} \sinh\left(\frac{l}{\lambda}\right)} \tag{2.45}$$

In order to obtain the oscillatory solution for the conducting-end cable driven by the extracellular potential $V_e = -Exe^{i\omega t}$, we apply the mapping in Eq. 2.29 to the steady-state solution in Eq. 2.45 to give

$$V_m = \frac{\lambda_c E \sinh\left(\frac{x}{\lambda_c}\right)}{\cosh\left(\frac{l}{\lambda_c}\right) + \frac{a}{2\lambda_c}\sinh\left(\frac{l}{\lambda_c}\right)} \tag{2.46}$$

where again the oscillatory factor $e^{i\omega t}$ has been omitted. Thus the additional component due to the conducting-end boundary conditions is given by the term $\frac{a}{2\lambda_c}\sinh(\frac{l}{\lambda_c})$ in Eq. 2.46, which is proportional to $\frac{a}{\lambda}$.

For $x = l$, Eq. 2.46 becomes

$$V_m = \frac{\lambda_c E}{\frac{1}{\tanh\left(\frac{l}{\lambda_c}\right)} + \frac{a}{2\lambda_c}} \tag{2.47}$$

For electrotonically compact neurons ($l \ll \lambda$)

$$V_m = El \qquad \omega\tau \ll \frac{\lambda^2}{l^2} \tag{2.48}$$

$$V_m = \frac{2\lambda^2 E}{ia\omega\tau_m} \qquad \omega\tau \gg \frac{\lambda^2}{l^2} \tag{2.49}$$

Thus for compact conducting-end neurons, we see a drop-off frequency of $\omega_T = \frac{\lambda^2}{\tau_m l^2}$ and the effective time constant of $\tau_{cab} = \frac{1}{\omega_T} = \frac{l^2}{\lambda^2}\tau_m$, same as the sealed-end neurons. For electrotonically extended neurons ($l \gg \lambda$)

$$V_m = \frac{2\lambda^2 E}{a\sqrt{1 + i\omega\tau_m}} \tag{2.50}$$

Thus just like in the sealed-end case, the extended conducting-end cable has a time constant $\tau_m = \frac{c_m}{g_L}$ for the frequency drop-off, and thus behaves like the current-injected case in this respect. It should be noted however that the high-frequency asymptote for the conducting-end cable

$$V_m = \frac{2\lambda^2 E}{ia\omega\tau_m} \tag{2.51}$$

is different from that for the sealed-end cable (Eq. 2.35), leading to a slightly steeper attenuation at higher frequencies (figs. 2.7a and 2.7b).

With regards to understanding the difference between the sealed-end and conducting-end neurons, it is instructive to think about the cable results above in terms of the effective electrotonic length constant $\lambda_c = \frac{\lambda}{\sqrt{1+i\omega\tau_m}}$ and the ratio $\frac{l}{\lambda_c}$. For $l \ll \lambda$ and $\omega\tau \ll \frac{\lambda^2}{l^2}$, the cable neuron is effectively "compact" ($\frac{l}{\lambda_c} \ll 1$) and charge redistribution in response to the dynamic electric field occurs at the whole cell level. Thus the local difference in boundary conditions does not impact the membrane potential at the cable tips, hence the same low-frequency limit for the compact neurons with both boundary conditions, $V_m = El$. For $l \ll \lambda$ and $\omega\tau \gg \frac{\lambda^2}{l^2}$, the cable neuron is effectively long ($\frac{l}{\lambda_c} \gg 1$) and local distribution of charge becomes significant, hence the differing high-frequency limits for compact neurons under the two boundary conditions (figs. 2.7a and 2.7b).

For $l \gg \lambda$, the cable neuron is always effectively "long" ($\frac{l}{\lambda_c} \gg 1$) regardless of the frequency, leading to a high parallel bulk resistance. This in turn causes the charge redistribution (in response to a dynamic electric field) to occur locally through the membrane and not globally through the bulk media. Thus a difference in the local boundary conditions between sealed and conducting cable ends, leads to different low and high-frequency limits for the elongated neurons, in comparison with the compact ones (compare Eq. 2.34 with Eq. 2.50). It should however be noted that the difference in the cable-end boundary conditions does not have significant overall impact on the membrane potential response to the uniform electric field (fig. 2.6).

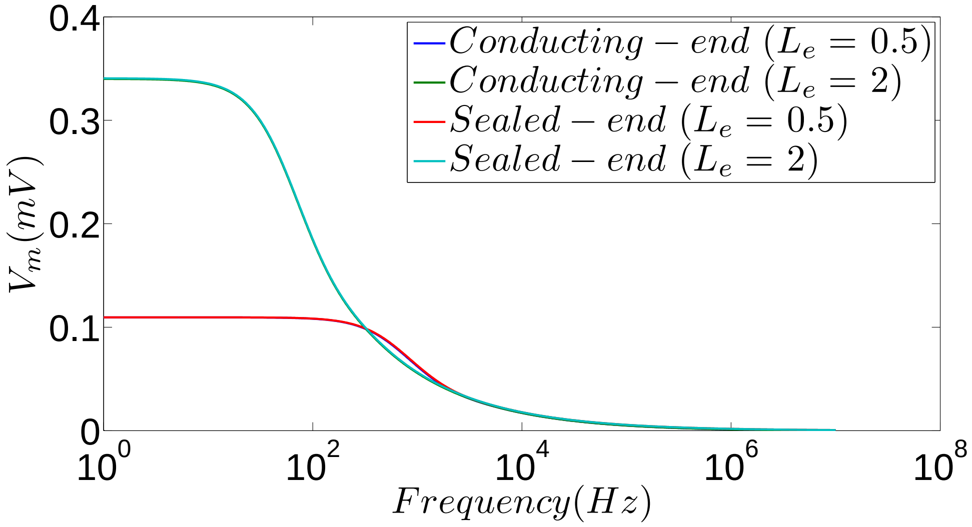

Figure 2.6: A difference in cable-end boundary conditions do not have a significant impact on the frequency response of the cable neurons. Frequency response for cable neurons of electrotonic lengths $L_e = 0.5$ and 2 for both sealed-end and conducting-end boundary conditions. The responses for the two boundary conditions are virtually superimposed at this resolution. The measurements are performed at $x = l$. The parameters used to produce this figure are as given in table 1.1, with the cable radius $a = 2\ \mu$m and $\lambda = 447.2\ \mu$m.

2.5 Modeling cylindrical neurons with finite radii in uniform electric fields - beyond the cable equation

The cable equation methodology given above [69] for modeling neurons in electric fields, approximates the neuronal processes as one-dimensional "core conductor" cables with no radial extent. Furthermore, the theory only provides for the cell to field coupling, where an imposed constant or dynamic electric field influences the transmembrane and intracellular potentials but is not in turn affected by the neuronal currents. In this thesis, we aim to go beyond cable theory and build three-dimensional neuronal models which incorporate full two-way coupling between the neuron and the applied electric field. Neurons have varied and elaborate three-dimensional geometries (fig. 1.1), which must be taken into account for considering electric field effects especially when considering those parts of the neurons which cannot be realistically modeled by one-dimensional cable structures, such as the soma. Furthermore,

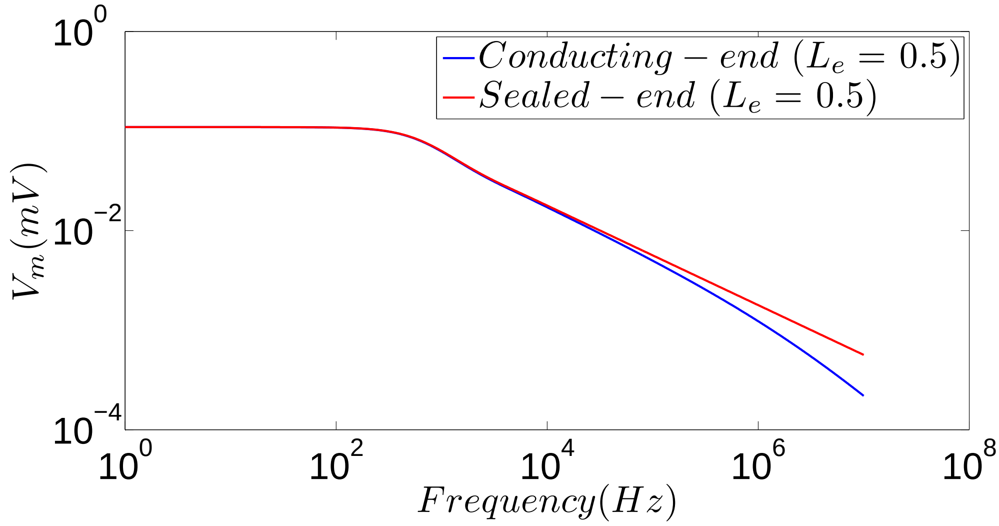

(a)

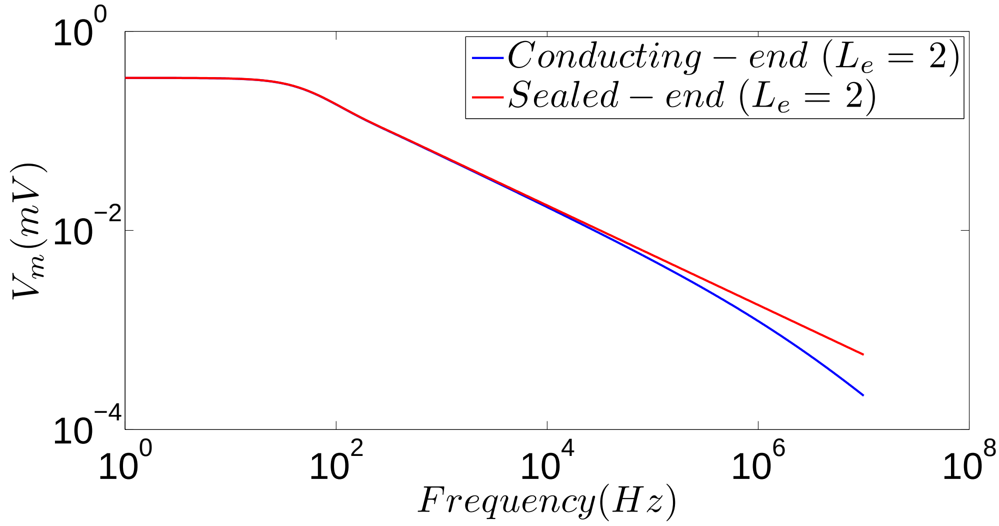

(b)

Figure 2.7: The high-frequency asymptotes differ for the sealed-end and the conducting-end cable neurons in uniform electric fields. a) Loglog plot for the frequency repose of the cable neuron of electrotonic length $L_e = 0.5$. b) Loglog plot for the frequency response of the cable neuron of electrotonic length $L_e = 2$. The difference between the boundary conditions occurs due to the neurons being effectively electrotonically long at higher field frequencies, causing a lack of global charge distribution during dynamic polarization. V_m is measured at the cable end ($x = l$) and the parameters used to produce these figures are as given in table 1.1, with the cable radius $a = 2$ μm and $\lambda = 447.2$ μm.

there is emerging evidence that full-field coupling, which in reality exists between the neurons and extracellular LFPs might be important in determining neuronal behaviour [59].

Thus we use Maxwell's equations (reduced to Laplace's equation) along with the transmembrane boundary conditions given above (Eqs. 1.11, 1.12 and 1.13) to determine the field-cell interaction. This methodology fully couples the bulk intra and extracellular potentials to the membrane potential. The steady-state analytical solution to this boundary-value problem for simple geometries can be derived by choosing a coordinate system which can model the surface of the cell and in which the Laplace's equation is separable, generating a general solution. The particular solution is then obtained by applying the boundary conditions (Eqs. 1.12 and 1.13). As mentioned in section 1.5, the time-dependent solution with an applied field $Ee^{i\omega t}$, oscillating with sinusoidal frequency ω, is then obtained by taking the solution form as $\hat{V}e^{i\omega t}$ for the membrane potential. The membrane boundary equations (Eq. 1.16) imply that the steady-state solution for V_m can be mapped on to the complex amplitude of the time-dependent solution, $\hat{V}$ by simply mapping g_L to $g_L + i\omega c_m$ in the steady-state solution. In this thesis, this mapping is also applied to the steady-state solutions obtained through the finite-difference and finite-element methods in order to obtain the respective time-dependent solutions. Eq. 1.21 was obtained by Schwan [47] by applying this methodology to the case of spherical neurons. In order to further investigate how the cell shape affects its response to an oscillating electric field, complex non-ellipsoidal shapes need to be studied, which are not accessible to an analytical approach. Thus we utilize the finite-difference and finite-element methods below to study the effect of a uniform electric field on a finite cylindrical neuron of radius a and half-length l exposed to a uniform electric field along its axis (figs. 2.9a and 2.9d). Due to the axial symmetry, this is a two-dimensional model with ρ and x as the radial and axial coordinates respectively.

2.5.1 Finite-difference method for a finite cylindrical neuron in a uniform electric field

The finite-difference method [74] is a numerical technique for solving differential equations, where the derivatives in the governing equations are replaced by finite-difference approximations. Taylor's series in one dimension (expanding around the point x_o) is given by

$$f(x_o + h) = f(x_o) + f'(x_o)h + \frac{f^{(2)}(x_o)}{2!}h^2 + ... + \frac{f^{(n)}(x_o)}{n!}h^n \tag{2.52}$$

The finite-difference expressions for the first and second derivatives can thus be derived from Eq. 2.52 as $f'(x_o) = \frac{f(x_o+h)-f(x_o)}{h}$ and $f^{(2)}(x_o) = \frac{f(x_o+h)-2f(x_o)+f(x_o-h)}{h^2}$, respectively. The differential equation under consideration can be discretized by replacing the derivatives by their finite-difference equivalents. For our model of a cylindrical neuron in a field (fig. 2.8), the Laplace equation in axial symmetric cylindrical coordinates is given by

$$\nabla^2 V = \frac{1}{\rho}\frac{\partial}{\partial\rho}\left(\rho\frac{\partial V}{\partial\rho}\right) + \frac{\partial^2 V}{\partial x^2} = 0 \tag{2.53}$$

where V is either V_i or V_e. The finite-difference equivalent of the above equation (after rearranging to make $V(i, j)$ the subject) is given by

$$V(i,j) = \frac{1}{4}(V(i,j+1) + V(i,j-1) + \frac{2i}{2i-1}V(i+1,j) + \frac{2i-2}{2i-1}V(i-1,j)) \tag{2.54}$$

where the potential $V(i, j)$ is now defined on a set of discrete mesh points i and j, the spatial indices in the radial and axial directions respectively. Thus the potential at a specific discrete point can be calculated in terms of the values of the potential at points around it. Using similarly discretized expressions for the boundary conditions, the value of potential at all the points in the solution domain can be calculated.

For solving the Laplace equation in cylindrical coordinates for our boundary-value problem (section 1.4), points were only placed in one quadrant of the plane (which is parallel to the applied field). The potentials in the other quadrants need not be calculated due to symmetry considerations (fig. 2.8).

Focusing on the boundary conditions for the membrane region, each mesh point is considered as a double point, with one point just inside and one just outside the membrane, both coupled via the membrane conductance g_L. A current conservation scheme is applied at each of the mesh points to arrive at the finite-difference membrane equations. For example for the membrane points along the axial direction ($\rho = a$), current conservation at the intracellular membrane point (i,j) implies

$$\begin{aligned} \tfrac{\sigma_i}{h}\left(V_i(i,j) - V_i(i-1,j)\right) + \tfrac{\sigma_i}{h}\left(V_i(i,j) - V_i(i,j-1)\right) = \\ \tfrac{\sigma_i}{h}\left(V_i(i,j+1) - V_i(i,j)\right) + g_L\left(V_e(i,j) - V_i(i,j)\right) \end{aligned} \tag{2.55}$$

where h is the spatial increment between the mesh points ($\rho = (i - \frac{1}{2})h$ and $x = jh$) and we have used the finite-difference form for the current expressions $\sigma_k \frac{dV_k}{dx}$ (with $k\epsilon\{i,e\}$). The expressions on the left hand side of Eq. 2.55 represent the currents going in to the intracellular membrane point (i,j), whereas those on the right hand side represent the currents going out, with $g_L\left(V_e(i,j) - V_i(i,j)\right)$ as the current through the membrane. Similarly, applying current conservation at the extracellular membrane point (i,j) we obtain

$$\begin{aligned} \tfrac{\sigma_e}{h}\left(V_e(i,j) - V_e(i,j-1)\right) + g_L\left(V_e(i,j) - V_i(i,j)\right) = \\ \tfrac{\sigma_e}{h}\left(V_e(i+1,j) - V_e(i,j)\right) + \tfrac{\sigma_e}{h}\left(V_e(i,j+1) - V_e(i,j)\right) \end{aligned} \tag{2.56}$$

The Eqs. 2.55 and 2.56 can then be manipulated to obtain expressions for $V_i(i,j)$ and $V_e(i,j)$ at the membrane point (i,j) in terms of the values of the the potential at the points around it

$$
\begin{aligned}
V_i(i,j) &= \frac{1}{\left(\frac{3\sigma_i}{h}+g_L\right)\left(\frac{3\sigma_e}{h}+g_L\right)-g_L^2}\left(\frac{\sigma_i}{h}\left(\frac{3\sigma_e}{h}+g_L\right)(V_i(i,j-1)+V_i(i+1,j)+\right. \\
&\quad \left. V_i(i-1,j))+\frac{\sigma_e g_L}{h}(V_e(i+1,j)+V_e(i,j+1)+V_e(i-1,j))\right) \qquad (2.57) \\
V_e(i,j) &= \frac{1}{\left(\frac{3\sigma_i}{h}+g_L\right)\left(\frac{3\sigma_e}{h}+g_L\right)-g_L^2}\left(\frac{\sigma_e}{h}\left(\frac{3\sigma_i}{h}+g_L\right)(V_e(i+1,j)+V_e(i,j+1)+\right. \\
&\quad \left. V_e(i-1,j))+\frac{\sigma_i g_L}{h}(V_i(i,j-1)+V_i(i+1,j)+V_i(i-1,j))\right) \qquad (2.58)
\end{aligned}
$$

The equations for the membrane on the "top" of the cylinder ($x = l$) are obtained by transposing Eqs. 2.57 and 2.58.

The field is assumed to be uniform "far away" from the cell (Eq. 1.12) due to the small size of the neuron relative to: a) the size of the field-inducing voltage plates and b) the distance between the neuron and the plates. To ensure that these conditions are satisfied in our finite-difference models, convergence studies were performed by increasing the size of the whole domain for a given cell size and ensuring that no significant change in V_m occurs due to the plate-neuron distance being too small.

The potential solution is given by the potential values V_{ij}, which simultaneously satisfy all of Eqs. 2.54-2.58. Using MATLAB version 7 (MathWorks Inc., 2011) to write the code, we used the iterative method of successive over-relaxation to arrive at the solution. For faster convergence, a multiscale methodology was utilized; successively superimposing solutions from coarser simulations, with large values of h on to finer grids (see appendix E).

Figure 2.9 shows the results of the steady-state (non-oscillating field) finite-difference simulations for cylindrical neurons of various sizes ($a \times l$ μm), with insulating membranes ($g_L = 0$). The maximum potential occurs at top and center of the cylinder ($\rho = 0$ μm, $x = l$ μm), with the membrane potential on the 4×4 μm cell being scaled up by a factor of two relative to the 2×2 μm cell as expected (fig. 2.9b). Looking at the membrane potential along the axial direction V_x (figs. 2.9a-2.9c), we

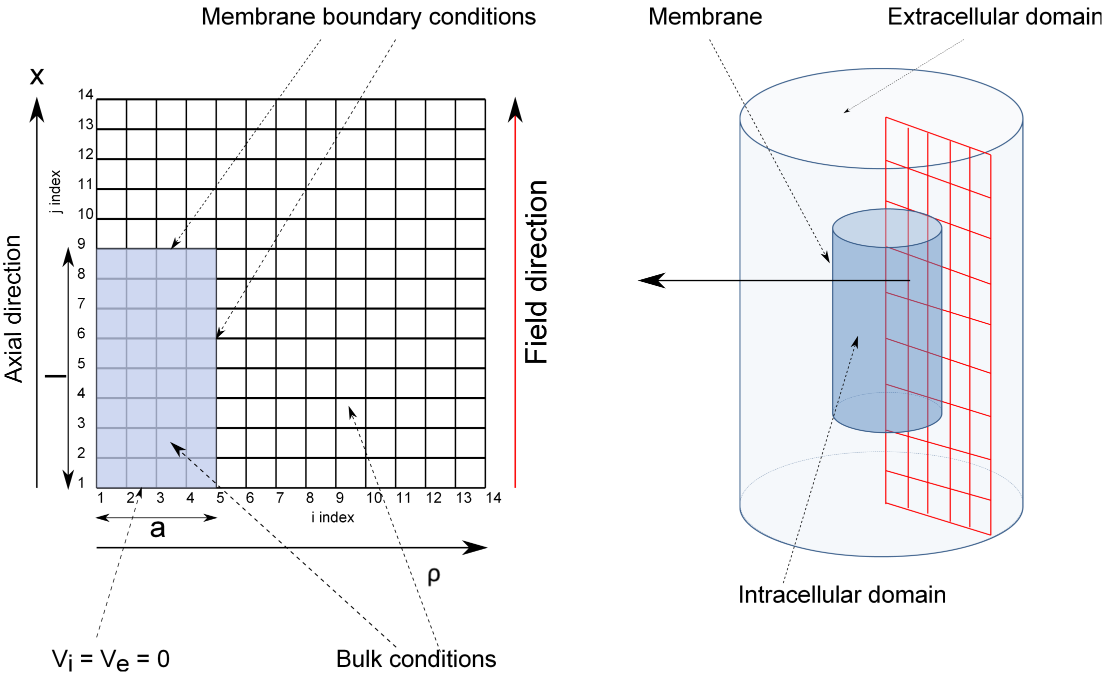

Figure 2.8: The finite-difference grid for a cylindrical neuron exposed to a uniform electric field, where a is the neuron radius, l is the neuron half-length, ρ is the radial coordinate, z is the axial coordinate, and V_i and V_e are the intra and extracellular potentials respectively. Due to the axial symmetry of the cylindrical system only a two-dimensional grid is required. Further symmetry conditions due to the uniform field require only a quadrant of the field-cell system to be simulated. Each point on the membrane boundary corresponds to two overlayed points, one intracellular and one extracellular, both coupled through the membrane conductance, g_L.

see that it can be roughly approximated by the negative of the potential resulting from the uniform applied field E

$$V_x = Ex \qquad \rho = a,\, 0 \leq x \leq l \tag{2.59}$$

as expected from the cable equation results for electrotonically compact neurons (Eq. 2.13). The approximation becomes more accurate for longer cylinders as the ratio l/a increases. This is to be expected as the one-dimensional cable equation does not take into account the radial extent of the cylindrical neuron and the feedback the cell gives to the extracellular field, in contrast to the finite-difference scheme (Eqs. 2.54-2.58). The membrane potential along the radial direction V_ρ (figs. 2.9d-2.9f), takes on the approximate form

$$V_\rho = El + Eaf\left(\tfrac{\rho}{a}\right) \tag{2.60}$$

with the function f approximately fitted to

$$f\left(\frac{\rho}{a}\right) = -0.454\left(\frac{\rho}{a}\right)^3 + 0.454 \tag{2.61}$$

The expressions in Eqs. 2.60 and 2.61 constitute a semi-analytical fit for the “top” of the steady-state cylindrical cell with an insulating membrane.

2.5.2 Finite-element method for a finite cylindrical neuron in a uniform electric field

The finite-difference method, though relatively easy to implement has the major drawback in that its application is limited to simple geometries. This is where the finite-element method (FEM) becomes most attractive as it is able to handle complex geometries with ease. FEM is a numerical technique which solves the governing differential equation approximately by discretizing the solution domain into “ele-

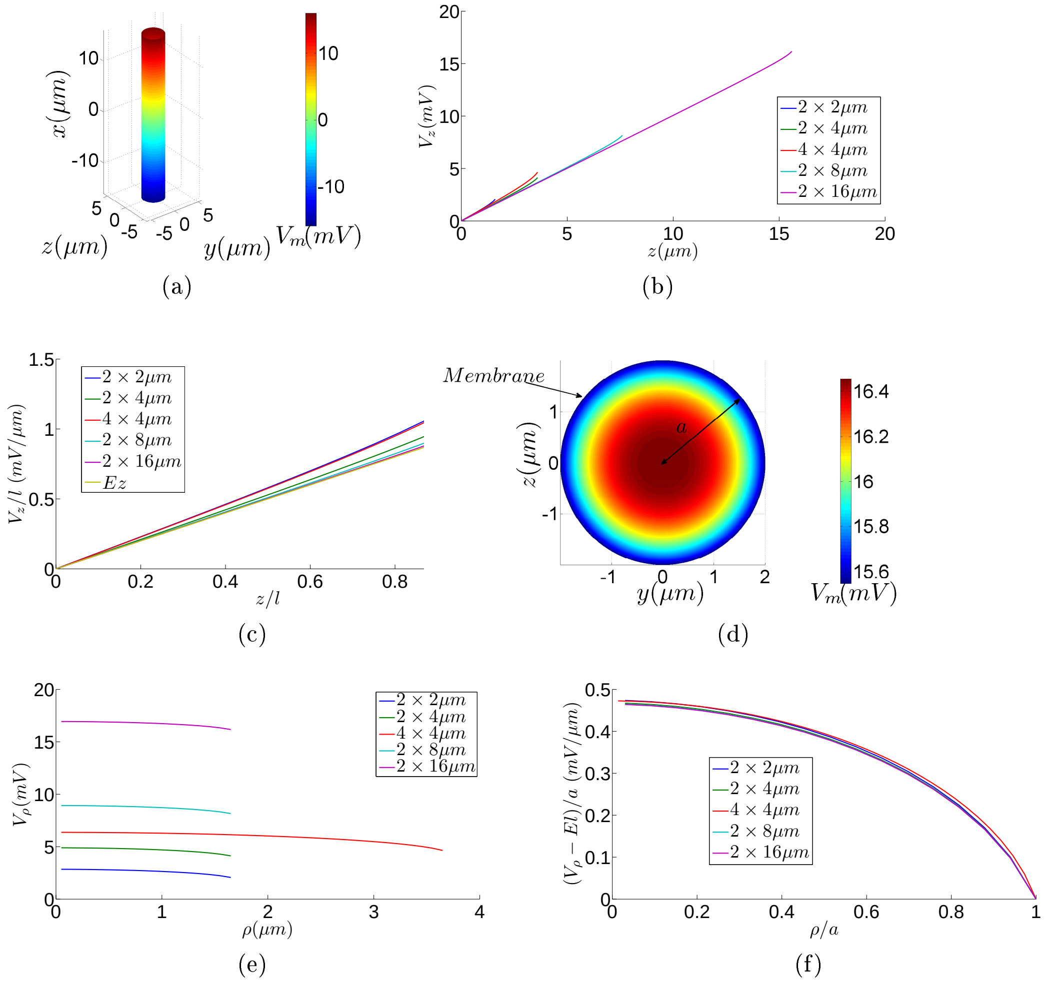

(a) (b) (c) (d) (e) (f)

Figure 2.9: Steady-state membrane potential distribution on a field-stimulated cylindrical neuron with a non-conductive membrane (finite-difference results). The applied field orientation is along the cylinder axis (x-axis) a) Membrane potential distribution on the side of the cylinder, V_x, plotted according to the linear fit (Eq. 2.59). As expected, the neuron is hyperpolarized at the positive field end, while being depolarized at the negative end. The cylinder is of size 2×16 μm (b) Variation of V_x along the axial direction for different cell shapes and sizes (finite-difference). (c) Normalized variation in the axial direction: V_x/l versus x/l. The plots for the different shapes and sizes converge for longer cylinders on to the function $V_x = Ex$. (d) Membrane potential distribution, V_ρ on the top of the cylinder ($x = l = 16$ μm), plotted according to the semi-analytical fit (Eqs. 2.60 and 2.61). V_ρ is axis-symmetric and highest at the center of the cylinder base. (e) Radial distribution of V_ρ at $x = l$, plotted for cylinders of various shapes (numerical simulations). (f) Plots of $(V_\rho - El)/a$ Vs ρ/a elucidating the function $f\left(\frac{\rho}{a}\right)$. An $a \times l$ neuron corresponds to a cell with radius a and half-length l.

ments" (fig. 2.10a) and using the "weak formulation" [75]. We utilize COMSOL Multiphysics version 4.1 (Burlington,. MA), a finite-element commercial software package optimized for simulating a variety of physical processes, especially coupled phenomena.

We note that the finite-element method and in particular COMSOL Multiphysics has been previously used to study neuronal interactions with electric fields [76] but in these investigations FEM is only used to calculate the imposed field given electrode geometries and bulk media properties, not incorporating the feedback from the neuronal targets.

We use the COMSOL model by Elia et al [85] as a starting basis for our model. The study in [85] considers a two-dimensional model of the axon with a prescribed intracellular current density mimicking currents due to the extracellular electric field. The model constitutes only one boundary interface between the intracellular and extracellular space. We on the other hand simulate the whole cell being exposed to actual extracellular fields induced by external potential plates.

Utilizing the symmetry, we construct a two-dimensional axial-symmetric model of the field-neuron system, with an intracellular bulk domain embedded within an extracellular bulk domain (fig. 2.10). We utilize the "AC/DC" module in COMSOL, setting up two different "electric currents" physics interfaces for the intracellular and extracellular domains, with the solution variables V_i and V_e respectively. We assume the membrane interface between the two bulk domains to be thin with a potential discontinuity at the membrane. The bulk domains are chosen to be purely conductive (with the dielectric constant set to zero) and the membrane boundary conditions are implemented by defining the normal current density $J = g_L(V_i - V_e)$ at the membrane boundary between the two domains, for both the physics interfaces. This common definition of J for both the physics interfaces couples the intracellular and the extracellular domains through the thin membrane interface. Thus in summary, the COMSOL variable V_i is active only in the intracellular domain and V_e only in the extracellular domain, while both are active on the membrane boundary.

The field is imposed by setting Dirichlet-type fixed potential boundary conditions on two of the outer boundaries (of the extracellular domain) perpendicular to the field direction (fig. 2.10b). In order to calculate the results for an oscillating field, the "frequency domain" study type is used with the complex transmembrane current density $J = (g_L + i\omega c_m)(V_i - V_e)$. This specific mode of the FEM simulator scans through the externally applied field frequencies ω, solving for the complex potentials at these frequencies. At the post-processing stages, the absolute values of the resulting potentials are taken.

It should be noted that the utilization of FEM using COMSOL with the above model constitutes a powerful method for understanding neuronal behaviour in the presence of extracellular fields, as it enables the modeler to model neurons with complex three-dimensional geometries taking into account full two-way coupling between the cell and the field.

2.5.3 Results and comparisons

The implementation of the finite-difference and finite-element schemes above in solving the boundary-value problem of the biological cell exposed to stationary and dynamic electric fields gives us the opportunity to compare against the results obtained from the cable method. In our numerical implementations we have assumed the more natural conducting-end boundary conditions, where instead of the cell being "shorted ($V_m = 0$)" or "sealed ($\frac{\partial V_m}{\partial r} = 0$)", the cell is assumed to have a leaky-capacitive membrane at the ends. Thus for comparison we use the derived membrane potential expression for conducting-end cables from above (Eqs. 2.45 and 2.46).

Plots of membrane potential (V_m) versus membrane conductance per unit area (g_L) for cells in stationary fields show very close agreement between the FEM and finite-difference methods for 2×4 μm and 2×16 μm neurons (fig. 2.11), verifying the results for both methods. The cable results however differ from the numerical

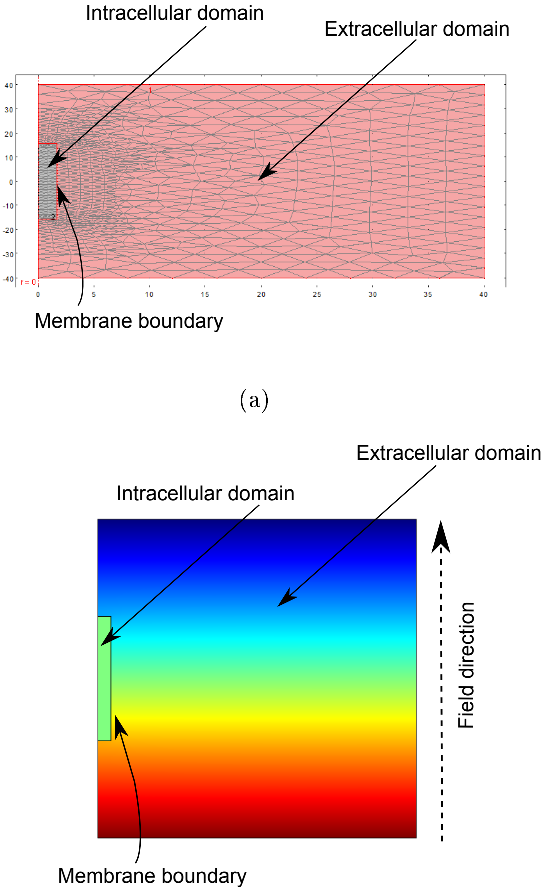

(a)

(b)

Figure 2.10: Results from the finite-element solution method (COMSOL Multiphysics). a) An example mesh for the two-dimensional axial symmetric problem. The elements are triangular and the mesh resolution increases inside the neuron and around the membrane to take account of the higher field strengths in those regions, in a computationally efficient manner. b) A two-dimensional potential plot for the cylindrical neuron in a uniform field.

ones, producing a lower V_m in the low g_L range (fig. 2.11). This discrepancy is higher for the more compact 2×4 μm cell (12 % lower) then for the 2×16 μm cell (~4 % lower). The g_L-variation results are reflected in the time-dependent oscillatory results with V_m plotted against field frequency (fig. 2.12).

Long neurons versus compact neurons

In the previous section we have shown close agreement between the finite-difference and the FEM results. We now go on to ascertain the differences between the one-dimensional, one-way coupled cable model and the two-dimensional, two-way coupled FEM model.

Figure 2.13a shows that for neurites of lengths comparable with the electrotonic length constant, the FEM and cable models agree very closely through the whole frequency range and thus the analytical cable model can be used to ascertain the drop-off frequencies for non-compact neurons using the expression for the effective time constant (Eq. 2.33). Small differences occur at high frequencies, with the FEM response overtaking that of the cable model (figs. 2.13b and 2.13c).

In the case of compact neurons (fig. 2.14) we see a significant difference between the two models in the low-frequency limit, with the cable model producing a lower value of the membrane potential (by 23% for the 10×10 μm neuron and by 14% for the 10×20 μm neuron). The drop-off frequencies are again identical to the cable model, with the membrane potential for the FEM model falling very slightly below that for the cable model in the high-frequency limit (figs. 2.14b and 2.14c).

This significant difference highlights the effect of the feedback received by the extracellular field from the electrotonically and spatially compact cell. The applied electric field changes the membrane potential of the neuron, which in turn distorts the extracellular field near the neuron from a perfectly axial configuration (fig. 2.15). From an electric current point of view, the currents generated by the application of a voltage across the cell take the path of least resistance across the system, flowing

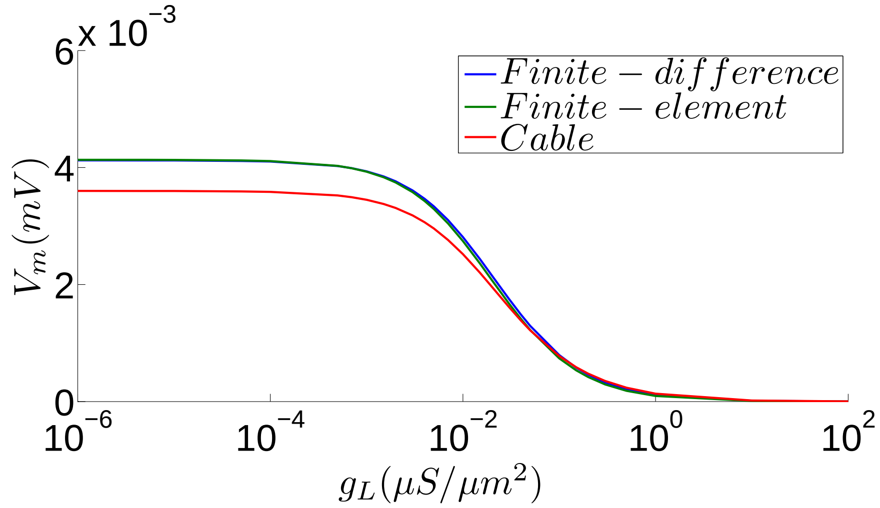

(a) 2×4 μm neuron

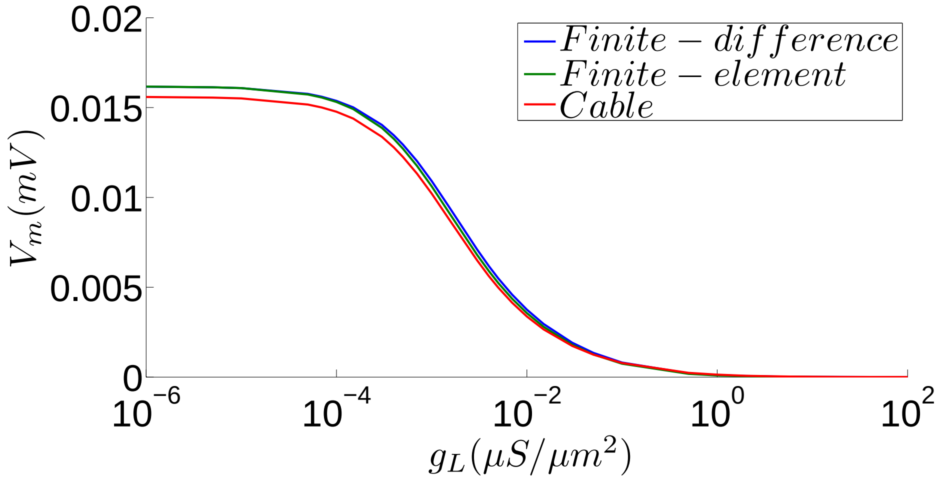

(b) 2×16 μm cell

Figure 2.11: Membrane potential versus g_L comparison between finite-difference, finite-element and cable methods for a) 2×4 μm and b) 2×16 μm (compact) cylindrical neurons. The finite-element and finite-difference results agree very closely but both differ significantly from the cable results with the difference greater for the more compact 2×4 μm neuron. The neurons considered have conducting ends. V_m is measured at the cable end $(x = l)$ and the parameters used to produce these figures are as given in table 1.1, with the cable radius $a = 2$ μm and $\lambda = 447.2$ μm.

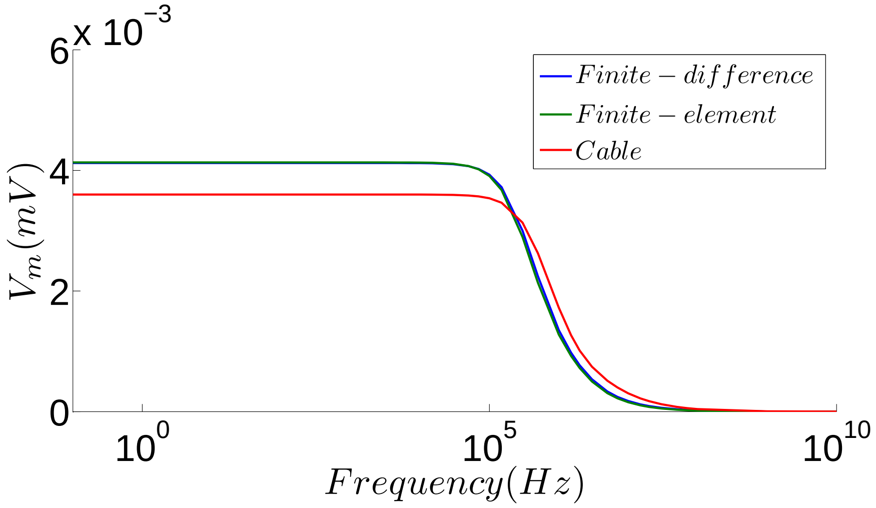

(a) 2 × 4 μm neuron

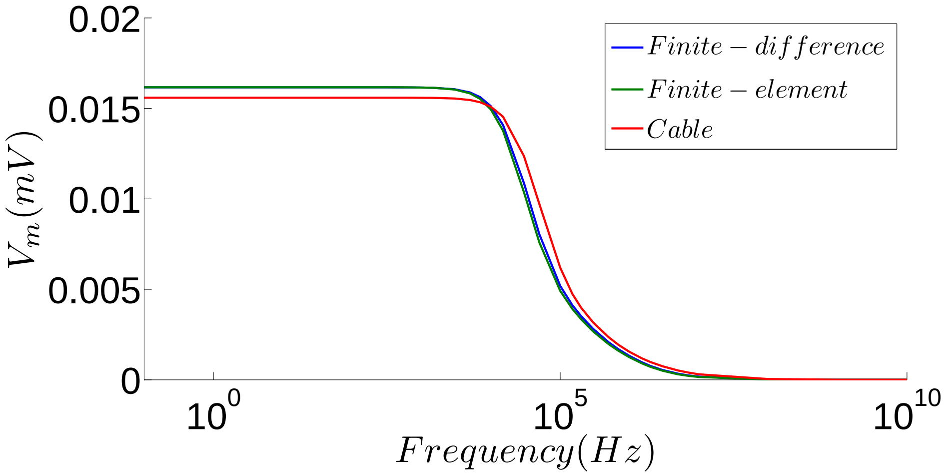

(b) 2 × 16 μm neuron

Figure 2.12: Frequency response comparison between finite-difference, finite-element and cable methods for a) 2×4 μm and b) 2×16 μm (compact) cylindrical neurons. As in the steady-state case with g_L-variation (fig. 2.11) the finite-difference and finite-element methods agree closely but differ from the cable results, with an increasing error for more compact neurons due to cell-to-field feedback. The neurons considered have conducting ends. V_m is measured at the cable end ($x = l$) and the parameters used to produce these figures are as given in table 1.1, with the cable radius $a = 2$ μm and $\lambda = 447.2$ μm. An $a \times l$ neuron corresponds to a cell with radius a and half-length l.

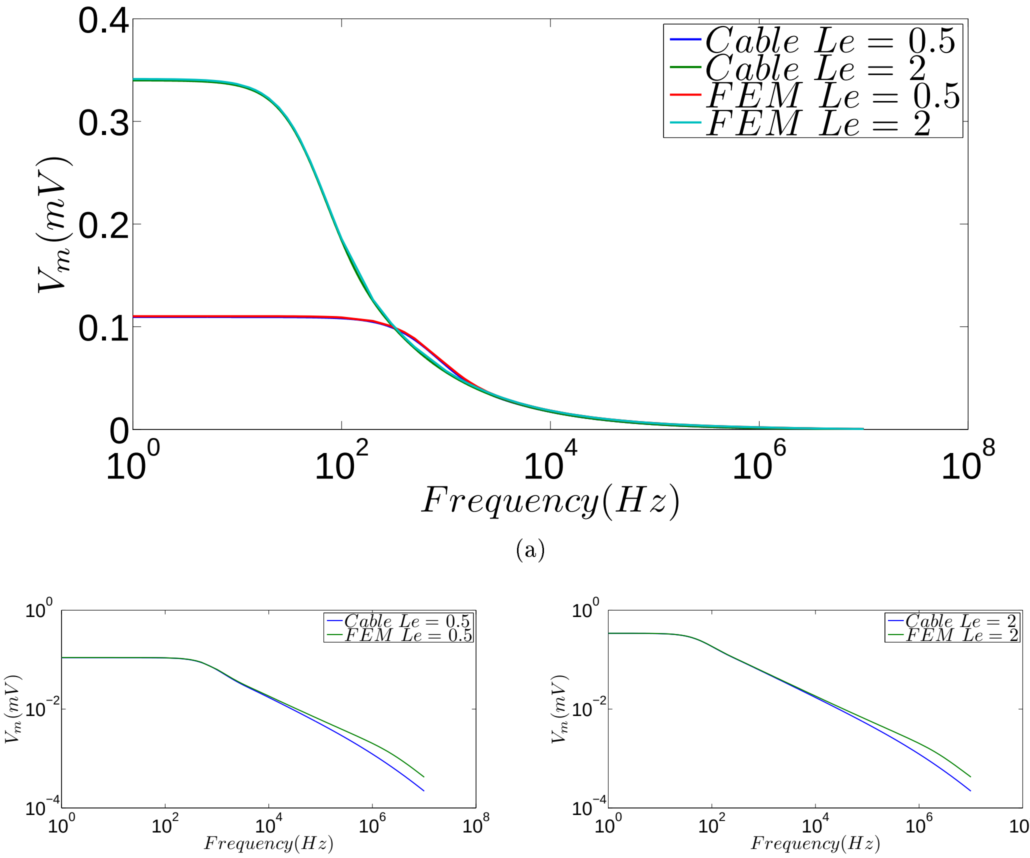

(a)

(b)

(c)

Figure 2.13: Comparison between finite-element and and cable methods in ascertaining the frequency response for cylindrical neurons of electrotonic lengths comparable to λ, in an oscillating electric field. a) The frequency responses of the $L_e = 0.5$ and 2 neurons show close agreement between the finite-element and the cable methods. The finite-element response slightly overtakes that of the cable method for both b) $L_e = 0.5$ and c) $L_e = 2$ neurons at high frequencies. The neurons considered have conducting ends. V_m is measured at the cable end $(x = l)$ and the parameters used to produce these figures are as given in table 1.1, with the cable radius $a = 2$ μm and $\lambda = 447.2$ μm.

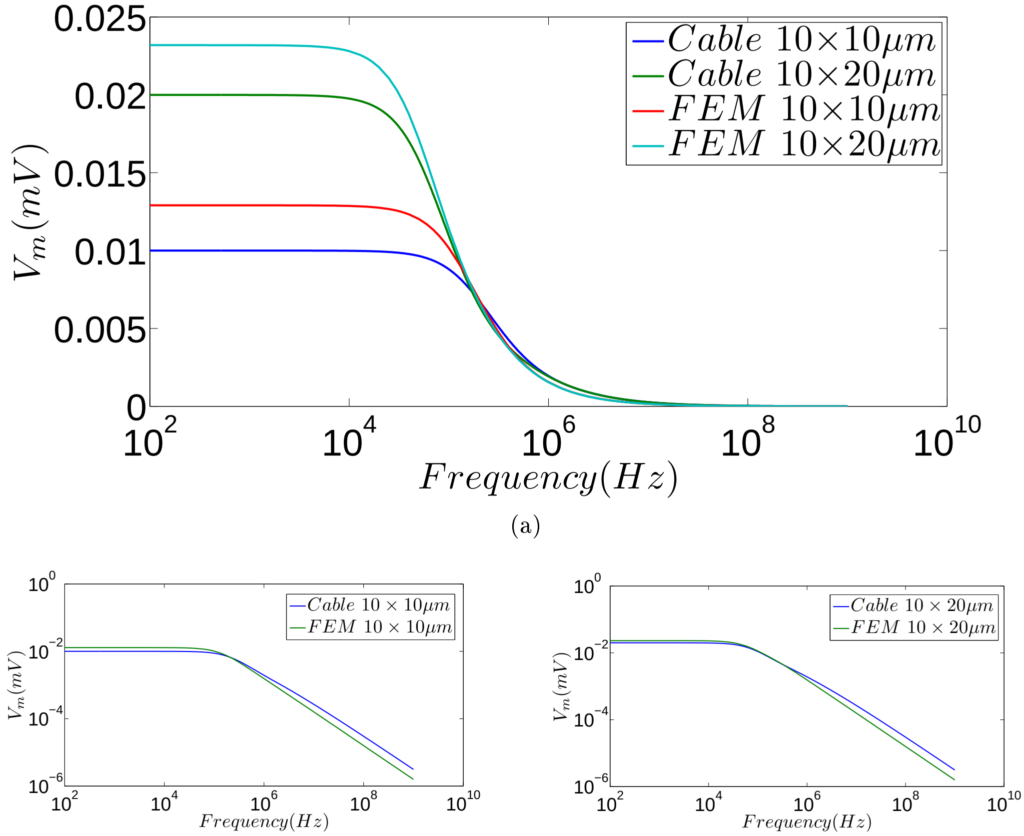

(a)

(b) 10×10 μm neuron

(c) $10{\times}20$ μm cell

Figure 2.14: Comparison between the finite-element and cable methods in ascertaining the frequency response for compact cylindrical neurons, in an oscillating electric field. a) The frequency of responses for the $l = 10$ and 20 μm neurons differ significantly between the finite-element and the cable methods in the low-frequency limit. The log-log plots also reveal that the finite-element response falls slightly below that of the cable method for both b) $10\times10\mu$m and c) $10\times20\mu$m neurons at high frequencies. The drop-off frequencies are identical for both models. The neurons considered have conducting ends. V_m is measured at the cable end ($x = l$) and the parameters used to produce these figures are as given in table 1.1, with the cable radius $a = 10$ μm and $\lambda = 1000$ μm. An $a \times l$ neuron corresponds to a cell with radius a and half-length l.

around the neuron, avoiding the high resistance cell membrane. This generates radial currents (fig. 2.15), which lead to higher polarization across the radial extent of the cell and a higher membrane potential. This feedback from the cell to the field is not modeled in the cable methodology with an imposed field, and highlights the importance of fully coupled models in understanding field-cell systems. Its is worth noting that electrotonically, these cells are very compact ($L_e = 0.02$ for the $10 \times 10\ \mu$m neuron) and serve as models for cell bodies rather than elongated neurites when the field is parallel to the axo-dendritic axis. With a field configuration perpendicular to the long axis of the neuron, we again expect to the see significant radial polarization, a situation which cannot be modeled with the one-dimensional cable equation.

Thus in conclusion we have checked the cable equation results above and hence the findings of section 2.3, using fully-coupled three-dimensional finite-difference and finite-element models. We have shown that the drop-off frequency, which marks the transition in the membrane potential response from a low-frequency plateau to a frequency-dependent attenuation at higher frequencies is accurately predicted by the derived cable results. Lastly, through the numerical simulations, we have shown that in the case of spatially compact neurons, the magnitude of the low-frequency response is significantly underestimated by the cable equation, due to a lack of feedback from the compact cell. The numerical schemes above and in particular the COMSOL/FEM model offer a novel methodology for simulating the effect of electric fields on neurons with full two-way coupling, taking into account the three-dimensional complexity of the cells, including dendritic trees and compact cell bodies, going beyond the capability of the one-dimensional cable equation.

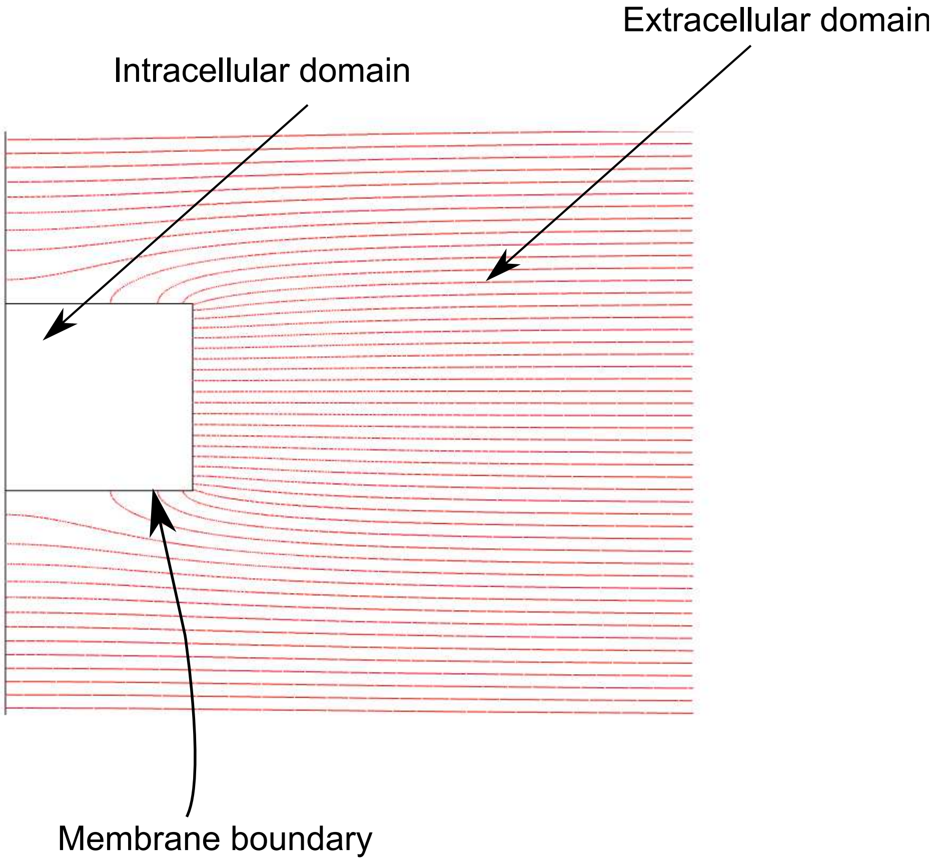

Figure 2.15: A potential contour plot from the finite-element solution for a compact cylindrical neuron in a uniform electric field. The compact cell distorts the applied uniform electric field causing radial currents to flow. This is an example of the neuron feeding-back to the extracellular electric field.

2.6 Physical reasoning behind the shape-dependent frequency response

The differences observed in our simulations in the effective membrane time constants between direct current injection and field preparations, and between different cylindrical shapes can be understood by considering how the membrane polarizes in these different situations in response to the changing electric field [70]. In the current injection case for a spherical cell, the charge spreads uniformly in the radial direction from the stimulating electrode causing the cell membrane to be uniformly charged and hence isopotential, with the current driven entirely through the membrane with the time constant $\tau_m = \frac{c_m}{g_L}$. In the case of field stimulation above, the membrane is non-uniformly charged, with the one end hyperpolarized while the other depolarized by the field (fig. 2.9a). Thus as the field orientation changes, only a redistribution of charge is required, which occurs through the extra and intracellular media acting as parallel conductances to the membrane conductance for the charge transfer. From Eq. 1.25, the effective conductance of the system increases to

$$g_L + \frac{1}{a\left(\frac{1}{2\sigma_e} + \frac{1}{\sigma_i}\right)} \tag{2.62}$$

providing a much smaller time constant. As we increase the cell size with a larger radius a, the distances and hence the resistances through the bulk media eventually become too large for the parallel charge transfer and the cell reverts to current injection behaviour, with the expression in Eq. 2.62 being reduced to g_L (and a much larger time constant). For physiological values of the bulk conductivities and membrane conductance (table 1.1), the parallel bulk media conductance becomes comparable with the membrane conductance for non-physiological values of a.

In the case of the cylindrical cell approximated by the cable equation, we see that the effective membrane time constant for electrotonically compact cells is given by Eq. 2.33, i.e. $\tau_{cab} = \frac{l^2}{\lambda^2}\tau_m = \frac{l^2 c_m}{\lambda^2 g_L} = \frac{2l^2 c_m}{a\sigma_i}$, where we have used the definitions

$\tau_m = \frac{c_m}{g_L}$ and $\lambda = \sqrt{\frac{a}{2r_L g_L}}$ from earlier to arrive at the last expression. If we now reformulate the last expression as $\frac{c_m}{g_{bulk}}$ we obtain the parallel bulk conductance as $g_{bulk} = \frac{a\sigma_i}{2l^2}$. As τ_{cab} is given for the electrotonically compact case, the effective conductance in play in τ_{cab} must be the dominant parallel bulk media conductance and hence the total effective conductance of the system is given by

$$g_L + \frac{a\sigma_i}{2l^2} \tag{2.63}$$

Thus as long as the cell is compact with a small $\frac{l}{a}$ ratio, the parallel bulk media conductance is high and dominant, and the system exhibits a small effective membrane time constant. With an increasing $\frac{l}{a}$ ratio however, the effective bulk media conductance decreases due to the increasing distances along cylinder length and a decreasing cross-sectional area through which charge redistribution takes place, and thus the effective membrane time constant increases with the cell reverting to current injection like behaviour.

Chapter 3

Extracellular point-source stimulation of neurons

The spatiotemporal profile of the neuronal membrane potential in a cell-field system, is determined not only by the shape of the cell, but also by the spatial profile of the applied electric field. In the above sections, we have only studied the effect of uniform extracellular fields that induce a linearly varying extracellular potential around the cell. In physiological situations however, the extracellular field is produced by distributed current sinks and sources [77] and thus is not uniform [59]. The typical electrophysiological experiment consists of application of extracellular current through small electrodes which, depending on the distance from the neuron, can produce a highly non-uniform field around it [57,78] (fig. 3.1). Furthermore, the fields applied using cylindrical electrodes with monopolar and multipolar activity in vivo during deep brain stimulation (DBS) therapy are also highly non-uniform [76].

Lee and Grill [78] investigated the effect of point-source stimulation on spherical cells by applying the boundary-value problem approach developed by Schwan for uniform electric fields [47]. Like in the uniform field case, they found the effective membrane time constant for the point-stimulated spherical cell to be much shorter than the membrane time constant, τ_m. Hentall [79, 80] has also derived a power series solution for point stimulation of finite cables with sealed ends. Anastassiou et al [72] again using the "extracellular cable" formalism studied in detail the effects of fields oscillating in time as well as in space on unbranched cables as well as on a morphologically realistic, reconstructed CA1 neuron and found the effect of the fields to persist for up to temporal frequencies of 200 Hz. It is interesting to note that the theoretical results in the study by Anastassiou et al [72] suggest smaller time constants for cable sections (apical dendrites) which are more aligned with the field with respect to those which have a more perpendicular orientation (basal dendrites), in apparent contrast to our findings in chapter 2. We suggest that this discrepancy is only apparent because of the varying electrotonic length constants λ of the different sections, with the apical dendrites consisting of thicker cables with respect to the basal dendrites. Thus if we were to simulate cable sections using our models, with the same field orientations and electrotonic length constants as in [72], we would obtain the same relationship as in [72], between the type of dendrite and the time constants.

We again argue that like in the case of uniform fields, the relationship between the frequency behaviour and the shape of the neuron has been neglected and as we will demonstrate below, some important effects have been missed. In this chapter we focus on the effects of oscillating electric fields on cylindrical neurons generated by extracellular point-sources. As before we utilize both the cable equation method (Eq. 2.7) and our FEM method (section 2.5.2) for investigating this problem.

3.1 Point-source stimulation of a sealed cable

According to electromagnetic theory, the electric field due to a point current source is spherically symmetric and attenuates with distance in the inverse squared fashion (fig. 3.1). The consequent electric potential is given by

$$V_e = \frac{I}{4\pi\sigma_e\sqrt{d^2 + (x-p)^2}} \tag{3.1}$$

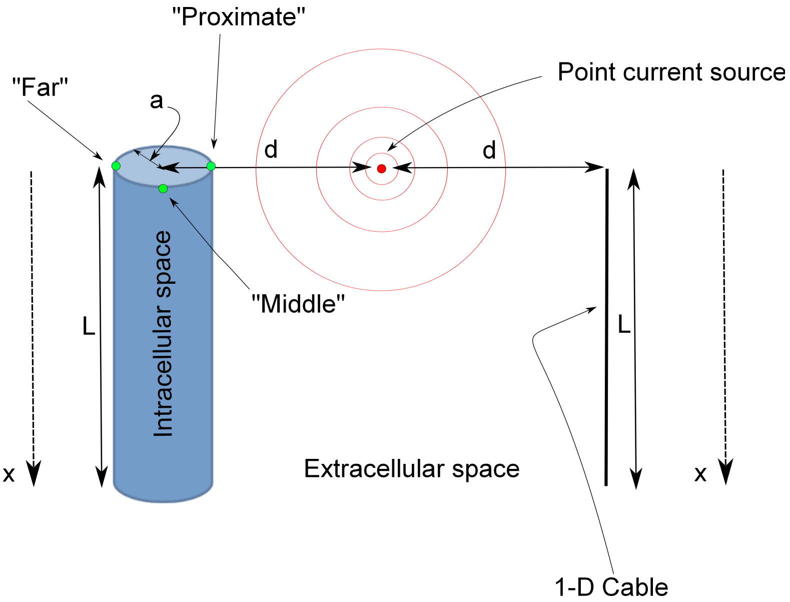

Figure 3.1: Point-source stimulation of cylindrical neurons (cable neuron (right), and three-dimensional finite-element neuron (left)). Due to the asymmetry imposed by the point-source current, a full three-dimensional model of the neuron has to be considered for the finite-element method. We consider three measurement points on the three-dimensional cylinder, “proximate”, “middle” and “far”.

where I is the magnitude of the applied extracellular current, d is the perpendicular distance of the point-source from the neuron, x (here ranging from 0 to L) is the distance along the coordinate axis parallel to the cable axis and p is the distance along the x-axis where the point-source is located (fig. 3.1). At steady-state and with a general form of the extracellular potential V_e, the extracellular cable equation (Eq. 2.7) becomes

$$\frac{d^2V_i}{dx^2} - \frac{V_i}{\lambda^2} = -\frac{V_e}{\lambda^2} \tag{3.2}$$

In order to solve the above equation (Eq. 3.2) with the point-source field (Eq. 3.1), we utilize the Green’s function approach (see section 2.5.2 of [90]). The Green’s function can be thought of as the solution of a linear equation (like Eq. 3.2) with a unit impulse (defined by the Dirac Delta function, δ) as its input. The linearity of the equation then allows for the construction of the solution for any input through the superposition of the Green’s functions. Lets assume that a Green’s function exists such that

$$V_i(x) = -\int_0^L dz G(x,z) \frac{V_e(z)}{\lambda^2} \tag{3.3}$$

where $V_i(x)$ is the general solution to Eq. 3.2, which obeys some boundary conditions and z is the integration variable. Combining Eq. 3.2 and Eq. 3.3 we obtain

$$\int_0^L dz \left(\tfrac{d^2G(x,z)}{dx^2} - \tfrac{G(x,z)}{\lambda^2}\right) V_e(z) = V_e(x) \tag{3.4}$$

$$\implies \qquad \tfrac{d^2G(x,z)}{dx^2} - \tfrac{G(x,z)}{\lambda^2} = \delta(x-z) \tag{3.5}$$

where we have used the well known property of the Dirac delta function, δ

$$\int_0^L dz \delta(x,z) V_e(z) = V_e(x) \tag{3.6}$$

to obtain Eq. 3.5. As stated earlier, the problem is thus converted to that of finding the appropriate Green's function, which can be thought of as a response of the system to a unit impulse at $x = z$.

Eq. 3.5 is homogenous at $x \neq z$, so we propose general solutions which satisfy this homogeneity

$$G(x,z) = A(z) \sinh \frac{x}{\lambda} + B(z) \cosh \frac{x}{\lambda} \qquad x < z \tag{3.7}$$

$$G(x,z) = C(z) \sinh \frac{x}{\lambda} + D(z) \cosh \frac{x}{\lambda} \qquad x > z \tag{3.8}$$

Two different ansatz are required because of the discontinuity at $x = z$, given by integrating Eq. 3.5

$$\int_{z-\epsilon}^{z+\epsilon} \left(\frac{d^2G(x,z)}{dx^2} - \frac{G(x,z)}{\lambda^2}\right) dx = 1 \qquad \epsilon \to 0 \tag{3.9}$$

$$\left[\frac{dG(x,z)}{dx}\right]_{z-\epsilon}^{z+\epsilon} - \int_{z-\epsilon}^{z+\epsilon} \frac{G(x,z)}{\lambda^2} dx = 1 \qquad \epsilon \to 0 \tag{3.10}$$

With $G(x,z)$ being continuous by assumption, according to Eq. 3.10 we must have a discontinuity in the first derivative

$$\left[\frac{dG(x,z)}{dx}\right]_{z-\epsilon}^{z+\epsilon} = 1 \qquad \epsilon \to 0 \tag{3.11}$$

The sealed-end, homogenous boundary condition on $V_i(x)$ at $x = 0$ is most simply satisfied by requiring

$$\frac{dG(0,z)}{dx} = 0 \qquad x < z \tag{3.12}$$

which in turn implies

$$\tfrac{A(z)}{\lambda}\cosh(0) + \tfrac{B(z)}{\lambda}\sinh(0) = 0 \tag{3.13}$$

$$\implies \qquad A(z) = 0 \tag{3.14}$$

Similarly at $x = L$

$$\frac{dG(L,z)}{dx} = 0 \qquad x > z \tag{3.15}$$

which implies

$$C(z)\cosh\left(\tfrac{L}{\lambda}\right) + D(z)\sinh\left(\tfrac{L}{\lambda}\right) = 0 \tag{3.16}$$

$$\implies \qquad C(z) = -D(z)\tanh\left(\tfrac{L}{\lambda}\right) \tag{3.17}$$

Thus our general Green's functions become

$$G(x,z) = B(z)\cosh\frac{x}{\lambda} \qquad x < z \tag{3.18}$$

$$G(x,z) = D(z)\left(\cosh\frac{x}{\lambda} - \left(\tanh\frac{L}{\lambda}\right)\left(\sinh\frac{x}{\lambda}\right)\right) \qquad x > z \tag{3.19}$$

Applying the continuity condition for $G(x, z)$ at $x = z$, we obtain

$$B(z) \cosh \tfrac{z}{\lambda} = D(z) \left(\cosh \tfrac{z}{\lambda} - \left(\tanh \tfrac{L}{\lambda}\right) \left(\sinh \tfrac{z}{\lambda}\right)\right) \tag{3.20}$$

or
$$D(z) = \tfrac{B(z)}{1 - \tanh \frac{L}{\lambda} \tanh \frac{z}{\lambda}} \tag{3.21}$$

Now applying the discontinuity condition in Eq. 3.11 we get

$$\begin{gathered} \tfrac{D(z)}{\lambda} \left(\sinh \tfrac{z}{\lambda} - \tanh \tfrac{L}{\lambda} \cosh \tfrac{z}{\lambda}\right) \qquad (3.22) \\ -\tfrac{B(z)}{\lambda} \sinh \tfrac{z}{\lambda} = 1 \end{gathered}$$

Combining Eqs. 3.21 and 3.22, we obtain

$$D(z) = -\lambda \tfrac{\cosh \frac{z}{\lambda}}{\tanh \frac{L}{\lambda}} \tag{3.23}$$

$$B(z) = \lambda \left(\sinh \tfrac{z}{\lambda} - \tfrac{\cosh \frac{z}{\lambda}}{\tanh \frac{L}{\lambda}}\right) \tag{3.24}$$

So we have the Green's function as

$$G(x, z) = \frac{-\lambda \cosh \frac{x}{\lambda}}{\sinh \frac{L}{\lambda}} \cosh \frac{(z - L)}{\lambda} \qquad x < z \tag{3.25}$$

$$G(x, z) = \frac{-\lambda \cosh \frac{z}{\lambda}}{\sinh \frac{L}{\lambda}} \cosh \frac{(x - L)}{\lambda} \qquad x > z \tag{3.26}$$

Substituting into Eq. 3.3 we obtain the solution as

$$\begin{aligned} V_i(x) \quad = \quad & \frac{1}{\lambda \sinh \frac{L}{\lambda}} \left(\cosh \frac{(x - L)}{\lambda} \int_0^x dz \cosh \frac{z}{\lambda} V_e(z) \right. \qquad (3.27) \\ & \left. + \cosh \frac{x}{\lambda} \int_x^L dz \cosh \frac{(z - L)}{\lambda} V_e(z)\right) \end{aligned}$$

The benefit of the Green's function approach is that any form of V_e can now be substituted into Eq. 3.27 to obtain the appropriate analytical solution with sealed-end boundary conditions. The corresponding frequency response to an oscillating point current source is obtained as before by substituting λ_c for λ (Eq. 2.29).

The analogous FEM model is implemented in a similar fashion as section 2.5.2 but this time requiring the far outer extracellular boundaries to be grounded to zero and adding a "point" primitive geometrical feature to act as a current source. The non-uniform point-source field breaks the axial symmetry of the models studied above and requires the construction of a full three-dimensional model of a cylindrical neuron (or neurite) (fig. 3.1). The "frequency domain" study type is again used with transmembrane current density $J = (g_L + i\omega c_m)(V_i - V_e)$ to investigate the frequency response of the field-cell system.

3.1.1 Steady-state point-source stimulation of finite cylinders

For an non-oscillating extracellular point-source (Eq. 3.1) located at $x = p = 0$, the extracellular potential is given by

$$V_e = \frac{I}{4\pi\sigma_e\sqrt{d^2+x^2}} \tag{3.28}$$

Substituting Eq. 3.28 into Eq. 3.27 gives the steady-state solution for the intracellular potential of a cable stimulated by a point current source at one of its ends (located a distance d away from the cable end)

$$\begin{aligned} V_i(x) \quad = \quad & \frac{I}{4\pi\sigma_e\lambda\sinh\frac{L}{\lambda}}\left(\cosh\frac{(x-L)}{\lambda}\int_0^x dz\cosh\frac{z}{\lambda\sqrt{d^2+z^2}}\right. \\ & \left. +\cosh\frac{x}{\lambda}\int_x^L dz\cosh\frac{(z-L)}{\lambda\sqrt{d^2+z^2}}\right) \end{aligned} \tag{3.29}$$

The steady-state solution for the membrane potential evaluated at $x = 0$ is given by

$$V_m(0) = V_i(0) - V_e(0) = \tfrac{I}{4\pi\sigma_e d}\left(\tfrac{1}{\lambda\sinh\frac{L}{\lambda}}\textstyle\int_0^L dz\tfrac{\cosh\left(\frac{L-z}{\lambda}\right)}{\sqrt{1+\frac{z^2}{d^2}}} - 1\right) \tag{3.30}$$

$$V_m(0) = \tfrac{I}{4\pi\sigma_e d}\left(\tfrac{1}{\lambda\sinh\frac{L}{\lambda}}\left(\lambda\sinh\tfrac{L}{\lambda} - \textstyle\int_0^L dz\tfrac{\sinh\left(\frac{L-z}{\lambda}\right)}{qd^2}\tfrac{z}{\left(1+\frac{z^2}{d^2}\right)^{\frac{3}{2}}}\right) - 1\right) \tag{3.31}$$

$$V_m(0) = \tfrac{I}{4\pi\sigma_e d^3\sinh\frac{L}{\lambda}}\textstyle\int_0^L dz\tfrac{z\sinh\left(\frac{L-z}{\lambda}\right)}{\left(1+\frac{z^2}{d^2}\right)^{\frac{3}{2}}} \tag{3.32}$$

where we have used integration by parts to obtain Eq. 3.32. Similar to the uniform field case, the extracellular point stimulation induces biphasic polarization of the cable, hyperpolarizing the end closest to the stimulation point and depolarizing the other end, with the most extreme polarization occurring at the ends (fig. 3.2). In contrast with the uniform case, the polarization induced by the point-source is asymmetric with the neutral point located nearer the stimulation end of the cable (fig. 3.2). As the cable length, L decreases and the distance of the source from the proximate cable end, d increases, the membrane potential decreases and the polarization becomes more symmetric (fig. 3.2). This is because a small $\frac{L}{d}$ ratio results in the whole cable experiencing a relatively uniform and radial field, with the extracellular potential given by

$$V_e = \frac{I}{4\pi\sigma_e d} \tag{3.33}$$

Comparing the cable results with the FEM simulations, we take three measurement points to consider in the three-dimensional FEM model of the neuronal cylinder for every point on the one-dimensional cable, i.e. the “proximate” point closest to the stimulation point, the “far” point furthest from the stimulation point and the “middle” point in between the previous two (fig. 3.1). The spatial profile for the middle edge of the FEM model matches well with the cable profile for both electrotonically long (fig. 3.3) and short (fig. 3.4a) neurons.

In the case of long neurons, we see that the spatial profiles for the proximate and far edges of the FEM model, deviate from the middle edge and cable profiles, close to the stimulation end and converge further away (fig. 3.3). The greater deviation at and near the stimulation end ($x = 0$) occurs because the field has a greater radial component in this region and is able to differentially polarize the neuron across its radial extent. Further away from the stimulation point, the field becomes more axial and polarizes uniformly across the circumference of the neuron like in the uniform field situation studied earlier in this thesis. In the case of compact neurons, the spatial profiles for the proximate and far edges of the FEM model,

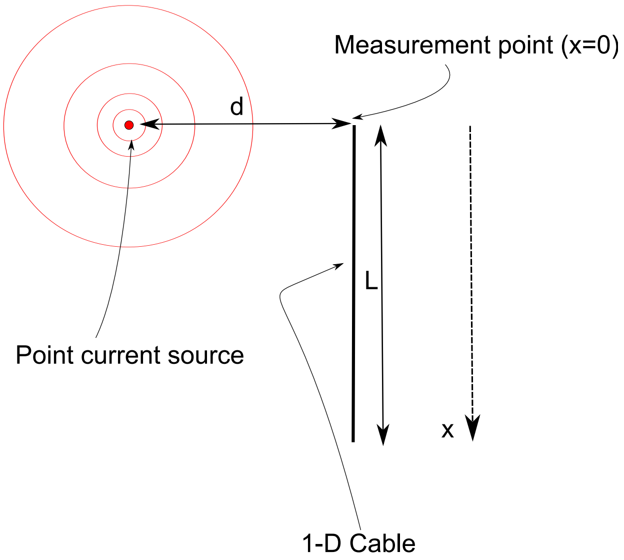

(a)

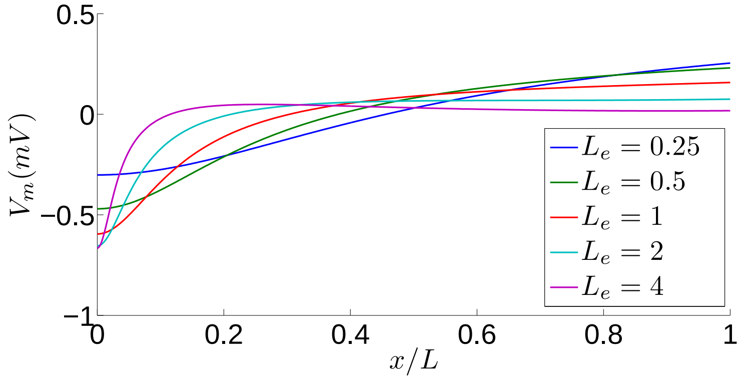

(b) $d = 0.1\lambda$

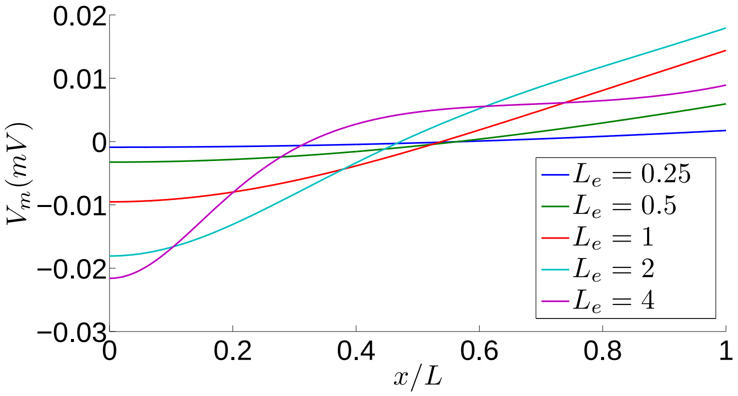

(c) $d = \lambda$

Figure 3.2: Steady-state membrane potential profiles of cable neurons of various electrotonic lengths, under point-source stimulation, with the source aligned horizontally with one of the cable-ends (fig. 3.1). V_m is plotted against x normalized to the cable length L. Two different values of the source-to-neuron distance are considered, with $I = 100$ nA. a) Illustration showing the positioning of the cable neuron with respect to the point source and the point of measurement. b) Plots for $d = 0.1\lambda$ and c) $d = \lambda$. A biphasic and asymmetric polarization is observed, with the neutral point located nearer to the stimulation end of the cable. The membrane potential profile becomes more symmetric with smaller $\frac{L}{d}$ ratios. The neurons considered have sealed ends. The parameters used to produce these figures are as given in table 1.1, with the cable radius $a = 2$ μm and $\lambda = 447.2$ μm.

deviate from the middle edge and the cable profile, along the whole length of the neuron (fig. 3.4a). The relative difference occurring for compact neurons is very significant (~95% increase in V_m) because the entirety of the the neuron experiences a largely radial field, the effects of which the cable model cannot account for. Without the uniform polarization across the neuron circumference due the axial components, the polarization due to the radial field becomes very significant. The radially varying V_m due to the radial field can be seen across the top of the three-dimensional compact cylindrical neuron (fig. 3.4b). Furthermore, due to the entirely radial extracellular field for the compact neuron, the V_m is constant over the length of the neuron, taking zero value for the cable and middle FEM edges and a finite value for the proximate and far FEM edges.

3.1.2 Sinusoidally oscillating point-source stimulation of finite cylinders - membrane potential response at the stimulation end

Imposing a sinusoidally oscillating extracellular point-source located at $x = p = 0$, the extracellular potential is given by

$$V_e = \frac{Ie^{i\omega t}}{4\pi\sigma_e\sqrt{d^2 + x^2}} \tag{3.34}$$

As in the uniform case, applying the mapping $\lambda \rightarrow \lambda_c = \frac{\lambda}{\sqrt{1+i\omega\tau}}$ for Eq. 3.32 yields the oscillatory solutions for the membrane potential of the cable neuron. As in the case of uniform field stimulation (fig. 2.4), we again observe the electrotonically shorter neurons being responsive to higher-frequency point-field stimulation (fig. 3.5) due to the high values of extra and intracellular conductances contributing to a high effective membrane conductance (thus leading to very small values of the effective membrane time constants). For example, the response of the neurons with electrotonic lengths from $L_e = 1$ down to $L_e = 0.25$ extends from ~100-1000 Hz (fig. 3.5) with extracellular point stimulation. The point stimulation used in these models corresponds to the unipolar extracellular stimulation of the compact somata

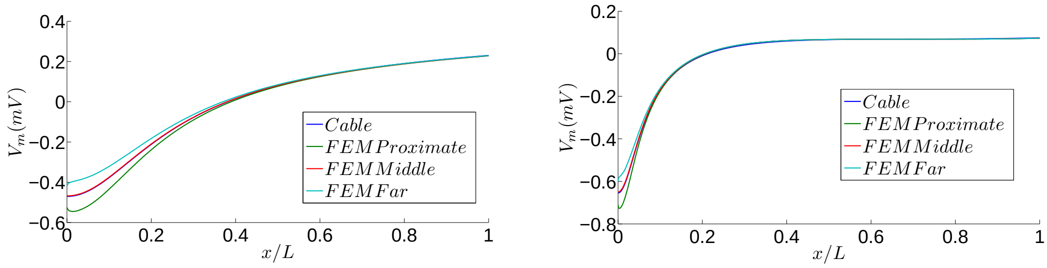

(a) $L_e = 0.5$ and $d = 0.1\lambda$ (b) $L_e = 2$ and $d = 0.1\lambda$

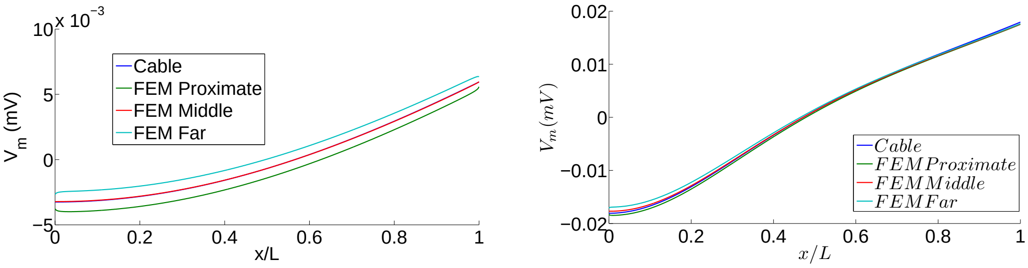

(c) $L_e = 0.5$ and $d = \lambda$ (d) $L_e = 2$ and $d = \lambda$

Figure 3.3: Comparison between the FEM and cable methods for the steady-state membrane potential profiles of neurons under point-source stimulation ($I = 100$ nA) with a) $L_e = 0.5$ and $d = 0.1\lambda$ b) $L_e = 2$ and $d = 0.1\lambda$ c) $L_e = 0.5$ and $d = \lambda$ and $L_e = 2$ and $d = \lambda$. The source is aligned horizontally with one of the cable-ends (fig. 3.1). V_m is plotted against x normalized to the cable length L. The cable profiles match well with the “middle” FEM profiles. The difference between the cable and the “proximate” / “far” profiles arises due to the radial orientation of the field at and near $x = 0$. The neurons considered have sealed ends. The parameters used to produce these figures are as given in table 1.1, with the cable radius $a = 2$ μm and $\lambda = 447.2$ μm.

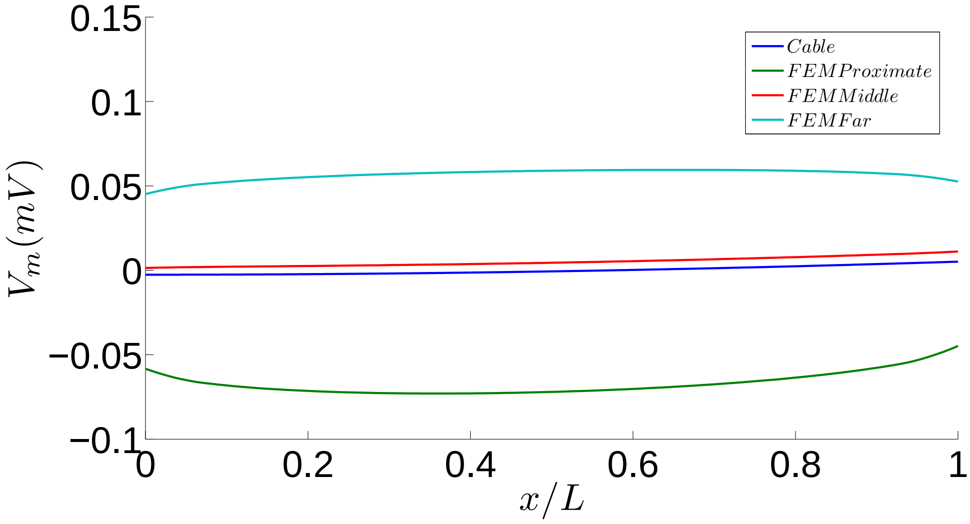

(a) 10×10 μm cell $d = 0.1\lambda$ (axial variation of V_m)

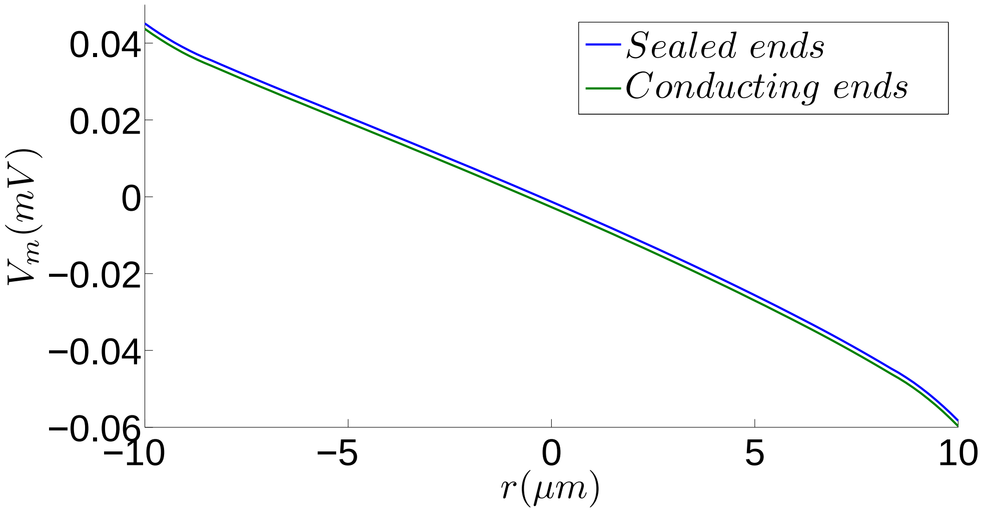

(b) 10×10 μm cell $d = 0.1\lambda$ (radial variation of V_m)

Figure 3.4: Comparison between the FEM and cable methods for the steady-state membrane potential profiles of a compact 10×10 μm neuron under point-source stimulation ($I = 100$ nA). The source is aligned horizontally with one of the cable-ends (fig. 3.1). a) The axial profile of V_m differs greatly between the “proximate” and “far” FEM results, and the cable results (∼95% increase in V_m for the FEM model). V_m is plotted against x normalized to the cable length L. The neuron considered has sealed ends. b) Radial variation of V_m across the top of the FEM three-dimensional cylindrical neuron (taking a line from the “proximate” to the “far” point), with conducting and sealed ends. The radial field due to the point-source induces a radially varying membrane potential across the top of the cylinder. The parameters used to produce these figures are as given in table 1.1, with the cable radius $a = 10$ μm and $\lambda = 1000$ μm. An $a \times l$ neuron corresponds to a cell with radius a and half-length l.

of cortical neurons performed by Anastassiou et al [57] and thus could help explain the high-frequency response (up to 100 Hz) observed by them. Previous results have shown that due to the high concentration of current density at the electrode tip, the point-source is an appropriate model for the unipolar microelectrode for electrode-cell distances of $d > 10\ \mu$m [81].

It should also be observed that, just like in the uniform field case (fig. 2.4a), under high-frequency point-source stimulation, no frequency selectivity is observed for the cable end proximate to the "electrode". Thus although the response of the compact neuron attenuates at higher frequencies than for the elongated neuron, the membrane potential at its "proximate" end does not exceed that of the elongated neuron significantly through the whole frequency range (fig. 3.5).

Comparing the membrane potential frequency response of the finite cable under uniform and point stimulation, we observe no difference in the drop-off frequency for the $L_e = 1$ and the very compact $10 \times 10\ \mu$m neuron (fig. 3.6). Thus the inhomogeneity of the point-source extracellular field (centered alongside a cable end) does not influence the effective time constant for the frequency drop-off point, which remains identical to the uniform case.

Comparing the FEM model with the cable model for the frequency behaviour of the cylindrical neuron (at the stimulation end), we see that as in the steady-state case, the "middle" point (fig. 3.1) of the three-dimensional FEM model matches well with the one-dimensional cable model (fig. 3.7). The "proximate" and "far" ends of the FEM model differ significantly from the cable results for compact neurons (fig. 3.8) due to the radial profile of the extracellular field in the FEM case. For electrotonically longer neurons, a further high-frequency plateau is observed for the FEM model neurons, which is absent from the cable results (fig. 3.7).

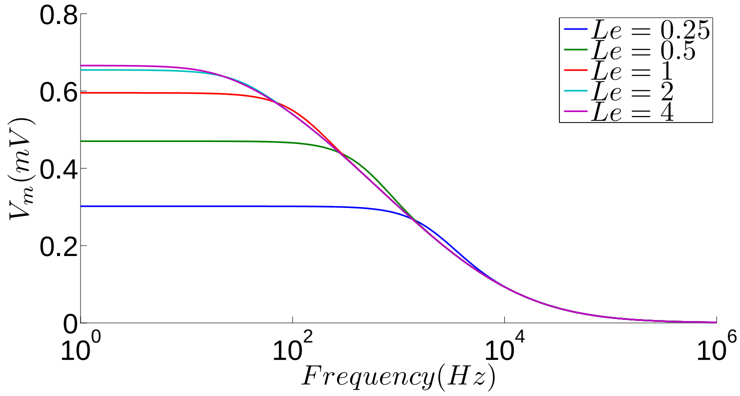

(a) $d = 0.1\lambda$

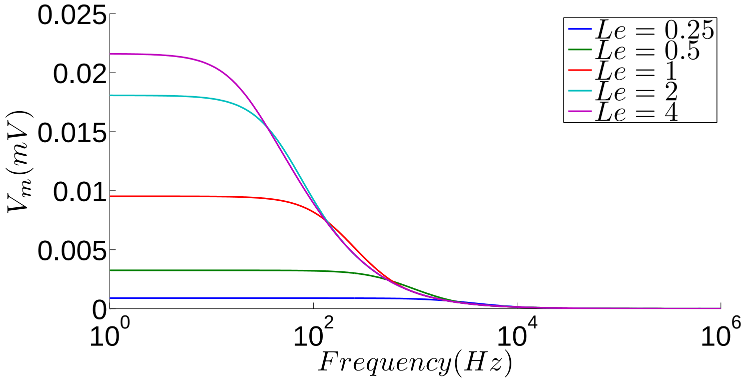

(b) $d = \lambda$

Figure 3.5: Electrotonically compact cable neurons remain responsive to high-frequency electric field stimulation from a point-source ($I = 100$ nA and V_m is measured at the cable end proximate to the point-source $x = 0$). Frequency response of neurons of various electrotonic lengths (box top right) to point-source electric field stimulation, with V_m measured at the cable end closest to the source. Like in the uniform field case (fig. 2.4), more compact neurons exhibit a higher drop-off frequency indicating a shorter time constant for membrane polarization. The frequency response of all the neurons converge at high frequencies, with the response of the shorter neurons never significantly exceeding that of the longer ones. Two different values of d: a) 0.1λ and b) λ are used. The neurons considered have sealed ends. The parameters used to produce these figures are as given in table 1.1, with the cable radius $a = 2$ μm and $\lambda = 447.2$ μm.

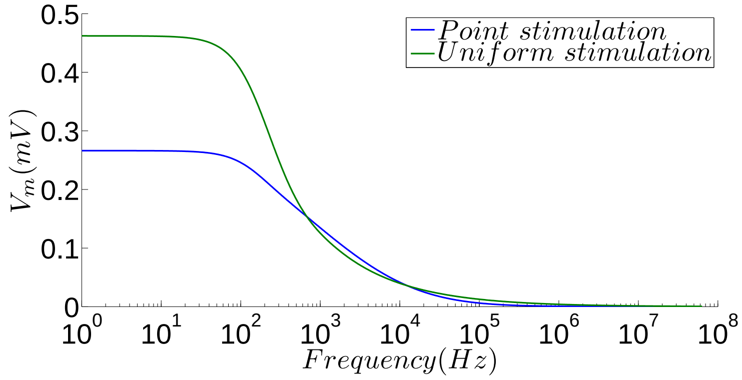

(a) $L_e = 1$

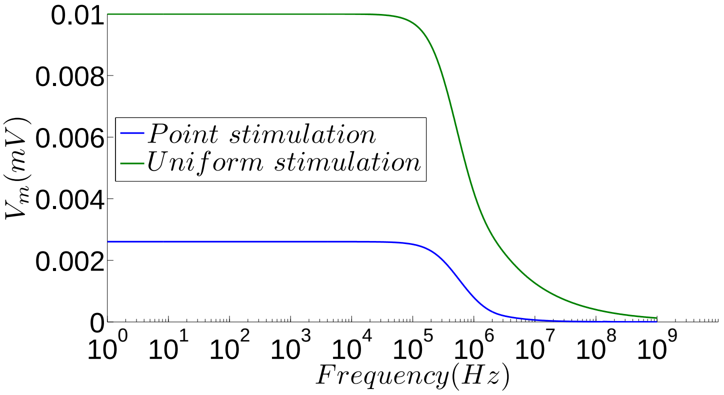

(b) 10×10 μm cell

Figure 3.6: Comparison between cable neurons under uniform and point-source field stimulation with $d = 0.1\lambda$ ($I = 100$ nA and V_m is measured at the cable end, $x = 0$). Neurons with two differing sizes: a) $L_e = 1$ (with $a = 2$ μm and $\lambda = 447.2$ μm) and b) 10×10 μm (with $a = 10$ μm and $\lambda = 1000$ μm) are considered. Both point and uniform stimulation produce the same frequency drop-offs. The neurons considered have sealed ends. The parameters used to produce these figures are as given in table 1.1. An $a \times l$ neuron corresponds to a cell with radius a and half-length l.

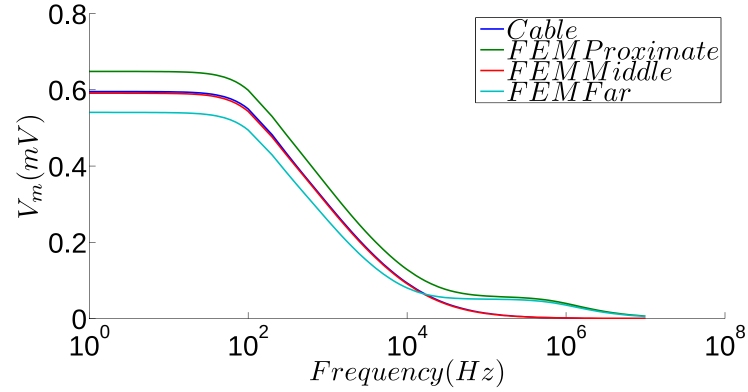

(a) $L_e = 1$ and $d = 0.1\lambda$

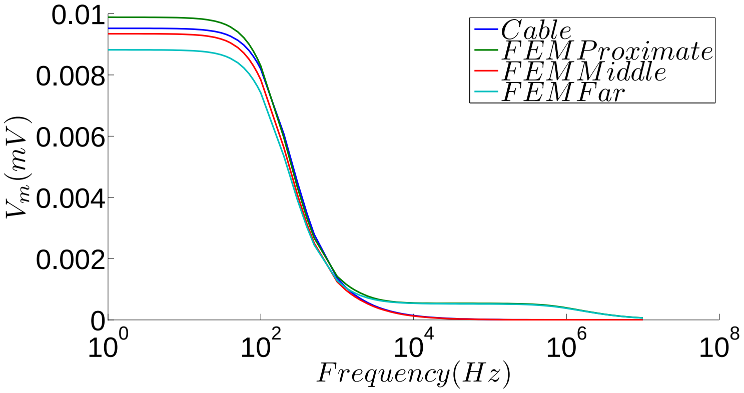

(b) $L_e = 1$ and $d = \lambda$

Figure 3.7: Comparison between finite-element and cable methods in ascertaining the frequency response for cylindrical neurons of electrotonic length $L_e = 1$, in an oscillating point-source electric field ($I = 100$ nA and V_m is measured at the cable end $x = 0$). The "middle" point for the FEM model matches well with the cable model for both a) $d = 0.1\lambda$ and b) $d = \lambda$. An additional high-frequency plateau is observed for the FEM models. The measurement is performed at the cable end proximate to the source. The neurons considered have sealed ends. The parameters used to produce these figures are as given in table 1.1, with the cable radius $a = 2$ μm and $\lambda = 447.2$ μm.

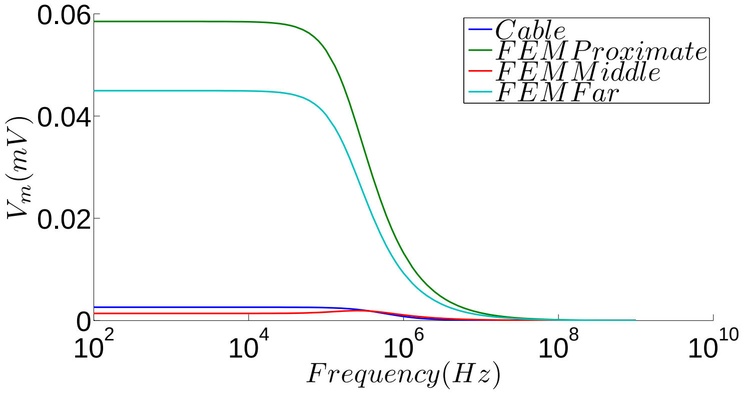

(a) 10×10 μm neuron with $d = 0.1\lambda$

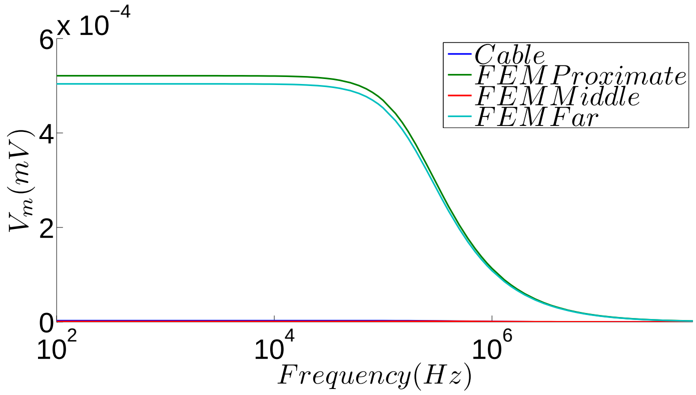

(b) 10×10 μm neuron with $d = \lambda$

Figure 3.8: Comparison between finite-element and and cable methods in ascertaining the frequency response for a compact cylindrical neuron of size 10×10 μm , in an oscillating point-source electric field ($I = 100$ nA and the measurement is performed at the cable end proximate to the source $x = 0$). The FEM results for the "proximate" and "far" points differ greatly from the cable model for both a) $d = 0.1\lambda$ and b) $d = \lambda$. The difference is caused by the radial profile of the extracellular field for small $\frac{L}{d}$ ratios. The neurons considered have sealed ends. The parameters used to produce these figures are as given in table 1.1, with the cable radius $a = 10$ μm and $\lambda = 1000$ μm. An $a \times l$ neuron corresponds to a cell with radius a and half-length l.

3.1.3 Sinusoidally oscillating point-source stimulation of finite cylinders - membrane potential response away from the stimulation end

Measuring the oscillating point-source extracellular field response of the cylindrical cable away from the stimulation end ($x = 0.25L$, $x = 0.5L$, $x = 0.75L$ and $x = L$) yields some interesting observations which differ qualitatively from the uniform field response. In the first instance, similar to the uniform field stimulation case, we see a recovery of frequency selectivity when we plot the frequency profile of the cable points away from the stimulation end (figs. 3.9, 3.10, 3.11 and 3.12). Thus for "off-end" observation, we see the membrane potential response of the electrotonically compact neurons exceeding that of the extended neurons at high frequencies. For example, with $x = 0.5L$ and $d = 0.1\lambda$, we see that the response of the $L_e = 4$ cable is diminished by about 100 Hz, whereas the $L_e = 0.25$ cable's response remains unattenuated up to about 1×10^4 Hz, a difference of two orders of magnitude. As in the uniform case, this high-frequency selectivity occurs due to the spatial distribution of the membrane potential over the cable. In the case with $x = 0.5L$ and $d = 0.1\lambda$, we see that the highly asymmetric polarization profile of the $L_e = 4$ cable (fig. 3.2) ensures a similar level of polarization as to the $L_e = 0.25$ cable at low frequencies, the lower frequency drop off point for the longer cable then in turn ensuring that its response drops below that of the compact cable at high frequencies. This pattern of frequency selectivity is also seen for all the other cable positions (apart from the end proximate to the point-source) at which the membrane potential is plotted (figs. 3.9, 3.10, 3.11 and 3.12).

The above observations for neuronal time constants and high-frequency selectivity correlate with those for uniform field stimulation of finite cylinders in chapter 2 and thus validate the conclusions of the previous chapter for the case of the more realistic and experimentally relevant point-source field stimulation.

Apart from the frequency selectivity, another interesting behaviour is ob-

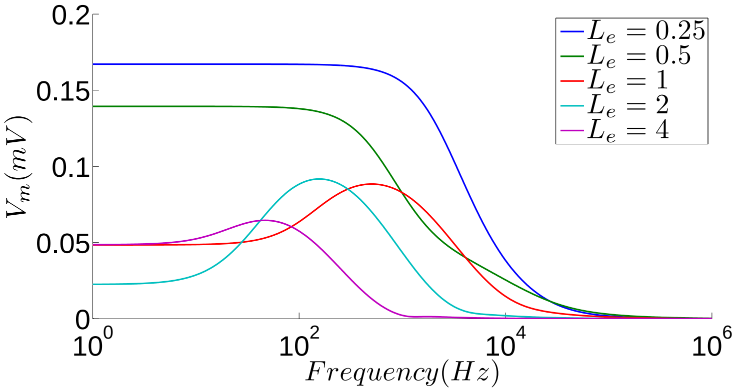

(a) $d = 0.1\lambda$

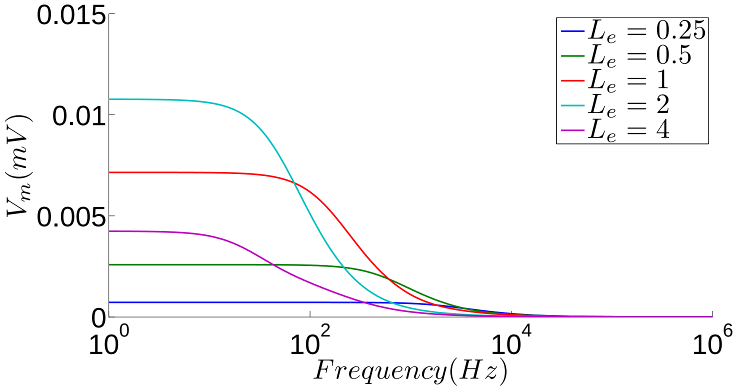

(b) $d = \lambda$

Figure 3.9: The "passive resonance" is observed for off-end measurement of cable neurons under point stimulation (with V_m measured at $x = \frac{L}{4}$). Frequency response of cable neurons of various electrotonic lengths (box top right) with a) $d = 0.1\lambda$ and b) $d = \lambda$. Frequency selectivity is observed with differing high-frequency asymptotes and the high-frequency response of the compact neurons exceeds that of the elongated ones. Additionally strong and broad resonances are observed for L_e =1, 2 and 4 in the $d = 0.1\lambda$ case. The neurons considered have sealed ends and the parameters used to produce these figures are as given in table 1.1, with the cable radius $a = 2$ μm and $\lambda = 447.2$ μm.

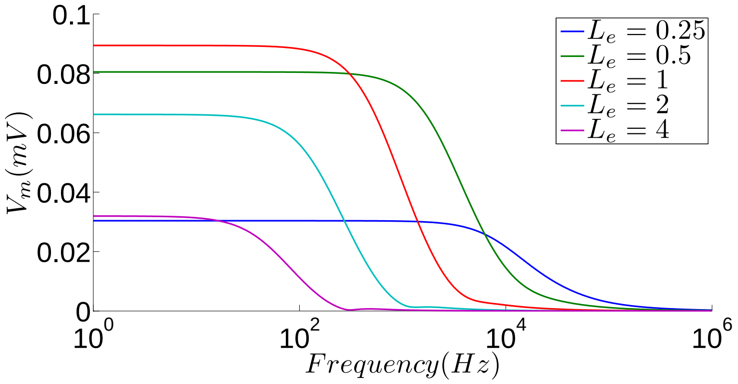

(a) $d = 0.1\lambda$

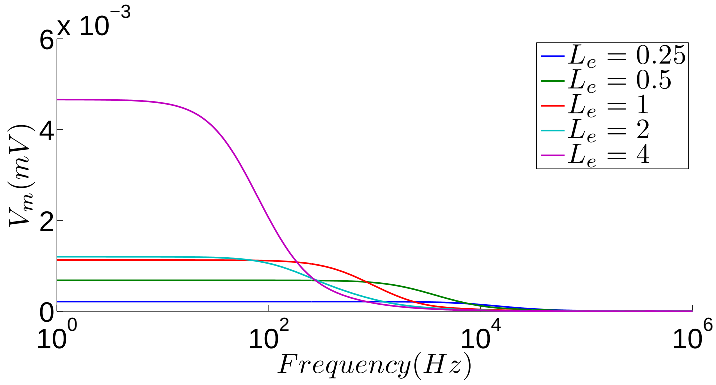

(b) $d = \lambda$

Figure 3.10: Frequency response of cable neurons (of various electrotonic lengths (box top right)) under point stimulation, with V_m measured at the center $x = \frac{L}{2}$, with a) $d = 0.1\lambda$ and b) $d = \lambda$. Frequency selectivity is observed with differing high-frequency asymptotes and the high-frequency response of the compact neurons exceeds that of the elongated ones. No resonance is observed. The neurons considered have sealed ends and the parameters used to produce these figures are as given in table 1.1, with the cable radius $a = 2$ μm and $\lambda = 447.2$ μm.

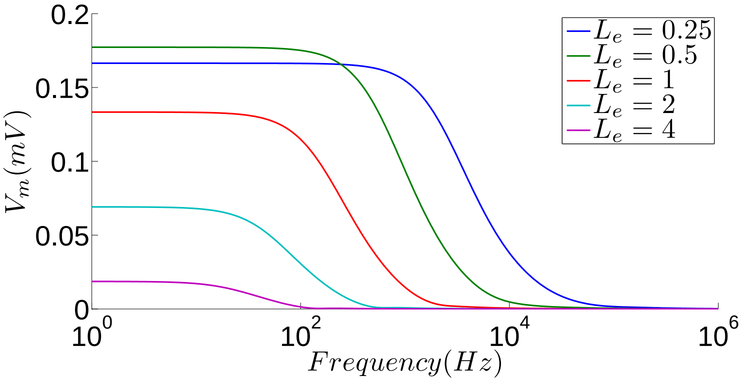

(a) $d = 0.1\lambda$

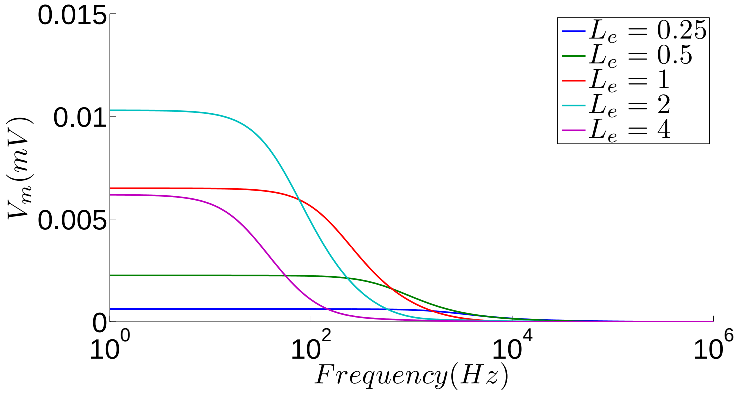

(b) $d = \lambda$

Figure 3.11: Frequency response of cable neurons of various electrotonic lengths (box top right) under point stimulation, with V_m measured at $x = \frac{3L}{4}$, with a) $d = 0.1\lambda$ and b) $d = \lambda$. Frequency selectivity is observed with differing high-frequency asymptotes and the high-frequency response of the compact neurons exceeds that of the elongated ones. No resonance is observed. The neurons considered have sealed ends and the parameters used to produce these figures are as given in table 1.1, with the cable radius $a = 2$ μm and $\lambda = 447.2$ μm.

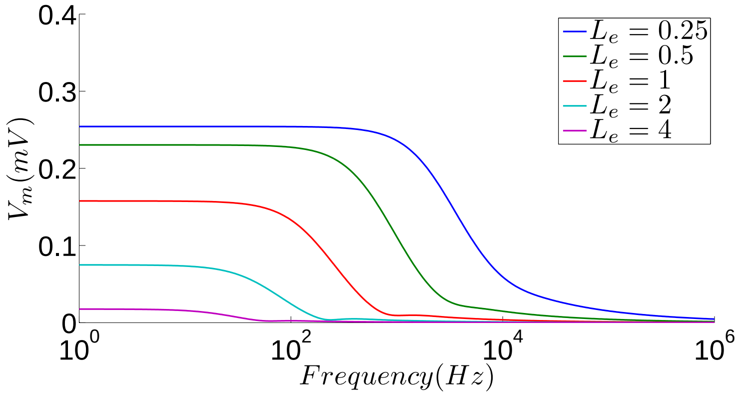

(a) $d = 0.1\lambda$

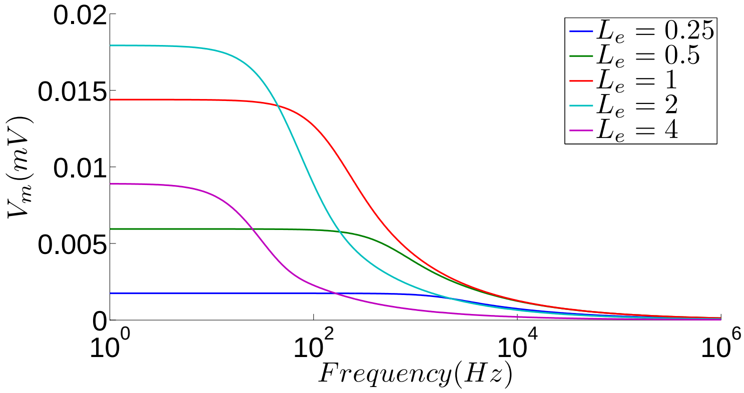

(b) $d = \lambda$

Figure 3.12: Frequency response of cable neurons of various electrotonic lengths (box top right) under point stimulation, with V_m measured at $x = L$, with a) $d = 0.1\lambda$ and b) $d = \lambda$. Frequency selectivity is observed with differing high-frequency asymptotes and the high-frequency response of the compact neurons exceeds that of the elongated ones. No resonance is observed. The neurons considered have sealed ends and the parameters used to produce these figures are as given in table 1.1, with the cable radius $a = 2$ μm and $\lambda = 447.2$ μm.

served for $x = 0.25L$, which is absent in the uniform field case, namely the strong resonances for $L_e = 1$, 2 and 4, with the electrode-cell distance of $d = 0.1\lambda$ (fig. 3.9a). These resonances occur near the drop-off frequencies for the respective cables and do not occur for the shorter cables. Furthermore, the resonances do not occur for larger electrode-cell distances (compare figs. 3.9a and 3.9b) and are spatially localized, not occurring for the other measurement points ($x = 0.5L$, $x = 0.75L$ and $x = L$). Figure 3.13 shows the evolution of the localized resonance through the length of the cable for the $L_e = 1$ neuron. The occurrence of the point stimulation resonance for the cell-field systems with spatially elongated cells and small electrode-cell distances (i.e. large $\frac{L}{d}$ ratios) lead us to conclude that the resonance occurs due to the inhomogeneity of the extracellular field as experienced by the entirety of the cable neuron. This is because small $\frac{L}{d}$ ratios imply an extracellular field at the cell which is radial and uniform (Eq. 3.33). Furthermore, the occurrence of the resonance is also related to the asymmetric polarization of the neuron as is demonstrated by its absence for electrodes positioned at the center of the cable with $p = 0.5L$ (figs. 3.15a and 3.15b) and its occurrence for $p = 0.25$ (fig. 3.15c).

Arising from the inhomogeneity of the imposed field, being dependent on the cell geometry and the electrode position and distance from the cell, this point-source resonance offers an alternative mechanism for frequency preference to subthreshold voltage-gated channels [60,61] and could play an important role in physiological and artificial field interactions. To our knowledge, this point-source resonance has not been reported in the theoretical or modeling literature to date and its experimental verification would be of interest. Experimental studies would require either extracellular recording electrodes to be positioned very close to individual dendrites or the recording electrodes to be patch-clamped on to sections of the dendritic tree, with an extracellular stimulus electrode creating the non-uniform electric field. Due to the small neurite diameters involved, dendritic patch-clamping is difficult and not many groups perform it, but improvements in the technique make it a possibility

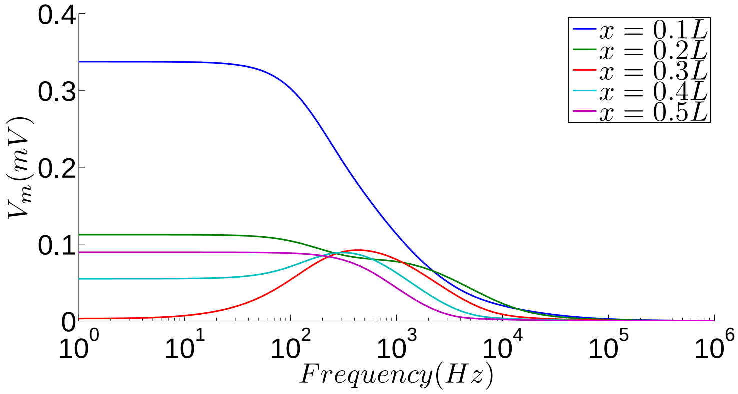

Figure 3.13: Development of the localized resonance through the length of the cable neuron from $x = 0.1L$ to $x = 0.5L$. The neuron under consideration is of size $L_e = 1$ and has sealed ends. The parameters used to produce these figures are as given in table 1.1, with the cable radius $a = 2$ μm and $\lambda = 447.2$ μm.

even for distal dendrites and with multiple recording electrodes [91].

The occurrence of the point-source resonance in the cable model is verified by our FEM model, which reproduces the resonance for all the three (proximate, middle and far) points on the three-dimensional cylinder (fig. 3.14). It should further be noted that resonance in neuronal cables with imposed extracellular fields has been reported by Monai et al, for asymmetric boundary conditions with a conductance shunt at one end [82], and could share the same mechanism as the point-source resonance reported above. The results relating to the point-source resonance in this chapter, could mean that electrotonically long neurons (and their passive dendrites) in the central nervous system may show a wide range of frequency preferences, depending on their particular geometry and the extracellular field environment.

3.1.4 Conducting-end cables

The point-source derivations in the previous section have been performed for sealed-end cables, we now derive the result for conducting-end cables using the Green's function methodology. For the sealed-end case above, the equation solved for a neuronal cable with an imposed field is given by Eq. 3.2 along with zero current boundary conditions at the ends. In the case of the conducting-end cable solution,

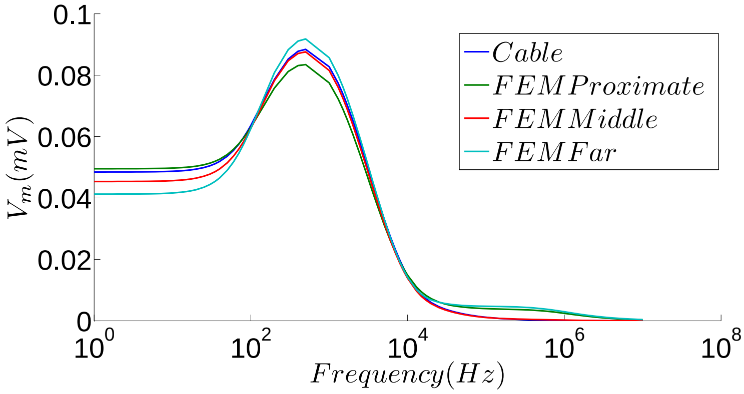

Figure 3.14: "Passive resonance" is observed for the three-dimensional FEM models as well as for the cable models (measurement performed at $x = 0.25L$ with horizontal electrode-neuron distance $d = 0.1\lambda$). The neuron under consideration is of size $L_e = 1$. The high-frequency plateau for the FEM case is observed as in the cases where the measurements are performed at $x = l$ above (fig. 3.7). The neuron has sealed ends and the parameters used to produce these figures are as given in table 1.1, with the cable radius $a = 2\ \mu$m and $\lambda = 447.2\ \mu$m.

$U_i(x)$, the bulk equation Eq. 3.2 remains the same

$$\frac{d^2U_i}{dx^2} - \frac{U_i}{\lambda^2} = -\frac{V_e}{\lambda^2} \tag{3.35}$$

but instead of the sealed-end boundary conditions we have

$$-\sigma_i \frac{\partial U_i(0)}{\partial x} = g_m(U_i(0) - U_e(0)) \tag{3.36}$$

$$-\sigma_i \frac{\partial U_i(L)}{\partial x} = g_m(U_i(L) - U_e(L)) \tag{3.37}$$

where

$$U_i(x) = V_i(x) + \phi(x) \tag{3.38}$$

and ϕ is the perturbation in the original sealed-end solution introduced by the change of boundary conditions. Substituting for U_i in Eq. 3.35 using Eq. 3.38, we obtain

$$\frac{d^2V_i}{dx^2} - \frac{V_i}{\lambda^2} + \frac{V_e}{\lambda^2} + \frac{d^2\phi}{dx^2} - \frac{\phi}{\lambda^2} = 0 \tag{3.39}$$

$$\text{or} \qquad \frac{d^2\phi}{dx^2} - \frac{\phi}{\lambda^2} = 0 \tag{3.40}$$

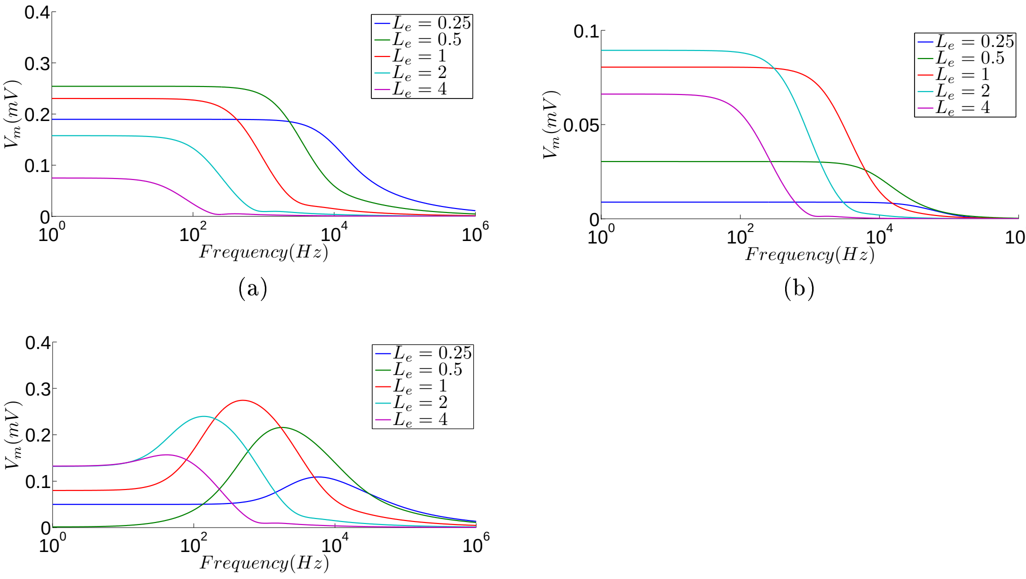

(a)

(b)

(c)

Figure 3.15: The “passive resonance” is observed for off-end point stimulation of cable neurons. Frequency response of cable neurons of various electrotonic lengths (box top right). The horizontal electrode-cell distance is $d = 0.1\lambda$ a) Point-source is placed next to the vertical center of the neuron and the measurement is performed at $x = 0$. No resonance is observed. b) Point-source is placed next to the vertical center of the neuron and the measurement is performed at $x = 0.25L$. No resonance is observed. c) Point-source is placed a quarter of the way up the length of the neuron $(x = \frac{L}{4})$ and the measurement is performed at $x = 0$. Strong and broad resonances are observed. The neurons considered have sealed ends and the parameters used to produce these figures are as given in table 1.1, with the cable radius $a = 2\ \mu$m and $\lambda = 447.2\ \mu$m.

which has the solution form

$$\phi = A \sinh \frac{x}{\lambda} + B \cosh \frac{x}{\lambda} \tag{3.41}$$

Thus we only need find the constants A and B, by substituting Eq. 3.38 into the boundary conditions Eqs. 3.36 and 3.37 to give

$$\begin{aligned} \tfrac{\partial \phi(0)}{\partial x} &= -\tfrac{g_m}{\sigma_i}(V_i(0) + \phi(0) - V_e(0)) \qquad (3.42) \\ \tfrac{\partial \phi(L)}{\partial x} &= -\tfrac{g_m}{\sigma_i}(V_i(L) + \phi(L) - V_e(L)) \qquad (3.43) \end{aligned}$$

which in turn give the unknown constants as

$$\begin{aligned} A &= -g_m \left(\tfrac{(-2g_m \cosh(qL) + q\sigma_i \sinh(qL))V_m(0) + g_m V_m(0)\cosh(qL) - g_m V_m(L)}{-2q\sigma_i g_m \cosh(qL) + q^2\sigma_i^2 \sinh(qL) + g_m^2 \sinh(qL)} \right) \qquad (3.44) \\ B &= \tfrac{q\sigma_i g_m \cosh(qL) V_m(0) - q\sigma_i g_m V_m(L) - g_m^2 V_m(0)\sinh(qL)}{-2q\sigma_i g_m \cosh(qL) + q^2\sigma_i^2 \sinh(qL) + g_m^2 \sinh(qL)} \qquad (3.45) \end{aligned}$$

which for a full solution are substituted into

$$U_i(x) = V_i(x) + A \sinh(qx) + B \cosh(qx) \tag{3.46}$$

along with the sealed-end cable expressions for $V_m(0)$ and $V_m(L)$ from Eq. 3.29.

Plotting the frequency behaviour of the conducting-end cables under external point-source stimulation, we see that the frequency selective behaviour and the resonances are reproduced as in the sealed-end case (fig. 3.16).

3.2 Summary of results

Our results show that the frequency response of passive cylindrical neurons, to oscillating point-source stimulation (aligned to one of the neuron ends), has two qualitatively distinct regimes. In the first instance, when measurements are performed at the neuron end next to the point-source, the frequency profile (for both FEM and

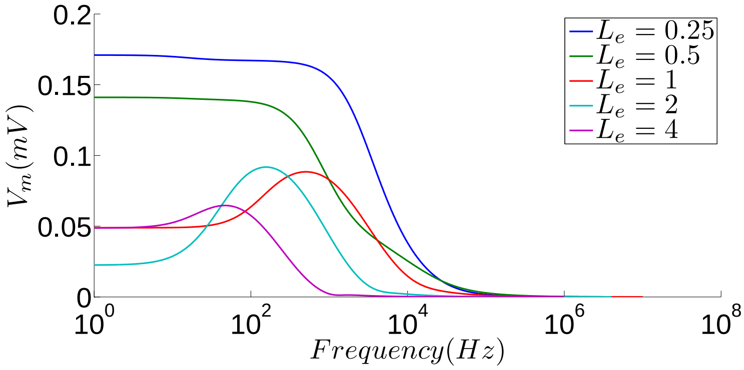

(a)

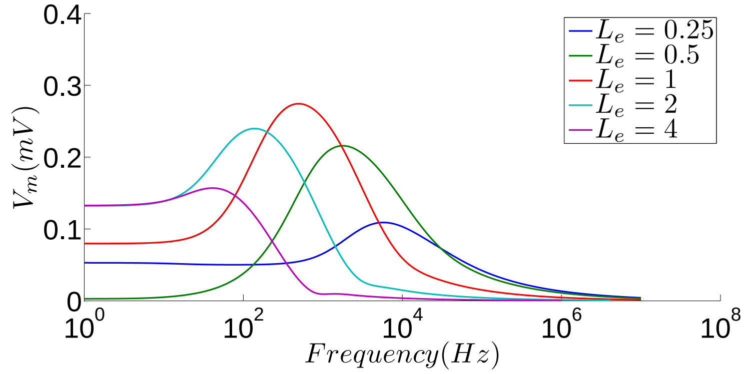

(b)

Figure 3.16: The "passive resonance" is observed for point stimulation of cable neurons with conductive ends (horizontal electrode-cell distance is $d = 0.1\lambda$). Frequency response of cable neurons of various electrotonic lengths (box top right). a) Point-source is placed at $x = 0$ and the measurement is performed at $x = \frac{L}{4}$. b) Point-source is placed at $x = \frac{L}{4}$ and the measurement is performed at $x = 0$. The "passive resonances" are apparent as in the sealed-end cases above. The parameters used to produce these figures are as given in table 1.1, with the cable radius $a = 2$ μm and $\lambda = 447.2$ μm.

Table 3.1: Comparison between the cable and FEM models for point source stimulation of cylindrical neuron at one end ($x = 0$)

	Compact (small $\frac{l}{a}$)	**Long (large $\frac{l}{a}$)**
Steady-state	Significant difference in the steady-state V_m measured for all values of x	Minor difference in the steady-state V_m measured on and near the point of stimulation at $x = 0$
Oscillating	Same frequency response for V_m (effective time constants) measured for all values of x	Same frequency response for V_m (effective time constants, resonances etc.) measured for all values of x

cable models) are similar to that for uniform field stimulation, with similar values of the frequency drop-off points (fig. 3.6). The earlier result that compact neurons remain responsive to higher frequency stimulation (2) is also validated for point-source electric field stimulation (figs. 3.5 and 3.6).

When measurements are performed away from the neuron end (at particular values of x), with a long neuron close to the point-source, spatially localized resonances are observed (for both FEM and Cable models) purely mediated by the passive properties of the field-cell system, not observed in the uniform field case (chapter 2). Similar resonances are also observed when the point-source is placed at $x > 0$ but not when placed next to the center of the neuron (fig. 3.15). Thus these resonances are correlated with the asymmetrical polarization of the neuron alongside the non-uniformity of the extracellular electric field.

Comparing the FEM and cable models (table 3.1) significant difference occurs for compact neurons in the magnitudes of the induced steady-state V_m, due to the radial orientation of the extracellular field (fig. 3.4). A significant difference between cable and FEM models is also observed for compact neurons under uniform field stimulation (fig. 2.14), but less so then in the point stimulation case.

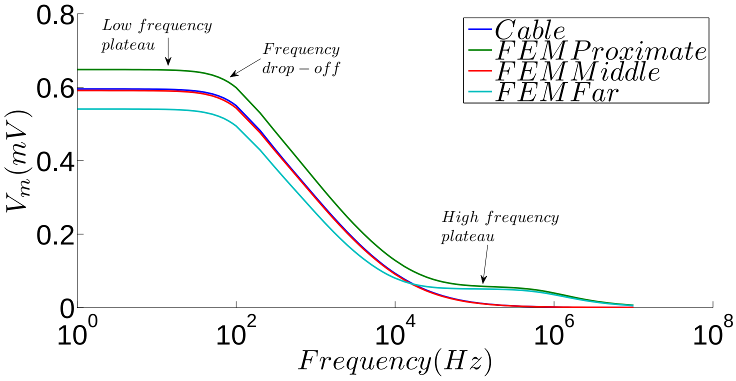

Figure 3.17: The different features of the frequency profile for the point-stimulated FEM cylindrical neuron. The FEM and cable plots are as in fig. 3.7a for cylindrical neurons of electrotonic length $L_e = 1$, in an oscillating point-source electric field ($I = 100$ nA, $d = 0.1\lambda$ and V_m is measured at the cable end, $x = l$). In agreement with the cable plot, all three FEM profiles exhibit the low frequency plateau and the same frequency drop-off. In contrast with the cable plot, the "proximate" and "far" point profiles also exhibit a high frequency plateau. This high frequency plateau is also seen in measurements with the "passive resonance" (fig. 3.14).

Chapter 4

Quasi-active and fully active membranes

In the analysis above, we have only studied passive membranes with a voltage independent membrane conductance. Neuronal membranes of course have active conductances which give rise to phenomena such as subthreshold resonance and action potentials. We now go on to include voltage-gated currents into our field-cell formalism and investigate the interaction between the active biophysical properties of the neuronal membrane and the spatial effects found in the previous chapters for passive neurons. We look at two different biophysical membranes. Firstly, a quasi-active membrane with the inclusion of one kind of voltage-gated channel (fig. 4.1a), to give a two-variable system which is known to lead to subthreshold resonance at particular frequencies, when stimulated via current injection. We linearize this system of equations around a holding voltage to yield the analytical solutions for the spherical and cable cells in an oscillating uniform field, and the numerical finite-element results for cylindrical neurons of various shapes. Secondly, we include the Hodgkin Huxley sodium and potassium currents in our model membrane (fig. 4.1c) and use the the finite-element method to obtain the full dynamic solution for an active, spiking neuron in an oscillating electric field.

Like in the case of passive neurons (figs. 1.4, 2.2b), the quasi-active and Hodgkin Huxley neuronal membranes can be described by electric circuit models. In the quasi-active case, the active system with an extra voltage-gated conductance along with the capacitive and leak paths (fig. 4.1a) is linearized to give a capacitive, a resistive (with conductance g_T) and an additional parallel path in the circuit described by a resistance κ and an inductance L in series (fig. 4.1b, Eq.). For the Hodgkin Huxley case, the membrane can be described by adding two extra resistive pathways to the passive circuit, consisting of the potassium and sodium voltage-gated conductances (fig. 4.1c).

Along with making our model biophysically realistic with the inclusion of active currents, we go on to embed our neuron model in an array of cells in order to validate our results at the level of neuronal tissue.

4.1 Quasi-active membrane

The inclusion of a voltage-gated, active conductance in our field-cell framework results in a two-variable system of equations for the membrane current

$$J = -\mathbf{n} \cdot (\sigma_i \nabla V_i) \tag{4.1}$$

$$= c_m \tfrac{\partial}{\partial t} V_m + g_L (V_m - E_L) + g_n n (V_m - E_n) \tag{4.2}$$

$$= -\mathbf{n} \cdot (\sigma_e \nabla V_e) \tag{4.3}$$

$$\tau_n \tfrac{dn}{dt} = n_\infty (V_m) - n \tag{4.4}$$

where n is the fraction of open voltage-gated channels, g_n is the maximum membrane conductance per unit area through the active channels, E_n is the reversal potential of the ionic species the active channels carry, τ_n is the relaxation time and n_∞ is the steady-state value of n. Using a mathematical linearization of the above two-variable model, resonance properties of neurons can be studied using a conductance based description [61]. Below spike threshold (Eqs. 4.1 and 4.4) can be linearized around

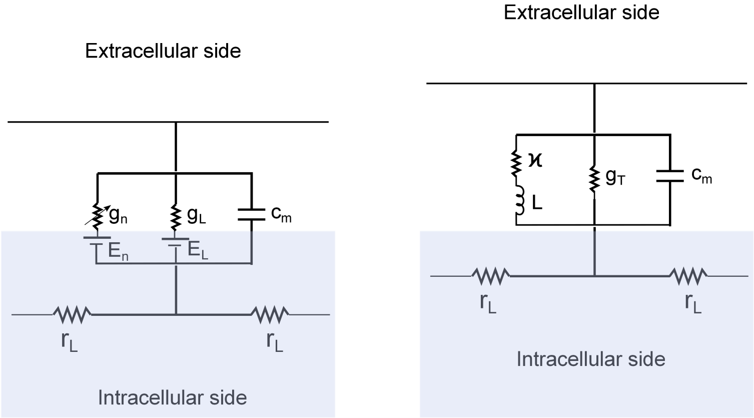

(a) Active membrane (b) Quasi-active membrane

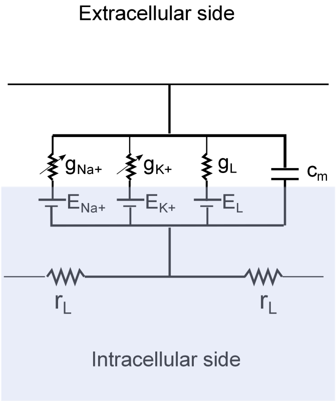

(c) Hodgkin Huxley membrane

Figure 4.1: Electric circuit models of active membranes. a) Representation of non-linearized two-component system with one type of voltage-gated channel. b) The LRC Circuit representing the the linearised form of the two-component system in a). The inductance, $L = \frac{\tau_n}{\kappa}$ and the conductances are given by $\kappa = g_n(V_m^* - E_n)\frac{dn_\infty}{dV_m}|_{V_m^*}$ and $g_T = g_L + g_n n^*$. c) Circuit representing the fully active Hodgkin Huxley membrane, with the respective sodium, potassium and leak conductances.

a holding voltage V_m^* (see e.g. [83]) to give

$$j = -\mathbf{n} \cdot (\sigma_i \nabla V_i) = c_m \tfrac{\partial}{\partial t} v_m + g_T v_m + \kappa y = -\mathbf{n} \cdot (\sigma_e \nabla V_e) \tag{4.5}$$

$$\tau_n \tfrac{\partial}{\partial t} y = v_m - y \tag{4.6}$$

where $y = \delta n \left(\frac{dn_\infty}{dV_m} |_{V_m^*} \right)^{-1}$, j, v_e, v_i, v_m and δn are deviations of J, V_e, V_i, V_m and n respectively from their fixed points, $g_T = g_L + g_n n^*$ with n^* as the holding value of n and $\kappa = g_n \left(V_m^* - E_n\right) \frac{dn_\infty}{dV_m}|_{V_m^*}$. Defining $I_n = \kappa y$, Eqs. 4.5 and 4.6 can be rewritten as

$$j = -\mathbf{n} \cdot (\sigma_i \nabla V_i) = c_m \tfrac{\partial}{\partial t} v_m + g_T v_m + I_n = -\mathbf{n} \cdot (\sigma_e \nabla V_e) \tag{4.7}$$

$$\tfrac{\tau_n}{\kappa} \tfrac{\partial}{\partial t} I_n = v_m - \tfrac{I_n}{\kappa} \tag{4.8}$$

The resultant linearized system and the resonant dynamics can thus be described by an a 'LRC' circuit (fig. 4.1b), with an inductance given by $L = \frac{\tau_n}{\kappa}$.

If we have the solution form $V_m(t) = V + \hat{V} e^{i\omega t}$, we identify $V_m^* = V$ and $v_m = \hat{V} e^{i\omega t}$, which in turn implies the forms $y = \hat{y} e^{i\omega t}$ and $j = \hat{j} e^{i\omega t}$. Inserting these solution forms into the linearized equations Eqs. 4.5 and 4.6, we obtain the boundary condition for the quasi-active membrane

$$\hat{j} = -\mathbf{n} \cdot (\sigma_i \nabla \hat{V}_i) = \left(i\omega c_m + g_T + \frac{\kappa}{1 + i\omega\tau_n} \right) \hat{V} = -\mathbf{n} \cdot \left(\sigma_e \nabla \hat{V}_e \right) \tag{4.9}$$

As in the case for the passive membrane, Eq. 4.9 implies that the steady-state result can again be mapped on to the result for the active membranes, this time by mapping

$$g_L \rightarrow g_T + i\omega c_m + \frac{\kappa}{1 + i\omega\tau_n} \tag{4.10}$$

Thus using the expression for the membrane potential of the passive current-injected

Table 4.1: Parameters for the quasi-active membrane model

Parameter	Denotation	value
Extracellular medium conductivity	σ_e	0.2 μSμm^{-1}
Cytoplasmic conductivity	σ_i	0.2 μSμm^{-1}
Membrane leak conductance	g_L	1×10^{-6} μSμm^{-2}
Membrane active conductance	g_n	1×10^{-6} μSμm^{-2}
Membrane capacitance	c_m	1×10^{-5} nFμm^{-2}
Leak reversal potential	E_L	-68 mV
I_H reversal potential	E_n	-41 mV
I_H relaxation time	τ_n	38 ms
Holding value of n	n^*	0.1324
Holding value of V_m	V_m^*	-64.84 mV

neuron (Eq. 1.24), we obtain

$$\hat{V} = \frac{I_{app}}{i\omega c_m + g_T + \frac{\kappa}{1+i\omega\tau_n}} \tag{4.11}$$

as the oscillatory part of the membrane potential expression for the current-injected neuron with the active conductance. Similarly using Eq. 1.20, the oscillatory part of the spherical solution with the active conductance becomes (See appendix D)

$$\hat{V} = \frac{3\sigma_e E a \cos\theta}{2\sigma_e + (1+2\mu)\left(g_T + i\omega c_m + \frac{\kappa}{1+i\omega\tau_n}\right)a} \tag{4.12}$$

In this thesis, for the active membrane current we have used the reduced form of the I_H current model (see [61]) with the parameters given in (table 4.1). Taking the expression for $n_\infty = \frac{1}{1+e^{\frac{V_m+78\text{mV}}{7\text{mV}}}}$, these parameters result in the value of $\kappa = 3.9133 \times 10^{-7}$ μS μm^{-2}.

4.1.1 The time-dependent spherical and cylindrical neurons with quasi-active membranes

With direct current-injection, the two-variable model for an active membrane (Eqs. 4.1-4.12) exhibits an impedance curve (fig. 4.2a) with a clear resonance at a frequency given by

$$f_{inj} = \frac{1}{2\pi\tau_n}\left(\frac{1}{c_m}\sqrt{\tau_n^2(\kappa^2 + 2g_T\kappa) + 2\kappa\tau_n c_m} - 1\right)^{\frac{1}{2}} \tag{4.13}$$

For the parameter values given (table 4.1) $f_{inj} = 7.5$ Hz.

With external uniform field stimulation of a spherical neuron, the resonance peak as given by the analytical solution shifts towards higher frequencies (as expected in light of the passive case)

$$f_{sph} = \frac{1}{2\pi\tau_n}\left(\frac{1}{Rc_m}\sqrt{\tau_n^2\{R^2(\kappa^2 + 2g_T\kappa) + 4\sigma_e R\kappa\} + 2R^2\kappa\tau_n c_m} - 1\right)^{\frac{1}{2}} \tag{4.14}$$

with $R = (1 + 2\sigma_e/\sigma_i)a$. For the parameter values given (table 4.1) $f_{sph} = 82.4$ Hz. The above expressions for f_{inj} and f_{sph} were obtained by calculating the amplitudes for the complex expressions in Eqs. 4.11 and 4.12 respectively, and maximizing them with respect to the angular frequency ω. Interestingly, the size of the subthreshold resonance peak for the spherical neuron diminishes drastically to a negligible size (fig. 4.2a).

To investigate this further, we utilize the quasi-active mapping in Eq. 4.10 with our numerical and analytical cable models of field stimulated cylindrical neurons, exploring the relationship between the cell dimensions and the quasi-active resonance behaviour. As in the case of the spherical neuron, the $L_e = 0.5$ and 1 cylindrical neurons do not exhibit significant resonances (fig. 4.2b and 4.2c). With the $L_e = 2$ neuron however, the resonance is recovered (fig. 4.2d). Therefore our results demonstrate that electrotonically longer neurons exhibit more pronounced resonant behaviour, as well as having a lower drop-off frequency. This is in accord with our observation above of the lack of a resonance peak in the case of the compact spherical neuron under oscillating uniform field stimulation. As can also be seen in figs. 4.2b, 4.2c and 4.2d, the FEM and cable results agree very well with each other as we are in the regime of non-compact neurons, where the radial extent of the neuron has an insignificant impact on the neuronal polarization.

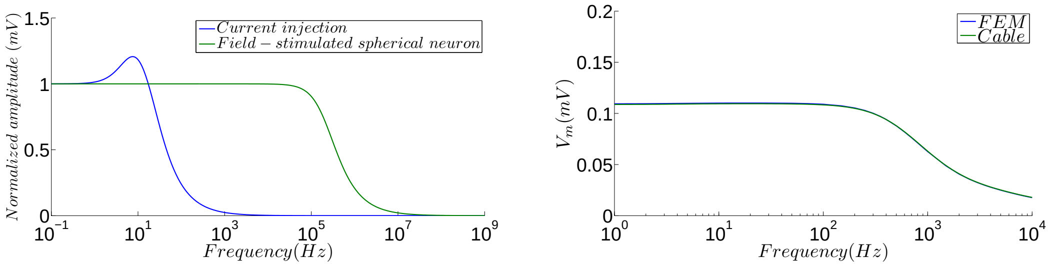

(a) Current-injected and spherical neuron (b) $L_e = 0.5$ neuron

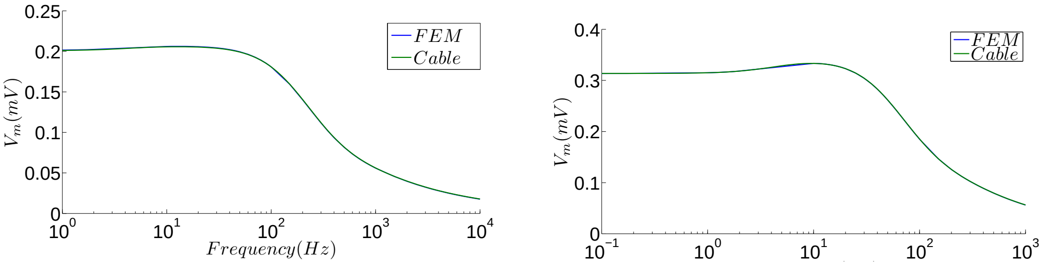

(c) $L_e = 1$ neuron (d) $L_e = 2$ neuron

Figure 4.2: Frequency response for field-stimulated neurons of various shapes (Spherical, finite-element and cable results) with quasi-active membranes in a uniform oscillating field. a) Comparison between the current-injected neuron and the field-stimulated spherical neuron of radius 10 μm (analytical solutions in Eqs. 4.11 and 4.12 respectively). The subthreshold resonance is clearly evident in the current-injected case whereas it is eliminated in the field-stimulated spherical neuron case. b-d) Comparison between field-stimulated cylindrical neurons of electrotonic lengths $L_e = 0.5$, 1 and 2, respectively, with the measurement performed at the cable end ($x = l$). The resonance disappears for neurons with low electrotonic lengths but is recovered for elongated neurons. Both the FEM and cable results agree well for the given neuron sizes. The cable neurons under consideration have sealed ends. The parameters used to produce these figures are as given in table 4.1, with the cable radius $a = 2$ μm and $\lambda = 447.2$ μm.

In order to understand this relationship between the subthreshold resonance and the neuron shape, we again invoke the concept of the parallel bulk media conductance as in section 2.6. The resonance phenomenon occurs due to the interaction between the passive and the active properties of the membrane, where a combination of a low-pass and a high-pass filtering occurs [60]. The low-pass filtering of course is provided by the parallel capacitance and leak conductance of the membrane. The high-pass filtering is provided by the voltage-gated channels which carry currents that actively oppose membrane voltage changes and are also slowly activating relative to the membrane time constant. In short, the subthreshold resonance is a phenomena mediated by the neuronal membrane and hence manifests only when most of the charge redistribution takes place through the membrane. This occurs only for electrotonically long neurons, where the bulk media conductances are low. Thus as long as the cell is compact, the parallel bulk media conductance is high and dominant, and the system exhibits a small effective membrane time constant. With an increasing electrotonic length however, the effective bulk media conductance decreases due to the increasing distances along cylinder length and a decreasing cross-sectional area through which charge redistribution takes place, and thus the effective membrane time constant increases with the cell reverting to current-injection like, resonance behaviour.

4.2 Fully active Hodgkin Huxley neurons

We now proceed to implement a fully active membrane model with Hodgkin Huxley currents into our finite-element field-neuron system. In particular we study the behaviour of the spiking neuron in the presence of a non-uniform field due to a point current source. The nonlinear Hodgkin Huxley membrane model for the generation of action potentials is given by including a delayed-rectified K^+ current and a transient

Na$^+$ current into the transmembrane current density J in our field-cell system

$$J = -\mathbf{n} \cdot (\sigma_i \nabla V_i) \tag{4.15}$$

$$= c_m \frac{\partial}{\partial t} V_m + g_L(V_m - E_L) + g_K n^4 (V_m - E_K) + g_{Na} m^3 h (V_m - E_{Na}) \tag{4.16}$$

$$= -\mathbf{n} \cdot (\sigma_e \nabla V_e) \tag{4.17}$$

where as before g_K and g_{Na} are the maximal conductances per unit area for the potassium and sodium ions respectively, E_K and E_{Na} are the potassium and sodium reversal potentials respectively, and n, m and h are the gating variables. Eq. 4.15 represents the non-space-clamped spatial Hodgkin Huxley model, where V_m is dependent on the neuronal location as well as on time. The gating variables are defined by the equation set

$$\frac{dj}{dt} = \alpha_j(1-j) - \beta_j j \qquad j \epsilon \{n,\, m,\, h\} \tag{4.18}$$

$$\alpha_n = \frac{0.01(V_m + 55\text{ mV})}{1 - \exp(-0.1(V_m + 55\text{ mV}))} \tag{4.19}$$

$$\beta_n = 0.125 \exp(-0.0125(V_m + 65\text{ mV})) \tag{4.20}$$

$$\alpha_m = \frac{0.1(V_m + 40\text{ mV})}{1 - \exp(-0.1(V_m + 40\text{ mV}))} \tag{4.21}$$

$$\beta_m = 4 \exp(-0.0556(V_m + 65\text{ mV})) \tag{4.22}$$

$$\alpha_h = 0.07 \exp(-0.05(V_m + 65\text{ mV})) \tag{4.23}$$

$$\beta_h = 1/(1 + \exp(-0.1(V_m + 35\text{ mV}))) \tag{4.24}$$

where α_j and β_j are the opening and closing rates for the specific gating variable j. The parameter values used in this thesis for the Hodgkin Huxley membrane model are taken from [84] and given in table 4.2.

As the model of a three-dimensional spiking neuron in a non-uniform electric field, incorporating full two-way feedback between the neuron and the field is a novel and significant step towards understanding field-neuron interactions, we describe the model construction below in some detail. It should be noted that the methodology used in this thesis for the FEM simulations is similar to that used by Elia et al [85]. The three-dimensional geometry is constructed as described in subsection 2.5.2, but with a three-dimensional intracellular cylindrical domain and a cubic extracellular domain (fig. 3.1). The outer boundaries of the extracellular domain are grounded and a geometrical point feature is placed in the extracellular domain, horizontally aligned with one end of the cylindrical cell. This point feature provides for the oscillating extracellular point current source. As before, the boundary surface between the the two bulk domains provides for the "infinitely thin" neuronal membrane, substantially reducing the computational burden which will be imposed by having a membrane with a finite thickness. Using the "AC/DC" module within COMSOL, two different "electric currents" physics interfaces are set up for the two domains, both set to be purely conductive. As before, two separate solution variables V_i and V_e are defined in COMSOL, which are active for the intracellular and extracellular domains respectively, while both are active at the boundary. In order to implement the nonlinear differential equations at the neuronal membrane, we add a "weak form" boundary interface within COMSOL and define it to be active only locally at the membrane boundary. In the bulk "electric currents" interfaces, the transmembrane current density at the membrane is simply defined as J. Using the "weak form" boundary interface we define the current density variable J and the gating variables h, m and n to be active locally at the membrane boundary and use Eqs. 4.15 - 4.24 in their weak forms to implement the dynamic behaviour of V_m and the gating variables. As with the full Hodgkin Huxley equations a simple mapping from the steady-state to the time-varying solution is no longer possible, a full transient solution is required. Thus the "time-dependent" study type with a fully coupled and direct "MUMPS" solver is used within COMSOL. This time-dependent mode of the COMSOL FEM solver solves the boundary value problem explicitly in time. In order to ensure that the outer domain boundaries do not influence the extracellular electric field, the length of the extracellular cubic domain is ensured to be three times the

Table 4.2: Parameters for the Hodgkin Huxley membrane model

Parameter	Denotation	value
Extracellular medium conductivity	σ_e	0.2 μSμm^{-1}
Cytoplasmic conductivity	σ_i	0.2 μSμm^{-1}
Membrane leak conductance	g_L	3×10^{-6} μSμm^{-2}
Maximal sodium conductance	g_{Na}	1.2×10^{-3} μSμm^{-2}
Maximal potassium conductance	g_K	3.6×10^{-4} μSμm^{-2}
Leak reversal potential	E_L	-68 mV
Sodium reversal potential	E_{Na}	50 mV
Potassium reversal potential	E_K	-77 mV
Membrane capacitance	c_m	1×10^{-5} nFμm^{-2}

length of the cylindrical cell. The time resolution used is 0.1 ms.

We investigate the spiking behaviour of the $L_e = 1$ neuron ($a = 2$ μm and $L = 258.2$ μm) with conducting ends, under point stimulation from an extracellular current source, which is horizontally aligned with one of the cell's ends and is 0.1λ away from it, with $\lambda = 258.2$ μm (using the parameters in table 4.2). The subthreshold frequency profile (fig. 4.3a) indicates a very strong resonance starting at about 10 Hz and peaking at about 1000 Hz. Looking at the spiking behaviour of the Hodgkin Huxley neuron under field stimulation at various frequencies we see a translation of the subthreshold passive resonance on to the spiking behaviour. As can be seen, at a field frequency of 100 Hz, an extracellular current amplitude of 2 μA is sufficient to trigger action potentials in the neuron (fig. 4.3b), whereas the same current amplitude fails to trigger spiking at 10 Hz (fig. 4.4b). Thus we see a clear frequency preference in the occurrence of spiking, as dictated by the subthreshold frequency profile of the neuron. The 100 Hz frequency stimulation causes spiking to occur at a frequency of 50 Hz, thus missing every other cycle. The 10 Hz stimulation induces subthreshold oscillations at 10 Hz which fail to develop into spikes, whereas the 5 Hz stimulation induces smaller low-frequency oscillations in the membrane potential. The resonance can also be detected in the subthreshold oscillation amplitudes with the stimulation of $I = 100$ nA (figs. 4.3a and 4.4c). It should be noted that the amplitudes of the induced subthreshold oscillations in V_m (figs. 4.3a and

4.4c) are a function of the electrode-neuron distance d and the stimulating current I, with a smaller d and a larger I causing an increase in the amplitude. Indeed in electrophysiological experiments, extracellular stimulation can be used to depolarize the membrane sufficiently for triggering spikes. Also endogenously with naturally occurring electric fields, the amplitude of the induced oscillations will vary depending on the neuronal activity, density and geometry. It has been shown that electric fields of physiological strengths (~ 2 mV/mm) induce somatic polarizations of around half a mV in the cortex, which in turn are sufficient in producing subthreshold network level effects [59]. Thus the small magnitude of the induced oscillations in V_m shown in figs. 4.3a and 4.4c do not imply a lack of effect. It is the size of the resonance peak relative to the low frequency, base level of V_m (fig. 4.3a), which is the key variable in determining the significance of the effect.

4.3 Field interactions with neurons embedded in tissue

The neuron models considered above exist in isolation within the extracellular space. This is an unrealistic scenario for in vivo cells within tissue, where the extracellular space is populated with other neurons and glia. As found in our investigations above, the extracellular bulk conductances play a crucial role in determining the effective membrane time constant of a neuron exposed to an electric field, where the extracellular space provides a parallel path for the polarization current flow. Thus a change in the extracellular configuration, such as placing in it other neurons with highly resistive membranes would necessarily lower the overall extracellular bulk conductance and effect the dynamics of the system.

Thus it is not obvious if the relationship between the geometry and the high-frequency response of the cell obtained in our models above is valid for neurons in tissue. We thus utilized COMSOL Multiphysics to simulate the behaviour of three-dimensional synaptically unconnected neuronal arrays exposed to oscillating electric fields. The arrays were constructed by having a single column of neurons, stacked

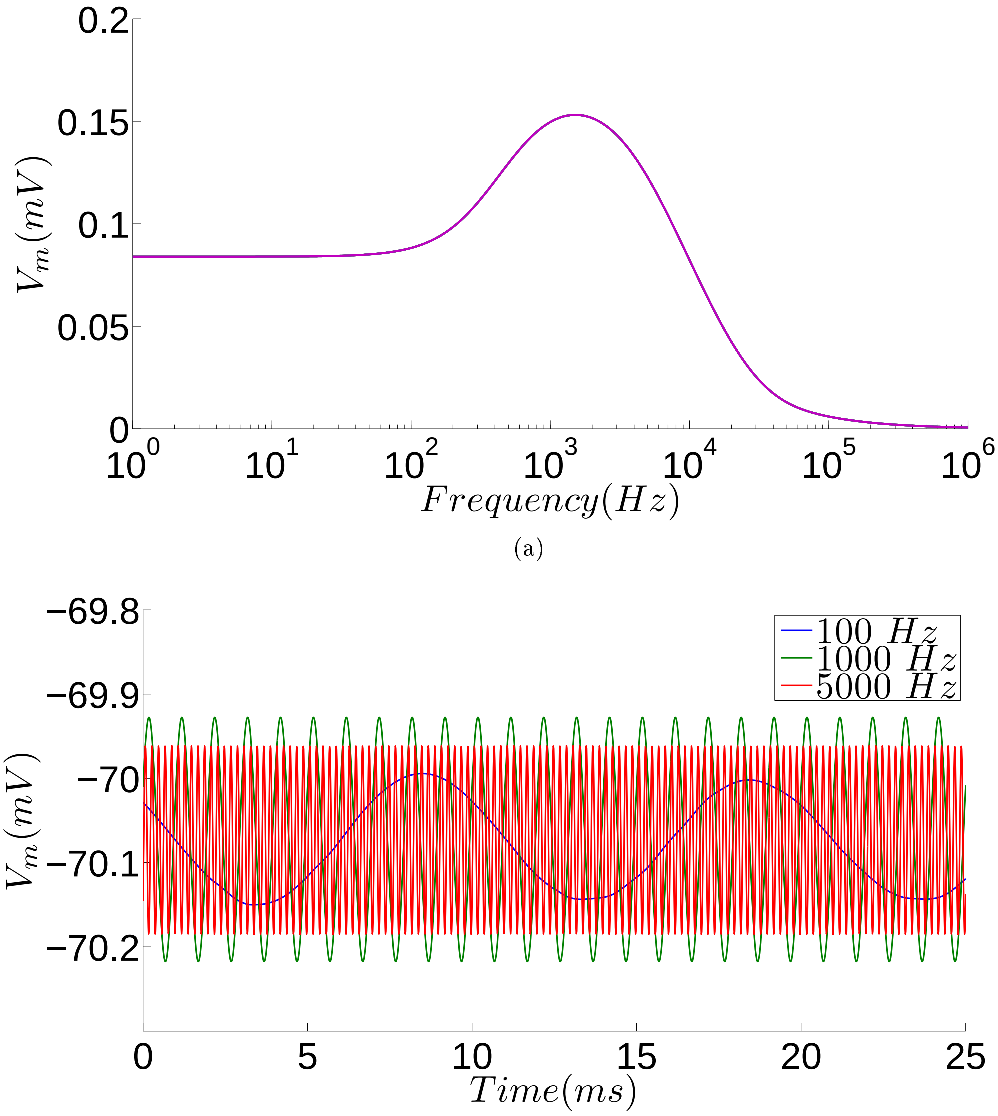

(a)

(b)

Figure 4.3: The "passive resonance" in the Hodgkin Huxley Neuron. a) The resonance profile for a passive cable neuron of size $L_e = 1$, under point stimulation ($I = 100$ nA) at $x = 0$ and measured at $x = 0.25L$. The horizontal electrode-cell distance is $d = 0.1\lambda$. The parameters are as given in table 1.1b) The dynamic subthreshold oscillations in a finite-element Hodgkin Huxley neuron of size $L_e = 1$ and $I = 100$ nA. The parameters are as given in table 4.2. The stimulation and measurement points are as in a). The resonance can be seen in the amplitudes, going from 100-5000 Hz. The neurons considered have sealed ends with the cable radius $a = 2$ μm and $\lambda = 447.2$ μm.

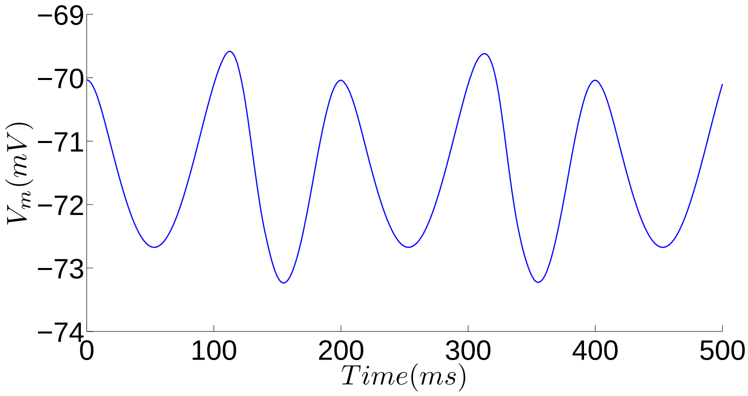

(a) $f = 5$ Hz neuron

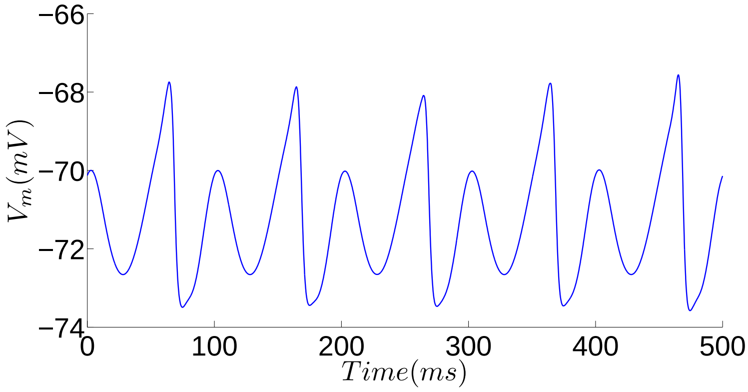

(b) $f = 10$ Hz neuron

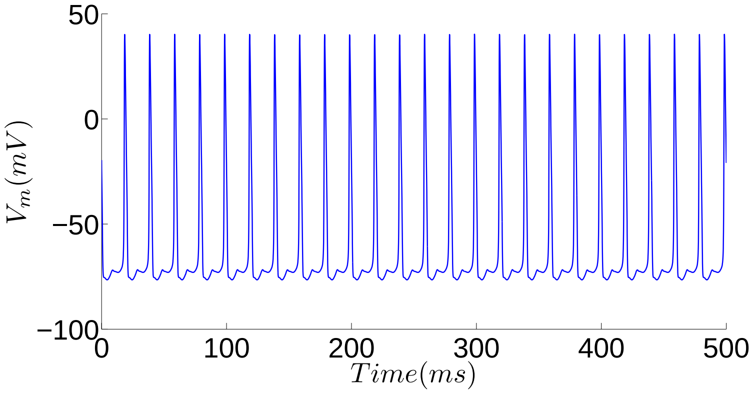

(c) $f = 100$ Hz

Figure 4.4: A point-stimulated, finite-element spiking neuron of size $L_e = 1$ and $I = 100$ nA (the stimulation and measurement points are as in fig. 4.3). The rising amplitude due to the resonance can be seen going from a) 5 Hz to b) 10 Hz to c) 100 Hz with the 100 Hz neuron firing. $I = 2000$ nA for all the models. The parameters are as given in table 4.2. The neurons considered have sealed ends with the cable radius $a = 2$ μm and $\lambda = 447.2$ μm.

directly on top of each other in the direction of the field (along the x-axis), with periodic boundary conditions ensuring an effectively infinite number of neurons in the directions perpendicular to the field, along the x and y axes (fig. 4.5a). In order to implement the periodic boundary conditions, the shape of the neuron model was taken to be cuboidal with both the width and the length fixed as 4 μm and the height along the field direction taken to be h μm (with cell size denoted as $4 \times 4 \times h$ μm). We consider both the case of the neuron with the passive and the quasi-active membrane, with the biophysical parameter values given in tables 1.1 and 4.1. The steady-state and time-dependent field responses of the isolated cuboidal neuron model were shown to be very similar to that of the cylindrical model simulated above. Cells of varying heights (along the x-axis) were considered, with the number of vertical layers altered to keep an approximate cumulative cell height of 100 μm (fig. 4.5a). The spacing between the cells, d was taken to be 1 μm in all three directions. Measurements are taken from the central cell in the array. A monolayer array with a single sheet of neurons was also simulated for comparison.

4.3.1 The array-embedded neuron with a passive membrane

For a passive cell embedded in a semi-infinite array exposed to a non-oscillating uniform field E (fig. 4.5a), the membrane potential along the x-axis, V_x takes a linear form $V_x = kEx$ with $k \approx 2$ (fig. 4.5b). Thus the presence of the surrounding cells significantly increases the effect of the applied field on an individual cell. The time-dependent frequency response of the embedded neuron also differs from the isolated case in having a drop-off frequency which is lower than that for the isolated neuron (fig. 4.6). The increase in cell to field coupling for the array-embedded neuron is primarily caused by the presence of cells within the $x - y$ plane of the neuron under observation, rather than the cells in the adjacent vertical layers, as demonstrated by the small difference between the monolayer and the full array results (fig. 4.6). The relationship between cell compactness and the high-frequency response is still clearly present for array-embedded neurons, with more compact neurons exhibiting higher drop-off frequencies ($> 10^5$ Hz for $4 \times 4 \times 4$ μm neurons and $< 10^4$ Hz for $4 \times 4 \times 32$ μm neurons - see fig. 4.6).

4.3.2 The array-embedded neuron with a quasi-active membrane

Incorporating the quasi-static membrane model into the field-cell system with the neuron embedded in an array, we see a clear relationship between the occurrence of the subthreshold voltage-gated resonance and the presence of the surrounding cells. In both the $4 \times 4 \times 256$ μm and the $4 \times 4 \times 512$ μm neurons we see the recovery of resonance when going from the isolated case to the field-embedded case. Furthermore, as in the isolated case, we see an increase in the resonance amplitude when going from the $4 \times 4 \times 256$ μm neuron to the more elongated $4 \times 4 \times 512$ μm neuron.

4.3.3 Explanation for the array results

The above results for array-embedded neurons can again be understood within the parallel bulk conductance framework established in the previous chapters. Our simulations demonstrate that cells embedded within arrays are more susceptible to the external field, with an induced V_m approximately twice that for the isolated case (fig. 4.5b). Similarly the frequency response of the array-embedded neuron is also altered with drop-off frequencies lower than those for isolated neurons (fig. 4.6). Furthermore, we see the recovery of resonance going from the isolated neuron to the array-embedded neuron case. We argue that all three of these effects can be understood as consequences of the decrease in the extracellular bulk media conductance, caused by the surrounding cells. The increased field to cell coupling is caused by the increased extracellular resistance shunting more of the applied current through the membrane of the observed neuron. The lower drop-off frequency on the other hand, results due to the increase in the parallel extracellular resistance causing an

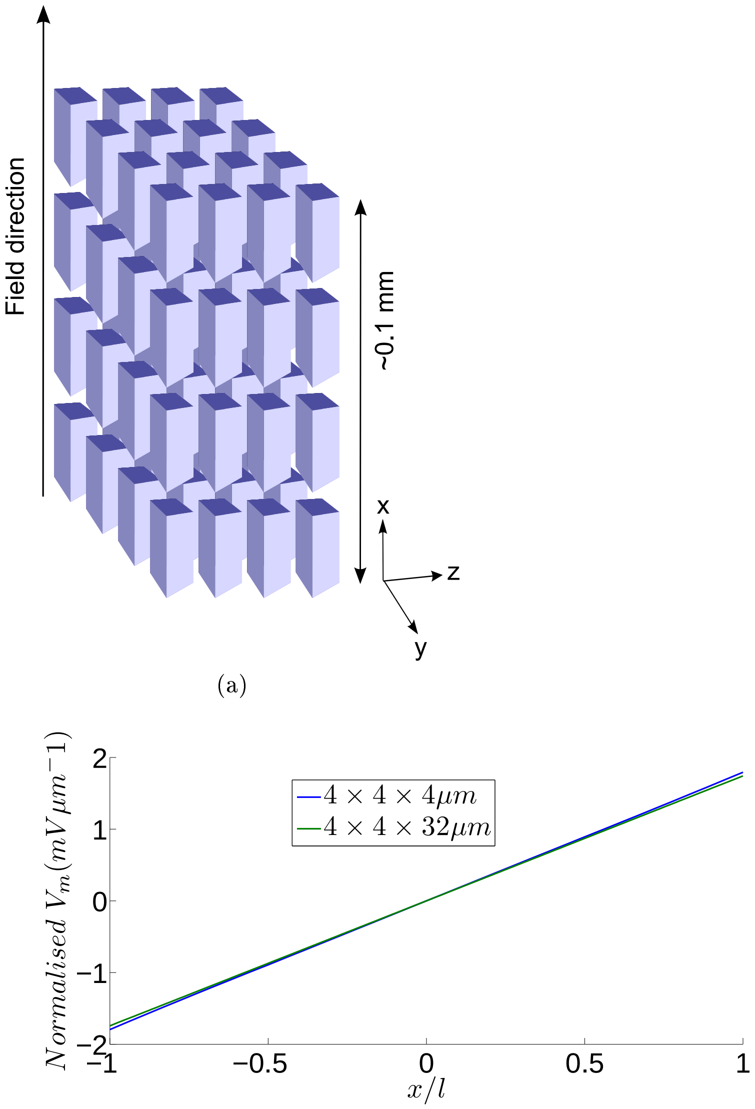

(a)

(b)

Figure 4.5: The semi-infinite neuronal array a) A schematic of the 3-dimensional field-stimulated neuronal array, simulated using the finite-element method. The periodic boundary conditions along the field-perpendicular axes simulate an effectively infinite number of neurons along these directions. The cumulative height of cells is maintained at approximately 100 μm above and below the central observed cell. b) Normalized steady-state membrane potential distribution, V_x/x for a $4 \times 4 \times 4$ and $4 \times 4 \times 32$ μm passive array-embedded neuron exposed to a non-oscillating electric field oriented along the x-axis. The field-coupling for the array-embedded neuron is much greater than for the isolated case, with the magnitude of the induced membrane potential approximately twice that for an isolated neuron. The parameters used to produce b) are as given in table 1.1. An $w \times d \times l$ neuron corresponds to a cell with width w, depth d and half-length l.

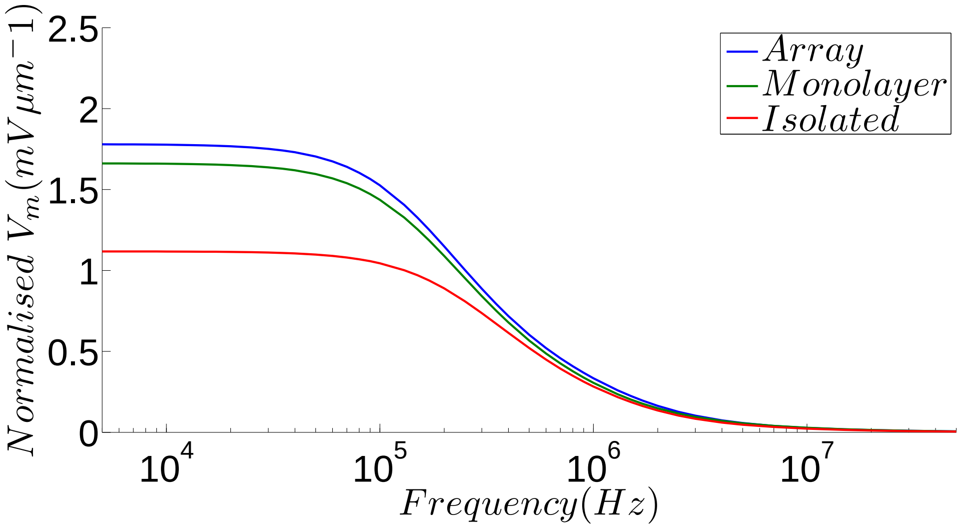

(a) $4 \times 4 \times 8$ μm neuron

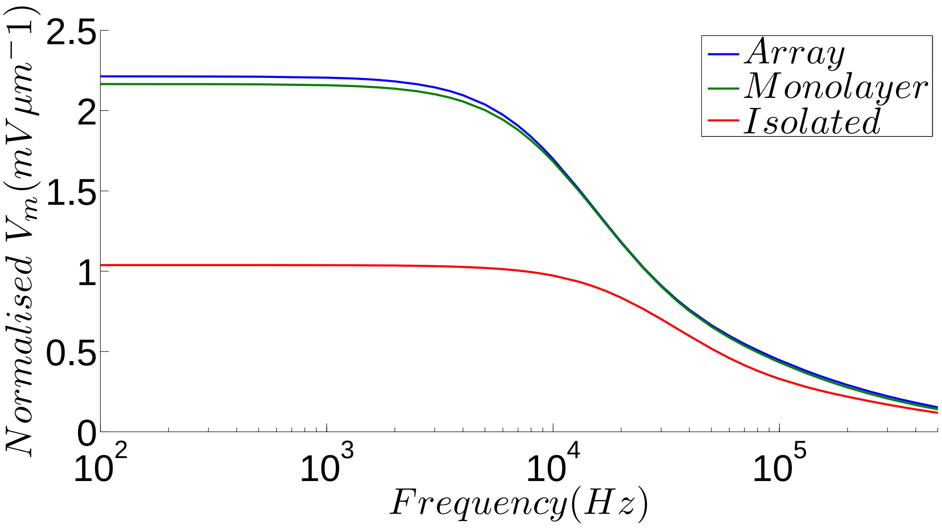

(b) $4 \times 4 \times 32$ μm neuron

Figure 4.6: Frequency response for a passive array-embedded neuron exposed to an oscillating electric field (the measurement is performed at the "top-right" corner of the central neuron). The array-embedded cell is compared with the monolayer-embedded and the isolated cases for cell sizes of a) $4 \times 4 \times 4$ μm and b) $4 \times 4 \times 32$ μm. The drop-off frequency decreases going from the isolated to the full array-embedded neuron, with the cells in the field-perpendicular plane primarily contributing to the change as demonstrated by the monolayer case. The effect of cell elongation on the drop-off frequency is still apparent with the array-embedded neuron. The parameters used to produce these figures are as given in table 1.1. An $w \times d \times l$ neuron corresponds to a cell with width w, depth d and half-length l.

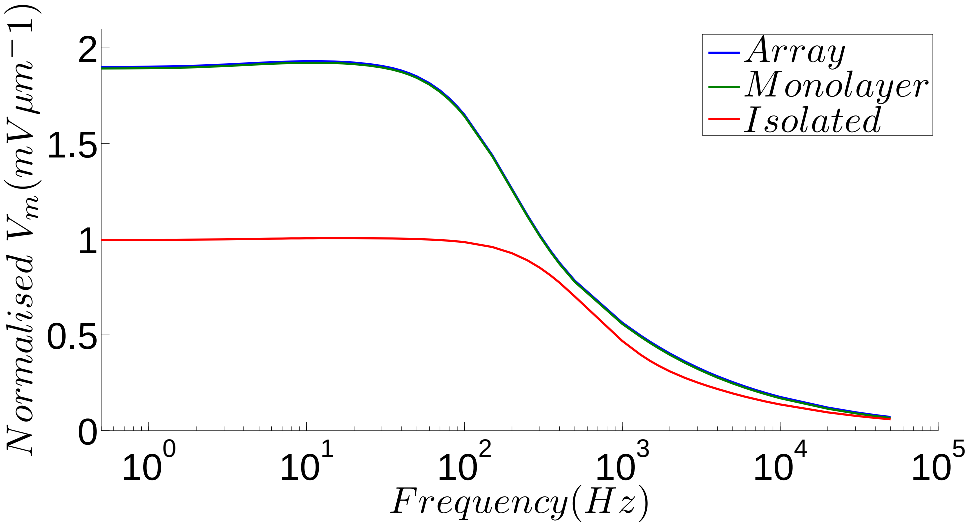

(a) $4 \times 4 \times 256$ μm neuron

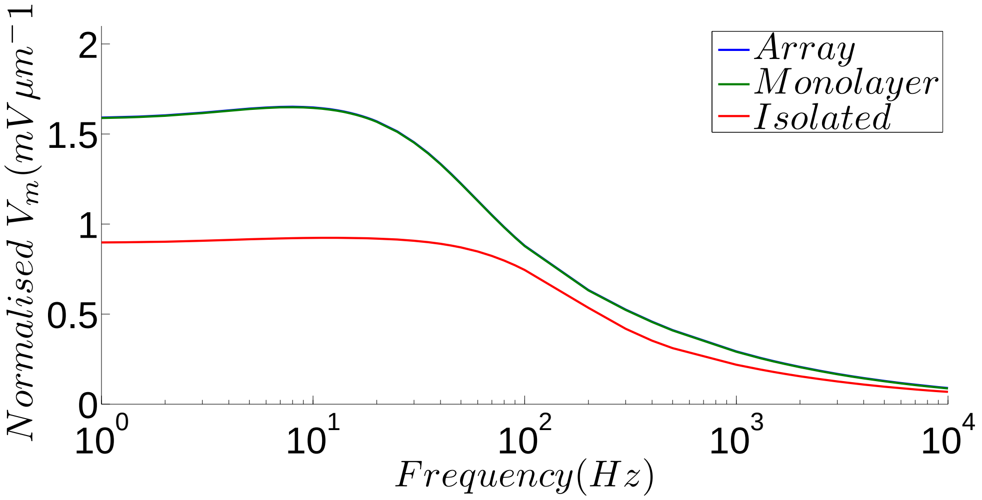

(b) $4 \times 4 \times 512$ μm neuron

Figure 4.7: Frequency response for a quasi-active field-stimulated neuron embedded in array and exposed to an oscillating electric field (the measurement is performed at the “top-right” corner of the central neuron). The array-embedded cell is compared with the monolayer-embedded and the isolated cases for cell sizes of a) $4 \times 4 \times 256$ μm and b) $4 \times 4 \times 512$ μm. Analogous to the isolated neuron case, the resonance reappears for the longer neuron. Additionally the resonance amplitude increases going from the isolated case to the monolayer-embedded or the field-embedded cases. The parameters used to produce these figures are as given in table 4.1. An $w \times d \times l$ neuron corresponds to a cell with width w, depth d and half-length l.

increase in the effective membrane time constant. Lastly, the increased shunting of the applied current through the membrane (due to the surrounding cells), causes the recovery of the subthreshold voltage-gated resonance. It should be noted that the influence of the surrounding cells on the steady-state and dynamic behaviour of the neuron under observation is dependent on the density of the array cells. Thus an increase in the intercellular distance within the neuronal array would lead to behaviour similar to the isolated case.

Significantly, the effect of cell elongation on the high-frequency neuronal response is still very much apparent for the array-embedded neurons (fig. 4.6), where the membrane potential of the more compact neurons is entrained up to higher frequencies of the applied extracellular electric field. Furthermore, the earlier results for the isolated quasi-active neurons are also carried over to the array-embedded case, where the subthreshold resonances are observed exhibiting a preference for a particular field frequency but only in the case of the non-compact neuron, where the polarization current flows primarily through the cell membrane. Thus our finite-element array model validates our findings from previous chapters that the shape and orientation of a neuron under electric field stimulation play a significant role in determining its frequency response, at the level of neuronal tissue.

Chapter 5

Conclusions

The primary mode of interneuronal communication within the nervous system, is through the synapse, where action potentials from presynaptic neurons induce potentials on the postsynaptic neuron through an electrochemical cascade, which are then in turn spatiotemporally integrated by the postsynaptic neuron. Gap junctions are another kind of specialized structure, which act as an electrical synapse, mediating electrical transmission between adjacent neurons. In this thesis I set out to investigate a relatively understudied, third mode of interneuronal communication, through the extracellular electric field. Referred to as ephaptic coupling when occurring endogenously, extracellular field effects have historically been thought of as negligible, with the LFP being regarded as an epiphenomena.

Recently however, field effects have been receiving greater attention, with studies showing an increasing relevance to physiological neuronal function. Frohlich and McCormick [59] have shown that weak electric fields of magnitudes comparable to endogenous LFPs, which cause small changes in the membrane potentials of single neurons, can enhance neocortical network activity. In particular, using an artificial feedback mechanism in vitro, linking the ongoing multiunit activity to the applied field, they have demonstrated that the feedback from the LFP could enhance the oscillatory nature of the structured neuronal activity. Anastassiou et al [57] have also recently shown that weak extracellular fields can strongly entrain subthreshold membrane oscillations and action potentials in individual neurons. These recent findings push our understanding of LFP functionality to being beyond epiphenomena.

5.1 A methodology for modeling two-way feedback coupling between the neuron and the field

Traditional models of neuronal interactions with electric fields either isolate the neuron from the extracellular field entirely or decouple the activity of the neuron from the field, where either an approximated and imposed extracellular field influences the neuron but is not in turn influenced by the neuronal activity [42, 43] or the neuron influences the extracellular field but is not in turn influenced by the extracellular activity [44]. Furthermore, these models often approximate neuronal elements as one-dimensional cables [42, 43, 45, 46]. Solving the required Maxwell's equations, we have developed a methodology, which enables us to model electric field effects in neurons with three-dimensional geometries and with full two-way field coupling, which in reality exists between the neuron and the extracellular field. This has required the combination of methodologies from two different fields, i.e. the coupling of nonlinear time-varying equations describing the membrane dynamics to the volume conductor behaviour of the Maxwell's equations in the extracellular and intracellular bulk media. We employed two different numerical methods, namely the finite-difference and the finite-element to solve the system of equations and compared these with the results of the cable equation. We have found that for electrotonically compact neurons, the cable equation is not adequate in determining the magnitude of the low-frequency membrane potential response to extracellular electric field stimulation. Due to the compactness of the neuron models, these results are relevant to neuronal somas. As the one-dimensional cable theory does not take into account the radial extent of the neuron, it significantly underestimates the magnitude of the membrane polarization, as demonstrated by our finite-element model. This highlights the need for two-way coupled field-cell models, which account for the three-dimensional geometry of the neuron.

Using the full capabilities of our finite-element models with COMSOL Multiphysics, we have simulated three-dimensional and field-coupled spiking neurons in inhomogeneous electric fields, and have also gone on to simulate arrays of synaptically unconnected neurons, validating our results for neurons in tissue. With the methodology established and given sufficient computational power, the finite-element models can easily be adapted and extended to investigating more complex neuronal geometries. A pioneering step towards modeling neurons within realistic extracellular field environments, the finite-element models presented in this thesis provide a powerful tool for understanding the nature of electric field interactions within biophysically and geometrically realistic neuronal networks.

5.2 Relationship between high-frequency response and electrotonic length

Modeling neuronal cylinders of various electrotonic lengths in sinusoidally oscillating uniform electric fields, we have elucidated the relationship between the neuronal shape and its frequency response. Using a combination of cable theory and finite-element methods, we have demonstrated that for a finite cylindrical neuron exposed to an axially oriented uniform field, its electrotonic length is the key determinant of its ability to stay responsive to higher stimulation frequencies in the kHz range; with the more elongated neurons being less responsive, having larger effective membrane time constants (fig. 2.4). We point out that although the cable methodology has been previously used to study cells in electric fields, the frequency analysis has been largely ignored. Our finite-element model on the other hand is completely novel and provides for a cross-comparison with the cable results.

The key concept which emerges from our analysis is that of the importance of the bulk media conductance in field-cell systems. The stimulation frequency at which the membrane potential begins to attenuate is dictated by the time constant of the membrane. The stimulation current dynamically polarizes the membrane with a time delay determined by the time constant. In typical current injection experiments, almost all of the current is driven through the neuronal membrane in order for the polarization to occur, hence the time constant is determined by the capacitance and the conductance of the membrane. In field-cell systems, due to the asymmetric polarization of the cell, the current redistribution during polarization takes place through the intra and extracellular media, which present a much lower resistance to the redistribution current. The bulk media thus provide a parallel pathway for the current to flow and hence the polarization occurs at a much shorter time scale, with the membrane potential of the neuron remaining entrained at a much higher frequency. In the case of the spherical cell the effective conductance of the field-cell system is given by the expression in Eq. 2.62. Thus as the radius a increases, the parallel bulk conductance increases and for $a \gg \frac{1}{g_L(\frac{1}{2\sigma_e}+\frac{1}{\sigma_i})}$ (unphysiologically large) the spherical cell reverts to current-injection like behaviour. Similarly, for finite cylindrical cells, the effective conductance is given by the expression in 2.63, which gives the parallel bulk conductance as $\frac{a}{2}\frac{\sigma_i}{l^2}$. Thus as long and narrow neurons present a greater bulk resistance to current flow, the current redistribution takes place mainly through the membrane and the cell is not as responsive to high-frequency stimulation.

This understanding of the role of the bulk conductances in field-cell systems offers a novel and elegant solution to the discrepancies in the experimental literature. In particular, it explains the difference between the frequency responses of the spherical myeloma cells [55] and the hippocampal pyramidal cells [36] when stimulated by uniform electric fields, with the lack of the high-frequency response in the pyramidal cells being explained as due to their elongation in the field direction.

Although the frequency profiles of the neurons, when measured at the end of the cell, show a higher frequency drop-off for compact neurons, the high-frequency asymptotes of all the neurons are the same regardless of their electrotonic length (fig. 2.4a). This means that at fixed field strength, the response of a compact neuron does not exceed that of an elongated neuron, hence there is no frequency selectivity. However, measurements performed away from the neuron end reveal a frequency selectivity occurring due to the increasingly exponential spatial profile of the membrane potential (fig. 2.4b).

5.3 Point stimulation of cylindrical neurons

In vivo, extracellular electric fields within the nervous system are produced by distributed current sinks and sources and hence are not uniform. In order to study the effects of inhomogeneous fields on neurons, we constructed cable theory and finite-element models of neurons in point-source electric fields. The cable model was solved by using the Green's function approach which, given the boundary conditions, yields an analytical solution for any given form of the extracellular potential. These models validate the results for the uniform field case, for a more realistic and experimentally relevant situation, showing a decreasing time constant with increasing electrotonic length and frequency selectivity occurring for off-end measurements (figs. 3.9, 3.10, 3.11 and 3.12). Our modeling could also help explain the high-frequency subthreshold entrainment (up to 100 Hz) observed by Anastassiou et al [57], in terms of the neuronal shape and field orientation. This study used unipolar extracellular electrodes to stimulate the compact somata of cortical neurons.

Furthermore the finite-element modeling further highlights the need for incorporating full two-way coupling between the field and the cell in the case of compact neurons, with the membrane potential profiles for the "proximate" and the "far" edges of the three-dimensional neuron significantly deviating from the cable results (fig. 3.4a). These results offer insight into how the shape and orientation of the neuron determines its frequency response to an oscillating field and are of special relevance to clinical studies looking at in vivo electric field stimulation, such as DBS [37–41]. Depending on the location of the stimulating electrode in the cortex, the neuronal geometry and orientation could be very stereotypical, with highly aligned and closely packed elongated neurons. Thus the orientation of the field with respect to the structured geometry of the neurons could play a significant role in determining the efficacy of the field application at different frequencies.

The off-end measurements of point-stimulated neurons reveal another phenomenon, which to our knowledge has not been reported in the literature, namely the "passive resonance" (fig. 4.3a). Revealed both by the cable and the finite-element models, this frequency preference in the field response is exhibited by the cylindrical neurons, with completely passive membranes and occurs for electrotonically long neurons with small electrode-cell distances. Exhibiting strong and broad resonance peaks dependent on the cell geometry, this passive frequency preference could play a significant role in endogenous and exogenous electric field interactions. In particular, it would be interesting to investigate its role in field interactions with neuronal networks. Using our finite-element model of a three-dimensional neuron with Hodgkin Huxley membrane currents, we have further demonstrated that the resonance observed in the passive neuron case is translated to the active case and indeed is exhibited in the occurrence of spikes, thus validating the passive results. As with the passive finite-element models, the construction of the Hodgkin-Huxley field-cell model required the two separate domains to be set up in COMSOL Multiphysics, with their boundary acting as a thin membrane and two different "electric currents" interfaces defined on each of the domains. In addition an extra "weak form" physics interface is defined locally on the membrane of the spiking model, which deals with the nonlinear Hodgkin Huxley differential equations and couples the membrane current to the bulk domains.

5.4 Interaction between the subthreshold voltage-gated resonance and field

As well as a passive and a Hodgkin Huxley model, we have also incorporated a quasi-active model of the neuronal membrane into our field-cell system. Mathematically, the simplest version of such a model requires the addition of a voltage-gated conductance into the passive description, resulting in a two-variable system of equations, which is subsequently linearized about fixed points to produce the quasi-active system of equations (Eqs. 4.5 and 4.6). In the case of current injection, such a model is known to lead to resonances at particular frequencies. The resonance here being produced by the intrinsic biophysics of the active membrane channels, in contrast to the "passive resonance" above caused by inhomogeneity of the applied field as experienced by the entirety of the passive cell. In the case of passive neurons, a key step towards solving the oscillatory analytical and numerical models was to recognize that the oscillatory solution can be obtained from the steady-state solution through a simple mapping (replacing g_L with $g_L + i\omega c_m$) . This mapping was then applied in all the passive models to very simply and quickly yield the oscillatory solutions without explicitly deriving or simulating fully transient, time-dependent solutions. With the quasi-active model as well, a simple mapping (replacing g_L with $g_T + i\omega c_m + \frac{\kappa}{1+i\omega\tau_n}$) converts the steady-state solution to an oscillatory one, eliminating the need to explicitly solve for the time-dependence. In particular, for the finite-element modeling in COMSOL Multiphysics, a simple application of the "frequency domain" study yields the appropriate solution.

Utilizing this mapping, we firstly solve for the case of the quasi-static spherical neuron in a uniform field, which interestingly shows a lack of resonance (fig. 4.2a). Going further and solving for the analytical cable neurons and the finite-element cylindrical neurons, we demonstrate a lack of resonance in the case of compact neurons but a recovery of resonance for the elongated ones (fig. 4.2). This behaviour again can be understood with the concept of the parallel bulk conductance. For compact neurons (including the spherical), the parallel bulk conductance is high and most of the current flows through the bulk media, which does not possess intrinsic resonance properties, hence no resonance. For elongated neurons, the parallel bulk conductance for current flow becomes low and most of the current flows through the resonant membrane, hence we see a recovery of resonance.

Our results imply that just like in the case of the high-frequency response of the neuronal membrane potential, the occurrence of subthreshold voltage-gated resonance is also dependent on the shape and orientation of the neuron with respect to the electric field. Thus according to our results, given appropriate active conductances, subthreshold voltage-gated resonance will occur when the cell is elongated in the direction of the applied field.

5.5 Constructing equivalent cylinders from real neuron geometries

The results obtained above for uniform and point-source field stimulation are for single dendritic cables modeled as cylinders. Real neurons however consist of intricate dendritic trees with many branches in various orientations. In order for our results to be applicable to realistic neurons, we need to match certain properties of these cells (measured through image reconstructions and electrophysiological experiments) with our equivalent dendritic cylinders [84]. Firstly, we need to equate the average electrotonic length of the tree ($< L_e^{tree} >$) with the electrotonic length of the cylinder ($L_e^{cyl} = \frac{L^{cyl}}{\lambda_{cyl}}$). This gives us equivalence of the voltage attenuation properties between the two. $< L_e^{tree} >$ is given by

$$< L_e^{tree} >= \sum_M \frac{l_k}{\lambda_k} \cos\theta_k \tag{5.1}$$

where k designates the particular segment of the realistic neuronal geometry divided in to M segments, l_k is the physical length of the segment, λ_k is the electrotonic length of the segment and θ_k is the angle between the segment and the direction of the applied field. It should be noted that in the formula for $< L_e >$ the projected length of the neuronal segment in the field direction is used to take account of the field orientation with respect to the neuronal segment. Thus equating $< L_e^{tree} >$ and L_e^{cyl} gives the equation

$$\frac{L^{cyl}}{\sqrt{\frac{a_{cyl}}{2g_L r_L}}} = \sum_M \frac{l_k}{\lambda_k} \cos\theta_k \tag{5.2}$$

where we have used the previously given definition of $\lambda_{cyl} = \sqrt{\frac{a_{cyl}}{2g_L r_L}}$ with a_{cyl} as the radius of the equivalent cylinder. The second property to match between the realistic geometry and the equivalent cylinder is the total surface area, which determines the total membrane conductance and capacitance. This gives us the second equation

$$A_{tree} = 2\pi a_{cyl} L_{cyl} \tag{5.3}$$

where A_{tree} is the measured total surface area of the realistic neuronal geometry and the expression $2\pi a_{cyl} L_{cyl}$ is the surface area of the equivalent cylinder. Thus using Eqs. 5.2 and 5.3 we can obtain values for the radius and length of the cylinder equivalent to the realistic neuron in its geometric and biophysical properties as

$$a_{cyl} = \left(\frac{A_{tree}}{\pi < L_e >}\right)^{\frac{2}{3}} \left(\frac{g_L r_L}{2}\right)^{\frac{1}{3}} \tag{5.4}$$

$$L_{cyl} = \left(\frac{A_{tree}}{\pi g_L r_L}\right)^{\frac{1}{3}} \left(\frac{< L_e >}{2}\right)^{\frac{2}{3}} \tag{5.5}$$

5.6 Array-embedded neurons and frequency filtering in cortical tissue

In order to make the results of our study applicable for tissue-level systems, we constructed synaptically unconnected neuronal arrays and observed the steady-state and frequency responses of the array embedded neurons. The array had a column height of approximately 100 μm in the applied field direction and infinite extent in directions perpendicular to the field. The number of neurons in the vertical column were altered for different neuronal heights to keep the column height at approximately 100 μm. For array-embedded neurons as well, we see effects mediated by the parallel bulk conductance. In the first instance, we observe a significant increase (by a factor of two) in the magnitude of the induced membrane potential (fig. 4.6), which is caused by the increased extracellular bulk resistance shunting the applied current through the neuronal membrane. Interestingly, this increased field to cell coupling is caused mainly by the cells in the x-y layer, adjacent to the neuron under observation. This is demonstrated by the fact that a significant increase in the V_m amplitude is observed when going from the isolated to the monolayer results, but only a small increase is observed when going from the monolayer to the full array results. This in turn implies that for an array-embedded neuron, it is the presence of the cells in its monolayer, which primarily affects the current flow around the neuron (causing an increase in V_m), with the cells in the other layers having a smaller effect.

We further observe a slight decrease in the drop-off frequency for the array-embedded neuron as compared to the isolated case. This again is in line with our understanding of the role of the extracellular bulk conductance in that it decreases due to the presence of the array cells and hence increases the effective membrane time constant of the array-embedded neuron. A similar argument explains the increase in the amplitude of the subthreshold resonance for array-embedded neurons (fig. 4.7), where an increasing proportion of the applied current is shunted through the resonant neuronal membrane.

Significantly, the relationship elucidated with our previous results, linking the high-frequency response of the cell to its compactness, is preserved for the array-embedded case and hence validated for tissue-embedded neurons.

Finally, the role of the extracellular bulk conductance highlighted above has implications for understanding the propagation of electrical signals within the cortex. Low frequency extracellular potentials, such as LFPs are observed to be much less sensitive to the recording position as compared to extracellular spikes. Furthermore, slow wave potentials exhibit spatial correlation over larger distances in comparison with gamma band potential oscillations or spiking activity [86]. These, as well as the observation that only slow wave potentials and not action potentials are recorded at the scalp surface, have prompted suggestions that the cortical tissue has a biased impedance spectrum, which selectively attenuates higher frequencies. This has lead to the development of models, which achieve high-frequency filtering by modeling the extracellular medium with inhomogeneous conductivities and permittivities [87,88]. Logothetis et al [77] however, have shown that the mammalian cortical impedance spectrum is nearly flat, by direct measurement using a four-electrode system, suggesting a more functional reason for the LFP coherence, making these extracellular signals more interpretable. In light of the concept of the parallel bulk conductance as elucidated by our models, the flat impedance spectrum implies that the cortical extracellular space offers low bulk resistance to current flow, thus implying a short effective time constant for the system. Thus currents from the potential/current sources flow, for the most part, through the extracellular space even at high frequencies. Indeed as our finite-element modeling suggests, the embedding of the neuron into an array has a small effect on the frequency response of its membrane potential.

5.7 Future work

To date, many modeling studies looking at extracellular field effects on neurons, only take into account a one-way coupling between the field and the cell. By solving Maxwell's equations for geometrically extended neurons in two and three dimensions, our modeling incorporates full two-way field coupling between a biophysically realistic neuron and the extracellular electric field. This is an advance in the field and opens up many avenues of investigation, where morphologically realistic neurons can be simulated in realistic inhomogeneous fields.

Thus we aim to develop models of actual neuronal geometries, such as the pyramidal, obtained through various imaging techniques to understand how a time-varying field polarizes the cell. This will require greater computational power, potentially with parallel computation using multinode clusters. The translation of actual neuronal geometries into COMSOL also presents an interesting challenge, which could potentially be met using modifications of COMSOL and existing software, specialized for three-dimensional neuronal modeling, such as neuroConstruct [89].

The finite-element array models presented in this thesis have strong relevance towards the cortical frequency-filtering debate as highlighted above. The array models can be adapted to simulate realistic cortical tissue and essentially model the experimental setup used by Logothetis et al [77] measuring the cortical impedance spectrum.

Another intuitive extension of our array models is to build a network of synaptically connected arrays of spiking neurons using FEM. This will involve simulating synaptic coupling between neurons using the conductance-based description to model the synaptic current on the postsynaptic neuron while linking it to the membrane potential of the presynaptic neuron. As in the case of coupling the bulk extracellular and intracellular electric fields with the membrane dynamics, we propose using the “weak form” boundary interfaces in COMSOL for modeling the synaptic coupling. It should be noted that significantly greater computational power will be required to simulate a realistic neuronal network. We expect that the inclusion of synaptically connected spiking neurons in to the model will profoundly alter the membrane potential dynamics of the system, when the electric field is strong enough to trigger spikes. For subthreshold conditions, we expect the system’s behaviour to be similar to that of the array modeled in this thesis.

Such a model would be a significant step towards understanding how the LFP is produced by the activity of individual neurons and how small coordinated changes in the membrane potentials of individual neurons can lead to a network-wide synchronization of structured neuronal activity [59].

5.8 Summary

In this thesis we set out to model electric field interactions with neurons, utilizing the extracellular cable equation, the finite-difference and the finite-element methodologies. With our models of the cylindrical neurons we have elucidated the relationship between the compactness of the cell and its frequency response to oscillating electric fields; with the compact neurons staying responsive to higher frequency stimulation. Physically, the lack of a high frequency response with the increasing elongation of neurons occurs due to the concomitant increase in the "parallel bulk conductance". We have applied this understanding to previously unexplained discrepancies in the experimental literature and have resolved them. Also using the comparison between the one-dimensional, "no feedback" cable model and the fully field-coupled FEM models we have shown that the cable models significantly underestimate the field coupling for compact neurons.

Using our models for point-source field stimulation, we have discovered the novel phenomena of the "passive resonance", which exhibits strong frequency-preferences in the membrane potential response, in the absence of voltage-gated channels. This phenomenon has not been previously reported in the literature and could have important implications towards understanding field-neuron interactions.

Furthermore, we have simulated quasi-active neurons (exhibiting voltage-gated resonances) in the presence of electric fields and have found that this kind of resonance diminishes for compact neurons. We have provided a physical explanation for this result in terms of the currents primarily flowing through the parallel bulk media for compact neurons. Using our FEM models, we go on further and simulate fully active (Hodgkin Huxley) neurons and show the occurrence of the passive resonance in the spiking neuron model.

Lastly, we simulated array-embedded neurons exposed to electric fields and validated the results above at tissue-level. Our results also demonstrated an increase in the field to cell coupling, a slight decrease in the frequency drop-off point and an increase in the quasi-active resonance occurring due to the presence of the "neighbouring" neurons. The physical explanations for these findings were provided using the parallel bulk conductance framework.

Along with the novel results presented above, the development of a biophysically detailed, three-dimensional, tissue-embedded neuron model in this thesis constitutes a significant step towards understanding interactions between the nervous system and endogenous or artificial electric fields.

Appendix A - Table of consistent units

The transmembrane current equation Eq. 1.13

$$J = -\mathbf{n} \cdot (\sigma_i \nabla V_i) = c_m \frac{\partial}{\partial t} V_m + I_{ion}(V_m) = -\mathbf{n} \cdot (\sigma_e \nabla V_e) \tag{5.6}$$

can be utilized to produce a table of consistent units (table 5.1) given below for the reader's reference.

Table 5.1: Table of consistent units

c_m	V_m	t	g_L	I	σ	x
F/m^2	V	s	S/m^2	A/m^2	S/m	m
nF/mm^2	mV	ms	μS/mm^2	mA/	μS/mm	mm
nF/μm^2	mV	ms	μS/μm^2	nA/μm^2	μS/μm	μm

Appendix B - Comparing the different time constants obtained for the various geometries

In the field-cell system, the applied current passes through the extracellular and the intracellular bulk media, providing for a much shorter effective membrane time constant. We list below (table 5.2) the analytical expressions and the physiological numerical values of these time constants for comparison. The radius used for the infinitely long cylinder, the sphere and the finite cable neuron is $a = 2$ μm, whereas the half-length of the finite cable neuron used is $l = 4$ μm (thus the cable cell is electrotonically compact).

Table 5.2: Algebraic expressions and numerical values of the effective membrane time constants for field-cell systems with different neuronal geometries. The biophysical parameters are those given in table 1.1.

Neuron geometry	Effective membrane time constant	Numerical value
Point-neuron	$\frac{c_m}{g_L}$	10 ms
Infinitely long cylinder	$\frac{c_m}{g_L+\frac{1}{a(\frac{1}{\sigma_e}+\frac{1}{\sigma_i})}}$	2×10^{-4} ms
Sphere	$\frac{c_m}{g_L+\frac{1}{a(\frac{1}{2\sigma_e}+\frac{1}{\sigma_i})}}$	1.5×10^{-4} ms
Finite cable	$\frac{\frac{c_m}{a\sigma_i}}{2l^2}$	8×10^{-4} ms

Appendix C - Derivation of V_m for an infinitely long cylindrical neuron exposed to a uniform sinusoidally oscillating field, oriented perpendicular to its axis

We consider a uniform electric field, E applied transversely to a cylindrical cell with infinite length and radius a. Due to the symmetry, the problem is reduced to two dimensions and can be cast in polar coordinates, r and θ. Using Eqs. 1.11, 1.12 and 1.13 and assuming a passive membrane with $I_{ion} = g_L(V_i - V_e - E_L)$, the boundary value problem in polar coordinates becomes

$$\nabla^2 V_e = 0 \qquad r \geq a \tag{5.7}$$

$$\nabla^2 V_i = 0 \qquad r \leq a \tag{5.8}$$

Along with the boundary conditions

$$V_e(r,\theta) = -Ercos\theta + c \qquad r \to \infty \tag{5.9}$$

$$E = \frac{V_1 - V_2}{2l} \tag{5.10}$$

$$-\sigma_e \frac{\partial}{\partial r} V_e = g_L(V_i - V_e - E_L) \qquad r = a \tag{5.11}$$

$$-\sigma_i \frac{\partial}{\partial r} V_i = g_L(V_i - V_e - E_L) \qquad r = a \tag{5.12}$$

Where $V_1$and V_2 are the potentials on the left and the right boundaries respectively and $2l$ is the distance between them. In order to solve the above boundary value problem we start with the general solution of Laplace's equation in 2-D polars for V_e

$$V_e(r,\theta) = C_o \ln r + D_o + \sum_{n=1}^{\infty}(A_n \cos n\theta + B_n \sin n\theta)(C_n r^n + D_n r^{-n}) \tag{5.13}$$

Applying the boundary condition (Eq. 5.9) we have

$$C_o \ln r + D_o + (\sum_{n=1}^{\infty} A_n \cos n\theta + B_n \sin n\theta)(C_n r^n) = -Er\cos\theta + c \tag{5.14}$$

Using the equation above we make the following observations

$$C_o = 0 \qquad \text{no } \ln r \text{ terms on RHS} \tag{5.15}$$

$$D_o = c \qquad \text{matching the constants} \tag{5.16}$$

$$B_n = 0 \quad \forall n \quad \text{no } \sin\theta \text{ terms due to even symmetry} \tag{5.17}$$

$$A_n C_n = 0 \quad n \geq 2 \quad \text{no } \cos n\theta \text{ terms on RHS for } n \geq 2 \tag{5.18}$$

Thus Eq. 5.14 becomes

$$A_1 C_1 r\cos\theta \;=\; -Er\cos\theta \tag{5.19}$$

$$A_1 C_1 \;=\; -E \tag{5.20}$$

Our general solution (Eq. 5.13) then becomes

$$V_e(r,\theta) = c - Er\cos\theta + \sum_{n=1}^{\infty} \frac{K_n \cos n\theta}{r^n} \tag{5.21}$$

Now we calculate the intracellular potential V_i. We again employ the general solution

$$V_i(r,\theta) = F_o \ln r + G_o + \sum_{n=1}^{\infty} (M_n \cos n\theta + N_n \sin n\theta)(P_n r^n + Q_n r^{-n}) \tag{5.22}$$

Immediately we can see that

$$F_o = 0 \qquad \text{due to consideration of}\, V_i \,\text{at}\, r = 0 \tag{5.23}$$

$$Q_n = 0 \quad \forall n \quad \text{due to consideration of}\, V_i \,\text{at}\, r = 0 \tag{5.24}$$

$$N_n = 0 \quad \forall n \quad \text{no}\, \sin\theta \,\text{due to even symmetry} \tag{5.25}$$

So our solution form becomes

$$V_i(r,\theta) = G_o + \sum_{n=1}^{\infty} S_n r^n \cos n\theta \qquad r \leq a \tag{5.26}$$

Now we apply the equality given by the membrane boundary conditions (Eqs. 5.11and 5.12) at $r = a$ to give

$$\sigma_e \frac{\partial V_e}{\partial r} \quad = \quad \sigma_i \frac{\partial V_i}{\partial r} \tag{5.27}$$

Inserting our solutions for V_e and V_i (5.21 and 5.26 respectively) in to Eq. 5.27 we get

$$\mu \left(-E\cos\theta + \sum_{n=1}^{\infty} -nK_n \cos n\theta a^{-(n+1)} \right) = \sum_{n=1}^{\infty} nS_n \cos n\theta a^{n-1} \tag{5.28}$$

where $\mu = \frac{\sigma_e}{\sigma_i}$. Rearranging Eq. 5.28

$$-\mu E \cos\theta = \sum_{n=1}^{\infty} \left(\mu K_n a^{-(n+1)} + S_n a^{n-1} \right) n \cos n\theta \tag{5.29}$$

The above equation implies that

$$\mu K_n a^{-(n+1)} + S_n a^{n-1} = 0 \qquad n \geq 2 \qquad \text{no } \cos n\theta \text{ terms for } n \geq 2 \tag{5.30}$$

$$\Rightarrow \quad S_n = \tfrac{-\mu K_n}{a^{2n}} \quad n \geq 2 \tag{5.31}$$

The above Eq. 5.29 thus becomes

$$-\mu \left(E + \frac{K_1}{a^2} \right) = S_1 \tag{5.32}$$

So our solution form for V_i (Eq. 5.26) becomes

$$V_i(r, \theta) = G_o - \mu \left(E + \frac{K_1}{a^2} \right) r \cos\theta + \sum_{n=2}^{\infty} \frac{-\mu K_n r^n \cos n\theta}{a^{2n}} \qquad r \leq a \tag{5.33}$$

In order to complete our solution, we now need to determine K_n and G_o. We utilize the membrane boundary condition at $r = a$ (Eq. 5.11)

$$-\sigma_e \tfrac{\partial V_e}{\partial r} = g_L(V_i - V_e - E_L) \tag{5.34}$$

$$\text{or} \quad -\sigma_e \left(-E\cos\theta + \textstyle\sum_{n=1}^{\infty} - \frac{nK_n \cos n\theta}{a^{(n+1)}} \right) = g_L \left(G_o - \mu(E + \tfrac{K_1}{a^2}) a \cos\theta \right. \tag{5.35}$$

$$\left. + \textstyle\sum_{n=2}^{\infty} \frac{-\mu K_n a^n \cos n\theta}{a^{2n}} - c + Eacos\theta - \sum_{n=1}^{\infty} \frac{K_n \cos n\theta}{a^n} - E_L \right)$$

We immediately see from the above equation that

$$G_o = c + E_L \tag{5.36}$$

We rearrange Eq. 5.35, joining together the two sums running from $n = 1$ to ∞ and separating out the $n = 1$ term from the resultant sum to give

$$\begin{aligned}\left(\sigma_e E - g_L a E + g_L \mu (E + \tfrac{K_1}{a^2}) a\right) \cos\theta = -K_1 \left(\tfrac{\sigma_e}{a^2} + \tfrac{g_L}{a}\right) \cos\theta \\ - \textstyle\sum_{n=2}^{\infty} K_n \left(\tfrac{\sigma_e n}{a^{n+1}} + \tfrac{g_L}{a^n} + \tfrac{\mu g_L}{a^n}\right) \cos n\theta\end{aligned} \tag{5.37}$$

We observe from the above equation that

$$K_n = 0 \qquad\qquad n \geq 2 \tag{5.38}$$

$$\text{and} \quad K_1 = \tfrac{-E a^2 (\sigma_e + g_L a(\mu - 1))}{\sigma_e + g_L a(1 + \mu)} \tag{5.39}$$

Thus we have our potentials as

$$V_e(r, \theta) = c + \left(-Er + \frac{K_1}{r}\right) \cos\theta \qquad r \geq a \tag{5.40}$$

$$V_i(r, \theta) = c + E_L - \mu \left(E + \frac{K_1}{a^2}\right) r \cos\theta \qquad r \leq a \tag{5.41}$$

Now in order to determine c, we utilize the boundary condition Eq. 5.10, which implies that

$$V_e = V_o = \frac{V_1 + V_2}{2} \quad y \to \infty \quad x = 0 \tag{5.42}$$

$$\text{or} \quad c = V_o \tag{5.43}$$

Thus we have our potentials as

$$V_e(r, \theta) = V_o + \left(-Er + \frac{K_1}{r}\right) \cos\theta \qquad r \geq a \tag{5.44}$$

$$V_i(r, \theta) = V_o + E_L - \mu \left(E + \frac{K_1}{a^2}\right) r \cos\theta \qquad r \leq a \tag{5.45}$$

Substituting for K_1 at $r = a$, we obtain

$$V_m = V_i - V_e = E_L + \frac{2\sigma_e E a \cos\theta}{\sigma_e + g_L a(1+\mu)} \qquad r = a \tag{5.46}$$

The time-dependent solution for a passive membrane can be obtained through the mapping $g_L \to \hat{g}_L = g_L + i\omega c_m$

$$V_m = E_L + \frac{2\sigma_e E a \cos\theta}{\sigma_e + (g_L + i\omega c_m) a(1+\mu)} \tag{5.47}$$

Lastly, the time-dependent quasi-active solution can be obtained through the mapping in Eq. 4.10

$$V_m = E_L + \frac{2\sigma_e E a \cos\theta}{\sigma_e + \left(g_T + i\omega c_m + \frac{\kappa}{1+i\omega\tau_n}\right) a(1+\mu)} \tag{5.48}$$

Appendix D - Derivation of V_m for a spherical neuron exposed to a uniform sinusoidally oscillating field

Using spherical-polar coordinates, we consider a uniform electric field applied in the axial or z direction with a spherical cell positioned at $r = 0$ with radius $r = a$. Using Eqs. 1.11, 1.12 and 1.13 and assuming a passive membrane with $I_{ion} = g_L(V_i - V_e - E_L)$, the boundary value problem in spherical coordinates becomes

$$\nabla^2 V_e = 0 \qquad r \geq a \tag{5.49}$$

$$\nabla^2 V_i = 0 \qquad r \leq a \tag{5.50}$$

Along with the boundary conditions

$$V_e(r,\theta) = -Ercos\theta + c \qquad r \to \infty \tag{5.51}$$

$$E = \frac{V_1 - V_2}{2l} \tag{5.52}$$

$$-\sigma_e \frac{\partial}{\partial r} V_e = g_L(V_i - V_e - E_L) \qquad r = a \tag{5.53}$$

$$-\sigma_i \frac{\partial}{\partial r} V_i = g_L(V_i - V_e - E_L) \qquad r = a \tag{5.54}$$

Where V_1 and V_2 are the potentials on the top and bottom boundaries respectively and $2l$ is the distance between them. We set $c = 0$ by requiring that $V_1 = -V_2$.

Incorporating the inherent axial symmetry and assuming finite solutions on the z-axis, we start with the general solution of Laplace's equation in spherical polars for V_e and V_i

$$V_e(r,\theta,\phi) = \sum_{l=0}^{\infty} \left(\left(A_l r^l + \frac{B_l}{r^{l+1}} \right) P_l(\cos\theta) \right) \qquad r \geq a \tag{5.55}$$

$$V_i(r,\theta,\phi) = \sum_{l=0}^{\infty} C_l r^l P_l(\cos\theta) \qquad r \leq a \tag{5.56}$$

where the $\frac{1}{r^{l+1}}$ coefficient has been set to zero for V_i due to the $r = 0$ consideration. P_l are the Legendre polynomials given by

$$P_l(x) = \frac{1}{2^l l!} \left(\frac{d}{dx} \right)^l (x^2 - 1)^l \tag{5.57}$$

The first few Legendre polynomials are

$$P_o(x) = 1 \tag{5.58}$$

$$P_1(x) = x \tag{5.59}$$

$$P_2(x) = \tfrac{3x^2-1}{2} \tag{5.60}$$

$$P_3(x) = \tfrac{5x^3-3x}{2} \tag{5.61}$$

Applying the boundary condition in Eq. 5.51, we have

$$\textstyle\sum_{l=0}^{\infty} A_l r^l P_l(\cos\theta) = -Er\cos\theta \tag{5.62}$$

$$\Rightarrow \qquad A_o = 0 \qquad \text{matching the constants} \tag{5.63}$$

$$\Rightarrow \qquad A_1 = -E \qquad \text{matching } \cos\theta \text{ terms} \tag{5.64}$$

$$\Rightarrow \qquad A_n = 0 \qquad n \geq 2 \tag{5.65}$$

Thus our extracellular potential becomes

$$V_e(r,\theta,\phi) = -Er\cos\theta + \sum_{l=0}^{\infty} \frac{B_l}{r^{l+1}} P_l(\cos\theta) \qquad r \geq a \tag{5.66}$$

Applying the equality $\sigma_e \frac{\partial V_e}{\partial r} = \sigma_i \frac{\partial V_i}{\partial r}$ given by boundary conditions in Eqs. 5.53 and 5.54 at $r = a$, we obtain

$$\mu\left(-E\cos\theta \textstyle\sum_{l=0}^{\infty} -(l+1)\frac{B_l}{a^{l+2}} P_l(\cos\theta)\right) = \textstyle\sum_{l=0}^{\infty} l C_l a^{l-1} P_l(\cos\theta) \tag{5.67}$$

$$\Rightarrow \qquad B_o = 0 \tag{5.68}$$

$$\Rightarrow \qquad C_1 = -\mu\left(E + 2\tfrac{B_1}{a^3}\right) \tag{5.69}$$

$$\Rightarrow \qquad C_l = \tfrac{-\mu(l+1)B_l}{l a^{2l+1}} \tag{5.70}$$

Thus our intracellular potential becomes

$$V_i(r,\theta,\phi) = C_o - \mu\left(E + \tfrac{2B_1}{a^3}\right) r\cos\theta - \textstyle\sum_{l=2}^{\infty} \tfrac{-\mu(l+1)B_l}{l a^{2l+1}} r^l P_l(\cos\theta) \tag{5.71}$$

for $r \leq a$. Applying the boundary condition in Eq. 5.53 at $r = a$, we obtain

$$\begin{aligned} -\sigma_e \left(-E\cos\theta \textstyle\sum_{l=1}^{\infty} -(l+1)\frac{B_l}{a^{l+2}} P_l(\cos\theta) \right) &= g_L \left(C_o - \mu \left(E + \tfrac{2B_1}{a^3} \right) a\cos\theta \right. \\ &\left. - \textstyle\sum_{l=2}^{\infty} \frac{-\mu(l+1)B_l}{la^{l+1}} P_l(\cos\theta) + Ea\cos\theta - \sum_{l=1}^{\infty} \frac{B_l}{a^{l+1}} P_l(\cos\theta) - E_L \right) && (5.72) \\ \Rightarrow \qquad C_o &= E_L && (5.73) \\ \Rightarrow \qquad B_1 &= \tfrac{(-\sigma_e E + g_L Ea(1-\mu))a^3}{2\sigma_e + g_L a(1+2\mu)} && (5.74) \\ \Rightarrow \qquad B_l &= 0 && (5.75) \end{aligned}$$

Thus in terms of B_1 we have our potential solutions as

$$V_e(r,\theta) = -Er\cos\theta + \frac{B_1}{r^2}\cos\theta \qquad r \geq a \tag{5.76}$$

$$V_i(r,\theta) = E_L - \mu(E + \frac{2B_1}{a^3})r\cos\theta \qquad r \leq a \tag{5.77}$$

The membrane potential $V_m = V_i - V_e$ at $r = a$ is thus given by

$$V_m = E_L + \frac{3\sigma_e Ea\cos\theta}{2\sigma_e + (1+2\mu)g_L a} \qquad r = a \tag{5.78}$$

The time-dependent solution for a passive membrane can be obtained through the mapping $g_L \to g_L + i\omega c_m$

$$V_m = E_L + \frac{3\sigma_e Ea\cos\theta}{2\sigma_e + (1+2\mu)(g_L + i\omega c_m)a} \tag{5.79}$$

Lastly, the time-dependent quasi-active solution can be obtained through the mapping in Eq. 4.10

$$V_m = E_L + \frac{3\sigma_e Ea\cos\theta}{2\sigma_e + (1+2\mu)\left(g_T + i\omega c_m + \frac{\kappa}{1+i\omega\tau_n}\right)a} \tag{5.80}$$

Appendix E - Matlab code for time-dependent finite-difference simulation of a cylindrical neuron in field

```
% MULTISCALE SIMULATION FOR A CYLINDRICAL CELL IN FIELD

function [xmT,VmT,xmS,VmS]=CYLscalintimedep(dxi,L,pi,zi)
E=1; %mV/um   field strength
Vo=E*L; %mV   boundary potential
sigmaE=0.2; %uS/um  extracellular resistivity
sigmaI=0.2; %uS/um  intracellular resistivity

GL=1e-6;    %uS/um^2  membrane leak conductance per unit area
C=1e-5;     %nF/um^2  membrane capacitance per unit area

fHz=1E1; %kHz  field frequency
omega=2*3.1416*fHz; %angular field frequency
gL=GL+1i*omega*C;   %complex membrane conductance
%%%%%%%%%%%%%%%%%%%%%%%%%%%%%%%%%%%%%%%%%%%%%%%%%%%%%%%%%%%%%%%%%%%%%
n=ceil(L/dxi)+1;  dx=L/(n-1);
sz=ceil(zi/dx); sp=ceil(pi/dx); %half width/height of cell
z=(sz-1)*dx; p=(sp-0.5)*dx; %defining coordinates

Ve=ones(n,n); Vi=ones(n,n); %e/i.cellular potentials
for k=1:n
   Ve(k,:)=linspace(0,-Vo,n); %fixes the top and right bcs
end
Vi(1:n,1:n)=EL;
%%%%%%%%%%%%%%%%%%%%%%%%%%%%%%%%%%%%%%%%%%%%%%%%%%%%%%%%%%%%%%%%%%%%%
[Vcoarse1,n,dx,dX1,sz,Sz,sp,Sp,Ve,Vi,xmT1,VmT1,xmS1,VmS1,ITT1,...
    VML1,VL1]=aniter(Ve,Vi,n,dx,sp,sz,1E-8,sigmaE,sigmaI,gL);
subplot(2,2,1); plot(xmT1,VmT1);
subplot(2,2,2); plot(xmS1,VmS1); drawnow;
%%%%%%%%%%%%%%%%%%%%%%%%%%%%%%%%%%%%%%%%%%%%%%%%%%%%%%%%%%%%%%%%%%%%%
```

```
[Vcoarse2,n,dx,dX2,sz,Sz,sp,Sp,Ve,Vi,xmT2,VmT2,xmS2,VmS2,ITT2,...
    VML2,VL2]=aniter(Ve,Vi,n,dx,sp,sz,1E-8,sigmaE,sigmaI,gL);
subplot(2,2,1); plot(xmT1,VmT1,xmT2,VmT2);
subplot(2,2,2); plot(xmS1,VmS1,xmS2,VmS2); drawnow;
%%%%%%%%%%%%%%%%%%%%%%%%%%%%%%%%%%%%%%%%%%%%%%%%%%%%%%%%%%%%%%%%%%%%%%
%%%%%%%%%%%%%%%%%%%%%%%%%%%%%%%%%%%%%%%%%%%%%%%%%%%%%%%%%%%%%%%%%%%%%%
%%%%%%%%%%%%%%%%%%%%%%%%%%%%%%%%%%%%%%%%%%%%%%%%%%%%%%%%%%%%%%%%%%%%%%
[Vcoarse3,n,dx,dX3,sz,Sz,sp,Sp,Ve,Vi,xmT3,VmT3,xmS3,VmS3,ITT3,...
    VML3,VL3]=aniter(Ve,Vi,n,dx,sp,sz,1E-7,sigmaE,sigmaI,gL);
z=(Sz-1)*dX3; p=(Sp-0.5)*dX3;
subplot(3,2,1); plot(xmT1,VmT1,xmT2,VmT2,xmT3,VmT3);title('VmS');
subplot(3,2,2); plot(xmS1,VmS1,xmS2,VmS2,xmS3,VmS3);title('VmT');
subplot(3,2,3); semilogx(ITT1,VML1);
title('1st convergence'); xlabel('itt');ylabel('Vmax');
subplot(3,2,4); semilogx(ITT2,VML2);
title('2nd convergence'); xlabel('itt');ylabel('Vmax');
subplot(3,2,5); semilogx(ITT3,VML3);
title('3rd convergence'); xlabel('itt');ylabel('Vmax');
save VL3;
subplot(3,2,6); plot ([dX1,dX2,dX3], [VL1,VL2,VL3]);
xlabel('dx'); ylabel('VL');
title(['dx =',num2str(dX3),'um, E = ',num2str(E),'mV/um, Vo = '...
    ,num2str(Vo), 'mV , L = ',num2str(L),' um, z = ',num2str(z),...
    ' um, p = ',num2str(p),'um'],'Fontsize',8);
saveas (gcf, 'VMCYLconvprofile');


function [Vcoarse,n,dx,dX,sz,Sz,sp,Sp,Ve,Vi,xmT,VmT,xmS,VmS,ITT,...
    VML,VL]=aniter(Ve,Vi,n,dx,sp,sz,maxerror,sigmaE,sigmaI,gL)
%Relaxation
maxr=1;
itt=0;
while maxr>maxerror

Velast(1:n, 1:n) = Ve(1:n, 1:n); %Save the last guess
```

```
Vilast(1:n, 1:n) = Vi(1:n, 1:n); %Save the last guess

%Boundary conditions
Vi(1:sp,1)=0; %Left side due to symmetry
Ve(sp:n-1,1)=0;

Vi(1,2:sz-1)=(1/3)*(Vi(2,2:sz-1) + Vi(1,1:sz-2) +...
    Vi(1,3:sz)); %Bottom no leakage
Ve(1,sz+1:n-1)=(1/3)*(Ve(2,sz+1:n-1) + Ve(1,sz:n-2) + Ve(1,sz+2:n));

%Bulk equations
for i=sp+1:n-1
Ve(i,2:n-1)= 1/4 *( Ve(i,3:n)+Ve(i,1:n-2)+((2*i)/(2*i-1))*...
    Ve(i+1,2:n-1)+((2*i-2)/(2*i-1))*Ve(i-1,2:n-1) );
end
for i=2:sp
Ve(i,sz+1:n-1)= 1/4*( Ve(i,sz+2:n)+Ve(i,sz:n-2) + ((2*i)/(2*i-1))...
    *Ve(i+1,sz+1:n-1)+((2*i-2)/(2*i-1))*Ve(i-1,sz+1:n-1) );
end
for i=2:sp-1
Vi(i,2:sz-1)= 1/4*( Vi(i, 3:sz)+Vi(i,1:sz-2)+((2*i)/(2*i-1))...
    *Vi(i+1,2:sz-1)+((2*i-2)/(2*i-1))*Vi(i-1,2:sz-1) );
end
%%%%%%%%%%%%%%%%%%%%%%%%%%%%%%%%%%%%%%%%%%%%%%%%%%%%%%%%%%%%%%%%%%%%

%Bottom membrane point
Vi(1,sz)=((sigmaI/dx)*(Vi(1,sz-1)+Vi(2,sz) )*(2*sigmaE/dx+gL) +...
    gL*(sigmaE/dx)*(Ve(1,sz+1)+Ve(2,sz)) )/((2*sigmaI/dx+gL)*...
    (2*sigmaE/dx+gL)-gL^2);
Ve(1,sz)=((sigmaE/dx)*(Ve(1,sz+1)+Ve(2,sz) )*(2*sigmaI/dx+gL) +...
    gL*(sigmaI/dx)*(Vi(1,sz-1)+Vi(2,sz)) )/((2*sigmaI/dx+gL)*...
    (2*sigmaE/dx+gL)-gL^2);
%Corner membrane point
Vi(sp,sz)=((sigmaI/dx)*(Vi(sp,sz-1)+Vi(sp-1,sz) )*(4*sigmaE/dx+gL)...
    +gL*(sigmaE/dx)*(Ve(sp+1,sz)+Ve(sp-1,sz)+Ve(sp,sz-1)+...
```

```
    Ve(sp,sz+1)) )/((2*sigmaI/dx+gL)*(4*sigmaE/dx+gL)-gL^2);
Ve(sp,sz)=((sigmaE/dx)*(Ve(sp+1,sz)+Ve(sp-1,sz)+Ve(sp,sz-1)+...
    Ve(sp,sz+1))*(2*sigmaI/dx+gL) + gL*(sigmaI/dx)*(Vi(sp,sz-1)+...
    Vi(sp-1,sz)) )/((2*sigmaI/dx+gL)*(4*sigmaE/dx+gL)-gL^2);
%Right membrane points
Vi(2:sp-1,sz)= ((sigmaI/dx)*(Vi(2:sp-1,sz-1)+Vi(3:sp,sz)+...
    Vi(1:sp-2,sz) )*(3*sigmaE/dx+gL) + gL*(sigmaE/dx)*(Ve(3:sp,sz)...
    +Ve(2:sp-1,sz+1)+Ve(1:sp-2,sz)) )/((3*sigmaI/dx+gL)*...
    (3*sigmaE/dx+gL)-gL^2);
Ve(2:sp-1,sz)= ((sigmaE/dx)*(Ve(3:sp,sz)+Ve(2:sp-1,sz+1)+...
    Ve(1:sp-2,sz) )*(3*sigmaI/dx+gL) + gL*(sigmaI/dx)*...
    (Vi(2:sp-1,sz-1)+Vi(3:sp,sz)+Vi(1:sp-2,sz)) ) /((3*sigmaI/dx+gL)...
    *(3*sigmaE/dx+gL)-gL^2);
%Top membrane points
Vi(sp, 2:sz-1)= ((sigmaI/dx)*(Vi(sp-1, 2:sz-1)+Vi(sp, 3:sz)+...
    Vi(sp, 1:sz-2) )*(3*sigmaE/dx+gL) + gL*(sigmaE/dx)*...
    (Ve(sp, 3:sz)+Ve(sp+1, 2:sz-1)+Ve(sp, 1:sz-2)) ) /...
    ((3*sigmaI/dx+gL)*(3*sigmaE/dx+gL)-gL^2);
Ve(sp, 2:sz-1)= ((sigmaE/dx)*(Ve(sp, 3:sz)+Ve(sp+1, 2:sz-1)+...
    Ve(sp, 1:sz-2) )*(3*sigmaI/dx+gL) + gL*(sigmaI/dx)*...
    (Vi(sp-1, 2:sz-1)+Vi(sp, 3:sz)+Vi(sp, 1:sz-2)) ) /...
    ((3*sigmaI/dx+gL)*(3*sigmaE/dx+gL)-gL^2);

%Error
errore(1:n, 1:n) = abs(Ve(1:n, 1:n)-Velast(1:n, 1:n));
errori(1:n, 1:n) = abs(Vi(1:n, 1:n)-Vilast(1:n, 1:n));
maxre=(max(max(errore))); maxri=(max(max(errori)));
maxr=(max(max(maxre,maxri)));
itt=itt+1;
%Convergence plot
Vml= (Vi(1,sz)-Ve(1,sz)); VML(itt)=Vml;
end

VL=Vi(1,sz)-Ve(1,sz);

```

```
ITT = linspace(1,itt,itt);
plot(ITT,VML);title('Fine convergence');
xlabel('iteration');ylabel('Vml');drawnow;

%%%%%%%%%%%%%%%%%%%%%%%%%%%%%%%%%%%%%%%%%%%%%%%%%%%%%%%%%%%%%%%%%%%%%%%%
%Vm spatial profile
xmT=((0:sz-1)*dx)'; VmT=(Vi(sp,1:sz)-Ve(sp,1:sz))'; %top of the cell
xmS=(((1:sp)-0.5)*dx)'; VmS=Vi(1:sp,sz)-Ve(1:sp,sz); %side of cell
Vcoarse(1:n, 1:n)=Ve(1:n, 1:n); Vcoarse(1:sp, 1:sz)= Vi(1:sp, 1:sz);
Vecoarse=Ve; Vicoarse=Vi;
N=n; dX=dx; Sz=sz; Sp=sp;
%%%%%%%%%%%%%%%%%%%%%%%%%%%%%%%%%%%%%%%%%%%%%%%%%%%%%%%%%%%%%%%%%%%%%%%%
[n,dx,sz,sp,Ve,Vi]=gridtransp(N,dX,Sz,Sp,Vecoarse,Vicoarse);


function[n,dx,sz,sp,Ve,Vi]=gridtransp(N,dX,Sz,Sp,Vecoarse,Vicoarse)
%Setting up the finer grid
n=2*N-1; dx=dX/2; sz=2*Sz-1; sp=2*Sp-1;%half width and height of cell
Ve=ones(n,n); Vi=ones(n,n);

Ve(1:2:n,1:2:n)=Vecoarse(1:N,1:N);
Vi(1:2:n,1:2:n)=Vicoarse(1:N,1:N); %original grid points

%odd horizontal strips
Ve(1:2:n, 2:2:n-1) = 0.5*(Vecoarse(1:N,1:N-1)+ Vecoarse(1:N,2:N));
Vi(1:2:n, 2:2:n-1) = 0.5*(Vicoarse(1:N,1:N-1)+ Vicoarse(1:N,2:N));

Ve(2:2:n-1, 2:2:n-1) = 0.25*( Vecoarse(1:N-1,1:N-1)...
    +Vecoarse(1:N-1,2:N)+ Vecoarse(2:N, 1:N-1)+...
    Vecoarse(2:N, 2:N)); %midpoints
Vi(2:2:n-1, 2:2:n-1) = 0.25*( Vicoarse(1:N-1,1:N-1)...
    +Vicoarse(1:N-1,2:N)+ Vicoarse(2:N, 1:N-1)+Vecoarse(2:N, 2:N));

%odd vertical strips
Ve(2:2:n-1, 1:2:n) = 0.5*( Vecoarse(1:N-1,1:N) + Vecoarse(2:N,1:N) );
```

```
Vi(2:2:n−1, 1:2:n) = 0.5*( Vicoarse(1:N−1,1:N) + Vicoarse(2:N,1:N) );

%setting non−evolving extracellular potentials to zero for simplicity
Ve(1:sp−1,1:sz−1)=0;
```

Bibliography

[1] Waxman, S. G. (1972). Regional differentiation of the axon: a review with special reference to the concept of the multiplex neuron. Brain research, 47, 269-88.

[2] Gray, E. G. (1959). Axo-somatic and axo-dendritic synapses in the cerebral cortex: an electron microscope study. Journal of Anatomy, 93, 420-433.

[3] Eccles, J. C. (1961). Inhibitory pathways to motoneurons. In E. Florey (Ed.), Nervous Inhibition, Pergamon, New York, 47–60.

[4] Gray, E. G. (1962). A Morphological Basis for Pre-synaptic Inhibition? Nature, 193, 82-83.

[5] Pinault, D., Smith, Y., & Deschênes, M. (1997). Dendrodendritic and axoaxonic synapses in the thalamic reticular nucleus of the adult rat. The Journal of neuroscience : the official journal of the Society for Neuroscience, 17(9), 3215-33.

[6] Walberg, F. (1965). Axoaxonic contacts basis for in the presynaptic Cuneate Nucleus, probable depolarization. Experimental Neurology, 231, 218-231.

[7] Scott, A. C. (1976). The electrophysics of a nerve fiber. Journal of Biological Physics, 4, 166-191.

[8] McCulloch, W., & Pitts, W. (1943). A logical calculus of the ideas immanent in nervous system. Bulletin of mathematical Biophysics, 5, 115–133.

[9] Stuart, G. J., & Sakmann, B. (1994). Active propagation of somatic action potentials into neocortical pyramidal cell dendrites. Nature, 367(6458), 69-72.

[10] Magee, J. C., & Johnston, D. (1995). Characterization of single voltage-gated Na+ and Ca2+ channels in apical dendrites of rat CA1 pyramidal neurons. The Journal of physiology, 487.1, 67-90.

[11] Stuart, G., Spruston, N., Sakmann, B., & Häusser, M. (1997). Action potential initiation and backpropagation in neurons of the mammalian CNS. Trends in neurosciences, 20, 125-31.

[12] Hausser, M. (2000). Diversity and Dynamics of Dendritic Signaling. Science, 290, 739-744.

[13] Debanne, D. (2004). Information processing in the axon. Nature reviews. Neuroscience, 5, 304-16.

[14] Koch, C., & Segev, I. (2000). The role of single neurons in information processing. Nature neuroscience, 3 Suppl, 1171-7.

[15] London, M., & Häusser, M. (2005). Dendritic computation. Annual review of neuroscience, 28, 503-32.

[16] Sidiropoulou, K., Pissadaki, E. K., & Poirazi, P. (2006). Inside the brain of a neuron. EMBO reports, 7(9), 886-92.

[17] Keener, J. P., & Sneyd, J. (1998). Mathematical Physiology (p. 766). Springer.

[18] Hodgkin, A. L., & Huxley, A. F. (1952). A quantitative description of membrane current and its application to conduction and excitation in nerve. Journal of Physiology, 117, 500-544.

[19] Rall, W. (1959). Branching dendritic trees and motoneuron membrane resistivity. Experimental neurology, 1, 491-527.

[20] Katz, B., and O. H. Schmitt. 1940. Electric interaction between two adjacent nerve fibres. J. Physiol. 97:471-488.

[21] Kocsis, J. D., J. A. Ruiz and K. L. Cummins. 1982. Modulation of axonal excitability mediated by surround electrical activity: an intra axonal study. Exp. Brain Res. 47:151-153.

[22] Jefferys, J. G. (1995). Nonsynaptic modulation of neuronal activity in the brain: electric currents and extracellular ions. Physiological reviews, 75(4), 689-723.

[23] Bokil, H., Laaris, N., Blinder, K. J., Ennis, M., & Keller, A. (2001). Ephaptic interactions in the mammalian olfactory system. The Journal of neuroscience, 21, RC173.

[24] Blinder, K. J., Pumplin, D. W., Paul, D. L., & Keller, A. (2003). Intercellular interactions in the mammalian olfactory nerve. Journal of Comparative Neurology, 466(2), 230-239.

[25] Furkawa, T. and E. J. Furshpan. 1963. Two inhibitory mechanisms in the Mauthner neurons of goldfish. J. NeuroPhys. 26:140-176.

[26] Korn, H. and H. Axelrad. 1980. Electrical inhibition of Purkinje cells in the cerebellum of the rat. Proc. Natl. Acad. Sci. USA. 77:6244-6247.

[27] Jefferys, J. G. R. and H. L. Haas. 1982. Synchronized bursting of CA1 hippocampal pyramidal cells in the absence of synaptic transmission. Nature. 300:448-450.

[28] Taylor, C. P. and F. E. Dudek. 1982. Synchronous neural afterdischarges in rat hippocampal slices without active chemical synapses. Science. 218:810-812.

[29] Snow, R. W. and F.E. Dudek. 1984. Electrical fields directly contribute to action potential sunchronization during convulsant-induced epileptiform bursts. Brain Res. 323:114-118.

[30] Snow, R. W. and F.E. Dudek. 1986. Evidence for neuronal interactions by electric field effects in the CA3 and dentate regions of rat hippocampal slices. Brain Res. 367(1-2):292-295.

[31] Jiruska, P., J. Csicsvari, A. D. Powell, J. E. Fox, W. Chang, M. Vreugdenhil, X. Li, M. Palus, A. F. Bujan, R. W. Dearden and J. G. R. Jefferys. High frequency network activity, global increase in network activity and synchrony expansion precede epileptic seizures in vitro. 2010. J. Neurosci. 30(16):5690-5701.

[32] Kamermans, M., & Fahrenfort, I. (2004). Ephaptic interactions within a chemical synapse: hemichannel-mediated ephaptic inhibition in the retina. Current opinion in neurobiology, 14(5), 531-41.

[33] Jefferys, J. G. R. 1981. Influence of electric fields on the excitability of granule cells in guinea-pig hippocampal slices. J. Physiol. 319: 143-152.

[34] Jefferys, J. G. R., J. Deans, M. Bikson and J. Fox. 2003. Effects of weak electric fields on the activity of neurons and neuronal networks. Radiat. Prot. Dosim. 106(4):321-323.

[35] Bikson, M., M. Inoue, H. Akiyama, J. K. Deans, J. E. Fox, H. Miyakawa and J. G. R. Jefferys. 2004. Effects of uniform extracellular DC electric fields on excitability in rat hippocampal slices in vitro. J. Physiol. 557.1:175-190.

[36] Deans, J. K., A. D. Powell, J. G. R. Jefferys. 2007. Sensitivity of coherent oscillations in rat hippocampus to AC electric fields. J. Physiol. 583.2:555-565.

[37] Benabid, A. L., P. Pollak, C. Gervason, D. Hoffmann, D. M. Gao, M. Hommel, J. E. Perret, J. D. Rougemont. 1991. Long-term suppression of tremor by chronic stimulation of the ventral intermediate thalamic nucleus. Lancet. 337:403-406.

[38] Limousin, P., P. Pollak, A. Benazzouz, D. Hoffmann, B. Jean-Francois, E. Broussol, J. E. Perret and A. L. Benabid. 1995. Effect of Parkinsonian signs and symptoms of bilateral subthalamic nucleus stimulation. Lancet. 345:91-95.

[39] The Deep-Brain Stimulation for Parkinson's Disease Study Group. 2001. Deep-brain stimulation of the subthalamic nucleus or the pars interna of the globus pallidus in Parkinson's disease. N. Engl. J. Med. 345:956-963.

[40] Mayberg, H. S., A. M. Lozano, V. Voon, H. E. McNeely, D. Seminowicz, C. Hamani, J. M. Schwalb and S. H. Kennedy. 2005. Deep brain stimulation for treatment-resistant depression. Neuron 45:651–660.

[41] Larson, P. S. 2008. Deep Brain Stimulation for Psychiatric Disorders. Neurotherapeutics. 5(1):50-8.

[42] Voronin, L. L., Volgushev, M., Sokolov, M., Kasyanov, a, Chistiakova, M., & Reymann, K. G. (1999). Evidence for an ephaptic feed-

back in cortical synapses: postsynaptic hyperpolarization alters the number of response failures and quantal content. Neuroscience, 92(2), 399-405.

[43] Berretta, N., Rossokhin, a V., Kasyanov, a M., Sokolov, M. V., Cherubini, E., & Voronin, L. L. (2000). Postsynaptic hyperpolarization increases the strength of AMPA-mediated synaptic transmission at large synapses between mossy fibers and CA3 pyramidal cells. Neuropharmacology, 39(12), 2288-301.

[44] Kasyanov, A. M., Maximov, V. V., Byzov, A. L., Berretta, N., Sokolov, M. V., Gasparini, S., et al. (2000). Differences in amplitude-voltage relations between minimal and composite mossy fiber responses of rat CA3 hippocampal neurons support the existence of intrasynaptic ephaptic feedback in large synapses. Neuroscience, 101(2), 323-36.

[45] Bennett, M. V. L., & Zukin, R. S. (2004). Electrical coupling and neuronal synchronization in the mammalian brain. Neuron, 41, 495-511.

[46] Schwan, H. P. 1983. Biophysics of the interaction of electromagnetic energy with cells and membranes. In Biological Effects and Dosimetry of Nonionizing Radiation. M. Grandolfo, S. M. Michaelson, and A. Rindl, editors. Plenum Press, New York. 213- 231.

[47] Grosse, C. and H. P. Schwan. 1992. Cellular membrane potentials induced by alternating fields. Biophys. J. 63:1632-1642.

[48] Schwan, H. P. 1957. Electrical properties of tissue and cell suspensions. Adv. Biol. Med. Phys. 5:147-209.

[49] Kotnik, T. and D. Miklavcic. 2000. Analytical description of transmembrane voltage induced by electric fields on spheroidal cells. Biophys. J. 79:670-679.

[50] Gimsa, J. and D. Wachner. 1999. A polarization model overcoming the geometric restrictions of the Laplace solution for spheroidal cells: obtaining new equations for field-induced forces and transmembrane potential. Biophys. J. 77:1316-1326.

[51] Gimsa, J. and D. Wachner. 2001. On the analytical description of transmembrane voltage induced on spheroidal cells with zero membrane conductance. Eur. Biophys. J. 30:463-466.

[52] Gimsa, J. and D. Wachner. 2001. Analytical description of the transmembrane voltage induced on arbitrarily oriented ellipsoidal and cylindrical cells. Biophys. J. 81:1888-1896.

[53] Maswiwat, K., D. Wachner, R. Warnke and J. Gimsa. 2007. Simplified equations for the transmembrane potential induced in ellipsoidal cells of rotational symmetry. J. Phys. D: Appl. Phys. 40:914-923.

[54] Maswiwat, K., D. Wachner and J. Gimsa. 2008. Effects of cell orientation and electric field frequency on the transmembrane potential induced in ellipsoidal cells. Bioelectrochem. 74:130-141.

[55] Marszalek, P., D. Liu and T. Y. Tsong. 1990. Schwan equation and transmembrane potential induced by alternating electric field. Biophys. J. 58:1053-1058.

[56] Tranchina, D., & Nicholson, C. (1986). A model for the polarization of neurons by extrinsically applied electric fields. Biophysical journal, 50, 1139-56.

[57] Anastassiou, C. A., Perin, R., Markram, H., & Koch, C. (2011). Ephaptic coupling of cortical neurons. Nature neuroscience, 14:217-23.

[58] Pettersen, K. H., & Einevoll, G. T. (2008). Amplitude variability and extracellular low-pass filtering of neuronal spikes. Biophysical journal, 94, 784-802

[59] Frohlich, F. and D. A. McCormick. 2010. Endogenous electric fields may guide neocortical network activity. Neuron 67:129-143.

[60] Hutcheon, B. and Y. Yarom. 2000. Resonance, oscillation and the intrinsic frequency preferences of neurons. Trends Neurosci. 23:216-222.

[61] Richardson, M. J. E., N. Brunel and V. Hakim. 2003. From subthreshold to firing-rate resonance. J. Neurophysiol. 89:2538-2554.

[62] Dickson, C. T., J. Magistretti, M. H. Shalinsky, E. Fransen, M. E. Hasselmo and A. Alonso. 2000. Properties and role of I(h) in the pacing of subthreshold oscillations in entorhinal cortex layer II neurons. J. Neurophysiol. 83:2562-2579.

[63] Gutfreund, Y., Y. Yarom, and I. Segev. 1995. Subthreshold oscillations and resonant frequency in guinea pig cortical neurons: physiology and modeling. J. Physiol. 483:621-640.

[64] Hutcheon, B., R. M. Miura and E. Puil. Subthreshold membrane resonance in neocortical neurons. 1996b. J. Neurophysiol. 76:683-697.

[65] Llinas, R., A. A. Grace and Y. Yarom. 1991. In vitro neurons in mammalian cortical layer 4 exhibit intrinsic oscillatory activity in the 10- to 50-Hz frequency range. Proc. Natl. Acad. Sci. USA 88:897-901.

[66] Leung, L. S. and H. W. Yu. 1998. Theta-frequency resonance in hippocampal CA1 neurons in vitro demonstrated by sinusoidal current injection. J. Neurophysiol. 79:1592-1596.

[67] Pike, F. G., R. S. Goddard, J. M. Suckling, P. Ganter, N. Kasthuri and O. Paulsen. 2000. Distinct frequency preferences of different types of rat hippocampal neurons in response to oscillatory input currents. J. Physiol. 529:205-213.

[68] Hopfield, J. J. (1984). Neurons with graded response have collective computational properties like those of two-state neurons. PNAS, 81(10), 3088-92.

[69] Rall, W. (1977). Core condductor theory and cable properties of neurons. Handbook of Physiology: The Nervous System. J. M. Brookhart and V. B. Mountcastle, editors. American Physiological Society, Bethesda, Maryland. Section 1, Vol. I. 39-97.

[70] Cartee, L. A. and R. Plonsey. 1992. The transient subthreshold response of spherical and cylindrical cell models to extracellular stimulation. IEEE Trans. Biomed. Eng. 39: 1

[71] Holt, G. R. and C. Koch. 1999. Electrical interactions via the extracellular potential near cell bodies. J. Comput. Neurosci. 6:169-184.

[72] Anastassiou, C. A, Montgomery, S. M., Barahona, M., Buzsáki, G., & Koch, C. (2010). The effect of spatially inhomogeneous extracellular electric fields on neurons. The Journal of neuroscience, 30(5), 1925-36.

[73] Svirskis, G., Baginskas, A., Hounsgaard, J., & Gutman, A. (1997). Electrotonic measurements by electric field-induced polarization in

neurons: theory and experimental estimation. Biophysical Journal, 73(6), 3004-15.

[74] Griffiths, D.V., Smith, I. M. (2006). Numerical methods for engineers. Chapman & Hall, Boca Raton.

[75] Zimmerman. W. B. J. (2006). Multiphysics modeling with Finite Element Methods. Series on stability vibration and control of systems. Series A. World Scientific.

[76] McIntyre, C. C., Mori, S., Sherman, D. L., Thakor, N. V., & Vitek, J. L. (2004). Electric field and stimulating influence generated by deep brain stimulation of the subthalamic nucleus. Clinical Neurophysiology, 115(3), 589-95.

[77] Logothetis, N. K., Kayser, C., & Oeltermann, A. (2007). In vivo measurement of cortical impedance spectrum in monkeys: implications for signal propagation. Neuron, 55(5), 809-23.

[78] Lee, D. C., & Grill, W. M. (2005). Polarization of a Spherical Cell in a Nonuniform Extracellular Electric Field. Annals of Biomedical Engineering, 33(5), 603-615.

[79] Hentall, I. D. (1985). The membrane potential along an ideal axon in a radial electric field. Brain research, 336(2), 387-9.

[80] Hentall, I. D. (1987). Practical modeling of monopolar axonal stimulation. Journal of neuroscience methods, 22(1), 65-72.

[81] McIntyre, C. C., & Grill, W. M. (2001). Finite Element Analysis of the Current-Density and Electric Field Generated by Metal Microelectrodes. Annals of Biomedical Engineering, 29(3), 227-235.

[82] Monai, H., Omori, T., Okada, M., Inoue, M., Miyakawa, H., & Aonishi, T. (2010). An analytic solution of the cable equation predicts frequency preference of a passive shunt-end cylindrical cable in response to extracellular oscillating electric fields. Biophysical journal, 98(4), 524-533.

[83] Koch, C. 1999. Biophysics of computation: Information processing in single neurons. Oxford, UK: Oxford Univ. Press.

[84] Dayan, P., & Abbott, L. F. (2001). Theoretical Neuroscience: Computational and Mathematical modeling of Neural Systems. The MIT Press. Cambridge, Massachusetts.

[85] Elia, S., Lamberti, P., & Tucci, V. (2009). A Finite Element Model for The Axon of Nervous Cells. Excerpt from the Proceedings of the COMSOL Conference 2009 Milan.

[86] Destexhe, A., Contreras, D., & Steriade, M. (1999). Spatiotemporal analysis of local field potentials and unit discharges in cat cerebral cortex during natural wake and sleep states. The Journal of Neuroscience, 19(11), 4595-608.

[87] Bédard, C., Kröger, H., & Destexhe, A. (2004). modeling extracellular field potentials and the frequency-filtering properties of extracellular space. Biophysical Journal, 86(3), 1829-42.

[88] Bédard, C., Kröger, H., & Destexhe, A. (2006). Model of low-pass filtering of local field potentials in brain tissue. Physical Review E, 73(5), 1-15.

[89] Gleeson, P., Steuber, V., & Silver, R. A. (2007). NeuroConstruct: a tool for modeling networks of neurons in 3D space. Neuron, 54(2), 219-35.

[90] Gerstner, W., & Kistler, W. M. (2002). Spiking Neuron Models. Cambridge University Press.

[91] Davie, J. T., Kole, Maarten H. P., Letzkus, Johannes J., Rancz, Ede A., Spruston, Nelson, Stuart, Greg J., & Häusser, Michael. (2006). Dendritic patch-clamp recording. Nature Protocols 1, 1235-1247.